SAPIENZA
UNIVERSITÀ DI ROMA

Sapienza Università di Roma
Facoltà di Ingegneria
Dipartimento di Scienza e Tecnica dell'Informazione e Comunicazione

Dottorato di Ricerca in Telerilevamento
XXII ciclo

Innovative Adaptive Techniques for Multi-channel Spaceborne SAR systems

Candidato: Diego Cristallini

Tutore: Prof. Pierfrancesco Lombardo

INDEX

I INTRODUCTION

Synthetic Aperture Radar (SAR) is a well-known technology which allows to coherently combine multiple returns from (typically) ground-based targets from a moving radar mounted either on an air-borne or on a space-borne vehicle. The relative motion between the targets on ground and the platform causes a Doppler effect, which is exploited to discriminate along-track positions of targets themselves. In addition, as most of conventional radar, a pulsed wide-band waveform is transmitted periodically, thus allowing even a radar discrimination capability in the range direction (i.e. in distance).

For side-looking acquisition geometries, the along-track and the range directions are almost orthogonal, so that the two dimensional target discrimination capabiliy results in the possibility to produce images of the illuminated area on ground. A side-looking geometry consists in the radar antenna to be, either mechanically or electronically, oriented perpendicular to the observed area.

Nowadays technology allows discrimination capability (also referred to as *resolution*) in both along-track and range directions in the order of few tenths of centimeters.

Since the SAR is a microwave active sensor, this technology assure the possibility to produce images of the terrain independently of the sunlight illumination and/or weather conditions. This makes the SAR a very useful instrument for monitoring and mapping both the natural and the artificial activities over the Earth's surface.

Among all the limitations of a single-channel SAR system, this work focuses over some of them which are briefly listed below:

a) the performance achievable in terms of resolution are usually paid in terms of system complexity, dimension, mass and cost;

b) since the SAR is a coherent active sensor, it is vulnerable to both intentionally and un-intentionally radio-frequency interferences which might limit normal system operability;

c) since the Doppler effect it is used to discriminate targets (assumed to be stationary) on the ground, this causes an intrinsic ambiguity in the interpretation of backscattered returns from moving targets.

These drawbacks can be easily overcame by resorting to a Multi-cannel SAR (M-SAR) system.

I.1 *Chapter Summaries*

I.1.1 Chapter II: Multi-Channel SAR for Improved Resolution

The exploitation of multi-channel SAR data for improving resolution is addressed in this Chapter.

In particular, in the first part of Chapter II a coherent combination of multi-channel returns from different parallel receiving channels is considered. It is shown that, if each receiving channel is connected to a different sub-aperture of the receiving antenna, being these sub-apertures aligned in the along-track direction, an improvement of the sampling rate (i.e. the Pulse Repetition Frequency, PRF) in the azimuth domain can be achieved. This directly increases the maximum upper bound for unambiguous Doppler frequency bandwidth, hence the maximum achievable azimuth resolution. To assure that, a severe relationship between nominal PRF, sub-aperture distances and SAR platform velocity has to be verified. If this relationship it is not verified, the multi-channel data sampling in the along-track domain would result in a non-uniform sampling of the signal in the slow-time domain. This effect causes ambiguities in the azimuth domain that deteriorate the system Point Spread Function, PSF. An unambiguous signal reconstruction can be applied to keep those ambiguities below a threshold level, but a complete rejection cannot be guaranteed. An extensive performance analysis has been conducted in the framework of the ASI (Agenzia Spaziale Italiana) funded project SABRINA (System for Advanced Bistatic and Radar INterferometry Applications) aimed at developing a bistatic exploitation of the SAR of COSMO-SkyMed. In addition, an adaptive technique is proposed to overcome the main problem related to the non-perfect cancellation of azimuth ambiguities.

The second part of Chapter II deals with an innovative technique for SAR ground range resolution improvement using multiple transmit and receive platforms with adequate cross-track displacements. Using orthogonal waveforms, that occupy the same bandwidth, for different platforms of the constellation, a Multiple Input Multiple Output (MIMO) SAR system is configured. The proposed technique allows to achieve a maximum theoretical range resolution improvement factor significantly greater than the number of operating SAR sensors, by jointly exploiting both the monostatic and the bistatic acquisitions. This can be exploited to obtain a ground range resolution much higher than the resolution corresponding to the frequency bandwidth transmitted by the single platform. Afer illustrating the proposed technique and its system requirements, a simulated dataset is used to show the effectiveness of the proposed approach.

I.1.2 Chapter III: Multi-Channel SAR for Jammer Rejection

Chapter III deals with the exploitation of multi-channel SAR signals to protect the system from barrage jamming interferences, either intentional or not. This is a crucial point, since normal SAR operability can be limited or denied by electro-magnetic interferences occupying the same bandwidth of the SAR sensor. Antenna-based approaches are considered to overcome this problem, which aim at synthesizing a null, or at least a strong depression, in the Direction Of Arrival (DOA) of the interfering signal. For the special case of a M-SAR system, due to the platform motion, such a jammer DOA is changing during the synthetic aperture, thus requiring a periodic update of the adapted antenna pattern. In particular, the work focuses on the effects related to the update of nulling weights and with the synthesis of larger depressions of the antenna pattern to take into account of possible uncertainties in the knowlegde of the jammer's DOA.

I.1.3 Chapter IV: Multi-Channel for Clutter Cancellation

Chapter IV deals with the exploitation of multi-channel SAR data to suppress clutter background, thus making possible moving target detection inside SAR images. As it is well known, moving targets within SAR images appear shifted and smeared due to their relative motion with respect to the ground. This affects the possibility to detect them against the strong clutter background represented by the echoes coming from stationary distributed targets on the Earth's surface. The availability of parallel multiple receiving channels allows to subtract echo samples acquired at different receiving antennas in different times, thus cancelling stationary echoes while keeping uncancelled returns from moving objects. This is the basic principle of Space Time Adaptive Techniques (STAP). Optimum STAP filtering assures high moving target detection performance at enormous high computational costs, this is especially true for the SAR case, which it is characterized by very long integration times. Therefore, sub-optimal STAP schemes have been proposed to limit the overall computational burden at reduced detection performance losses. However, the only detection of moving targets might not be enough for existing M-SAR systems, which have sub-meter resolution capabilities. Therefore, an integration of the STAP with proper focusing techniques has to be developed in order to assure not only the detection of the movers, but also their high-resolution imaging[1]. While STAP has been deeply analyzed in past literature, limited interest has been addressed to an *efficient* integration of STAP techniques together with focusing algorithms.

The work presented in Chapter IV refers to an efficient integration of a particular quasi-optimal post-Doppler STAP technique with a bank of focusing filters based on the Chirp Scaling algorithm. Specifically, the first analysis is devoted to the performance evaluation of the bank of focusing filters to

[1] Due to the relative motion of ground moving targets with respect to stationary scene, the focusing filter matched to the stationary background is not matched to moving targets, thus causing imaging performance degradations.

show the increase in terms of imaging capabilities and also in terms of detection capability. Subsequently, an efficient integration of post-Doppler STAP and bank of focusing filters is presented. The analysis shows that both techniques are needed for detection and high-resolution imaging of movers. The last part of Chapter IV is devoted to a computational cost evaluation of the integrated technique. For comparison, an Along-Track Interferometry (ATI) based approach is considered.

II MULTI-CHANNEL SAR FOR IMPROVED RESOLUTION

II.1 *Introduction*

Increasing interest in recent years has concerned the development of new SAR imaging modes being able to ensure the so called High Resolution Wide Swath (HRWS) SAR. As it is well known, intrinsic limitations pose in direct relation these two desirable characteristics, namely imaged swath and obtainable resolution, for a single-channel SAR system. Basically, a requirement in the minimum physical antenna area has to be verified in order to avoid ambiguities both in azimuth and in range dimensions. As it is clear, this minimum antenna area constraint is even more severe for spaceborne SAR systems, since directly affects size, mass, and costs of the platform to be launched.

A viable solution to overcome this minimum area constraint is to resort to Multi-channel SAR (M-SAR) systems. Various solutions can be considered, related to monostatic and bi-/multi-static geometries. Obviously, a multi-channel SAR system, even if theoretically able to achieve HRWS modes, has to deal with other technological issues, such as synchronization, paraller receiving channel matching, etc… In this chapter, these aspects will not be considered, while focusing on some innovative techniques for multi-channel data processing for HRWS SAR. In particular, in Section II.2 it will be addressed the possibility to use multiple parallel receiving channel for increasing the data sampling in the along-track dimension (namely to increase the PRF). As it is well known, the PRF value selection has to guarantee both an adequate sampling of the instantaneous Doppler bandwidth as well as an adequate interval time for receptions of all the echoes from the swath to be imaged. Therefore, if the

receiving antenna is splitted in two (or more) sub-apertures aligned in the along-track direction, and if a simultaneous reception of data samples is conducted in for each sub-aperture, an equivalent increase in the theoretical improvement of the azimuth resolution at constant swath size, or, equivalently, to increase the swath size at constant azimuth resolution can be obtained.

Section II.3 is addressed to the analysis of possible exploitation of constellation of SAR platforms for range resolution improvement. In particular, a Multiple Input Multiple Output (MIMO) SAR system is considered with different platforms observing the same area on the ground with different incident angles. In past literature ([5][6][7]) it has been proved that such a geometrical configuration of multiple platforms can lead to an increase of the resolution in the range direction, by exploiting the wavenumber shift, [5]. Specifically, a maximum theoretical improvement in range resolution equal to the number of platforms can be achieved (i.e. coherent integration of all the monostatic acquisitions). The idea here presented resort to the exploitation not only of the monostatic acquisitions, but also of the bistatic ones. As a consequence, the maximum theoretical improvement of the range resolution becomes equal to the overall number of monostatic plus bistatic acquisitions, hence an improvement factor greater than the number of SAR platforms. To make this possible, a MIMO SAR system has to be considered being the single SAR systems able to transmit almost orthogonal waveforms and able to discriminate echoes corresponding to monostatic and bistatic acquisitions by means of multiple parallel receiving channels.

II.2 *Enhanced Imaging*

Exploiting the multi-channel antenna versatility, Extended Imaging (EI) permits an improvement of the image geometric characteristics. Many applications require a very high spatial resolution either to detect, recognize and identify small man-made targets or to have a high accuracy in the estimation of borders between regions in natural vegetated areas. In particular, using EI it is possible to increase the azimuth spatial resolution, or to improve the radiometric resolution without decreasing the spatial resolution, without the need to operate in Spotlight mode and thus without largely reducing the azimuth size of the imaged area.

Another limitation of the imaging capability of spaceborne SAR is related to the range swath size and therefore to the revisit time. Although conventional Stripmap revisit time may be adequate for the surveillance of certain features, especially for the COSMO-SkyMed constellation, such as geologic formations and crops, for other more dynamic features, such as oceans, ice and man-made targets, there could be a requirement for shorter revisit times. This can be obtained through Extended Imaging Optional Techniques which, improving the range swath extension, enable an increase of the monitored area and thus a reduction of the revisit time, [1].

EI are utilized only in Stripmap acquisition mode, but they allow to exploit at the same time the advantages of both Stripmap and Spotlight acquisition modes. In fact using EI it is possible to have a large swath and, at the same time, to obtain an azimuth resolution comparable to the Spotlight one.

As well known, in a single channel SAR, high azimuth resolution and wide swath extension set contrasting requirements on the PRF selection. In fact, in the conventional Stripmap acquisition mode, the highest achievable azimuth resolution is fixed at L/2 (where L represents the along track antenna

dimension). This value of resolution sets a lower bound on the PRF value to avoid azimuth ambiguities; any improvement of the azimuth resolution requires an increase on this lower bound. Besides, the range swath extension is limited by the elevation antenna pattern and by the chosen value of PRF (resulting in a maximum unambiguous zone equal to $c/(2\times PRF)$), and therefore an improvement of the swath extension requires a decrease of the PRF value.

In the EI the signal emitted by the transmitter is acquired simultaneously by two parallel receiving channels one of each associated to a different RX-antenna sub-aperture obtained splitting the whole antenna in the along-track direction. This implies two phase centers displaced in the along-track direction. The motivation for this approach is that two independent sets of target returns are obtained for each transmitted pulse. If the sensor platform velocity v, the PRF value and the along-track displacement of the two phase centers (dx) are such that

$$PRF = \frac{v}{dx}, \qquad \text{Eq. II-1}$$

then the samples received on the two RX-channels are identical to the samples received by a conventional SAR operating with a double PRF. The PRF value of Eq. II-1 is such that the SAR platform moves just one half of the total antenna length between subsequent radar pulses, as depicted in

Figure **II-1**.

This situation corresponds to a uniform sampling of the SAR signal after data stream recombination, [2]. Therefore the value of PRF that satisfies the Eq. II-1 will be indicated as “uniform PRF” in the following. Through a coherent processing, it is possible to combine the data sets thus obtaining an improvement on the signal sampling frequency (i.e. the PRF).

However such a rigid selection of the PRF (cfr. Eq. II-1) may be in conflict with the timing diagram for some incident angles and exclude the possibility to use an increased PRF for improved azimuth ambiguity suppression. Therefore in our preliminary analysis of EI, a reconstruction algorithm for unambiguous recovery of SAR signal from non uniform sampling, as presented in [3] has been exploited.

Depending on the user requirement to increase the imaging capability in term of azimuth resolution or range swath extension, two different EI can be exploited:

- EI-R (Resolution improvement): the transmitting antenna has an azimuth aperture augmented[2] with respect of the usual single-channel case in order to extend the azimuth footprint. The received signal is acquired by the two parallel RX-channels each one relative to a half side of the receiving antenna (**Figure II-2**). Performing a coherent processing on the two received signals and using the same PRF of the single-channel case, it is possible to improve the azimuth resolution without reducing the range swath extension.
- EI-S (Swath extension improvement): the transmitting antenna has the same pattern aperture of a usual single-channel system in azimuth direction, whereas the pattern aperture is augmented in elevation direction in order to increase the illuminated zone in range direction. The received signal is acquired by the two parallel RX-channels each one relative to a half side of the receiving antenna (**Figure II-3**). Performing a coherent processing on the two received signals,

[2] Note: the increasing of the pattern aperture in one of the two direction of azimuth or elevation can be obtained through a proper phase tapering on the radiating elements in the transmitting antenna. Such a technique allows an augmentation of the antenna aperture not reducing the transmitted power level.

it is possible to reduce the value of PRF (regarding the single-channel case), thus allowing an improvement of the unambiguous zone, without reducing the azimuth resolution.

- EI-T (optimal Trade-off): instead of exploit the EI performances alternatively in terms of azimuth resolution improvement (EI-R) or in terms of range swath widening (EI-S), it is interesting to jointly exploit a partial improvement in each of the two EI techniques. Specifically, an EI optimal trade-off can be obtained by varying both the acquisition time, T_A, (and thus varying the azimuth resolution) and the value of PRF (thus varying the range swath extension). The variation intervals of these parameters are chosen such as: (*i*) T_A varies so that the achieved azimuth resolution varies from the nominal Stripmap value L/2 toward the halved valued L/4[3]; (*ii*) the PRF varies so that the range swath extension varies from the nominal Stripmap value to a doubled value.

II.2.1 Definition of the performance parameters for EI

The implementation of the EI influences the following aspects:

- Azimuth Resolution;
- Range Swath Extension;
- Signal to Noise Ratio (SNR);
- Azimuth Ambiguities Level;
- Volume of Collected Data.

[3] In order to guarantee the desired azimuth spatial resolution improvement, other than the acquisition time, the transmitted azimuth pattern beamwidth is properly chosen too. In particular, the transmitted beamwidth is enlarged of a factor equal to the acquisition time improvement.

In particular the two following parameters are considered in order to evaluate the impact of the implementation of EI on the SAR image quality:

- Noise Equivalent Sigma Zero (NESZ): defined as the level of RCS (Radar Cross Section) that an hypothetical target should have so that the peak value of the corresponding focused signal is equal to the thermal noise level. In the performance analysis, the NESZ will be evaluated with respect to the NESZ of the nominal Stripmap acquisition mode (indicated as $NESZ_{nominal}$ in the following).
- Azimuth Ambiguity Ratio (AAR): measured as the ratio of the focused signal peak powers from the mainlobe to the first order ambiguity at Doppler frequency ±PRF, as presented in [3].

The improvement of geometric characteristics achievable by applying the EI techniques, will be evaluated on the basis of the three following parameters.

In particular, the performance of EI-S are evaluated through the **Swath Improvement (SI)** parameter defined as the ratio between the $PRF_{nominal}$ and the PRF_{actual}:

$$SI = \frac{PRF_{nominal}}{PRF_{actual}} \qquad \text{Eq. II-2}$$

where $PRF_{nominal}$ = 3632.4 Hz is the nominal PRF of COSMO-SkyMed in Stripmap acquisition mode for the considered incidence angle (37.78°).

Moreover the performance of EI-R are evaluated through the **Resolution Improvement (RI)** parameter defined as the ratio between the nominal Stripmap azimuth resolution of COSMO-SkyMed ($r_{nominal}^{AZ} = 2.8\,m$) and the actual azimuth resolution:

$$RI = \frac{r_{no\,min\,al}^{AZ}}{r_{actual}^{AZ}} \qquad \text{Eq. II-3}$$

For the EI-T, the further following performance parameter has been considered.

Information Gain (IG): defined as the product of the inter-pulse period (PRF^{-1}), determining directly the unambiguous swath width, and the inverse azimuth resolution normalized by the sensor velocity:

$$IG = \frac{v}{r_{actual}^{AZ} \cdot PRF_{actual}} \qquad \text{Eq. II-4}$$

In a conventional SAR operating in Stripmap mode the PRF is chosen greater than the Doppler bandwidth (equal to $B_{Dop}=v/r_{AZ}$) in order to avoid azimuth spectral folding. Therefore, the maximum theoretical value of IG for a conventional Stripmap SAR, is equal to 1. Moreover, using EI, the value of B_{Dop} can be up to 2PRF, thus resulting in a maximum theoretical value of IG equal to 2.

II.2.2 Preliminary analysis of EI performance

Analyzed scenario for both EI-S and EI-R:

- Stripmap acquisition mode
- Interferometric configuration

For each one of the proposed techniques, several simulations have been performed in order to demonstrate the validity of the EI.

The simulations have been performed placing a point target with unitary RCS in a broadside position. For the EI-S, we have simulated the operation of a dual receive antenna SAR system with fixed distance between the two phase centers, but varying the value of PRF. Focusing is done by a matched filter with a constant Doppler bandwidth in a processing that considers only the azimuth dimension. The Doppler bandwidth is chosen so that an azimuth resolution of L/2 is achievable. For the EI-R, the chosen approach was to simulate the operation of a dual receive antenna SAR system with fixed distance between the two phase centers, but varying the acquisition time in order to vary the achievable azimuth resolution. Evaluating the performances achievable using EI, the two parameters of NESZ and AAR have been considered. The following table reports the main system/sensor used parameters.

In order to guarantee a symmetrical split of the antenna into two sub-apertures, without sharing any tile between the two receiving channels, for some antenna configurations, the one or more central panels are not used and so they are depicted in grey in the following figures. This represents a loss in the RX-antenna gain, or which is equivalent an increase of the NESZ, proportional to the number of unused panels. In particular the configuration SPAN2a (both for COSMO5x8 and COSMO6xY) and the antenna COSMO6xY (with Y<8) are not considered because the number of used tiles in each sub-antenna is not sufficient to guarantee a proper value of NESZ, whereas the configurations COSMO5x8 STRX and COSMO6x8 STRX are not considered because they are only single-channel.

COSMO5x8 SPAN2b

In **Figure II-4** and Tab. II-2 is described the COSMO5x8 SPAN2b configuration. The panels relative to the two receiving channels are colored in green and light blue. The phase centers of the two receiving sub-antennas are depicted as red dots.

COSMO6x8 SPAN2c

In **Figure II-5** and Tab. II-3 is described the COSMO6x8 SPAN2c configuration. The panels relative to the two receiving channels are colored in green and light blue. Using the COSMO6x8 antenna, having an even number of panels, it is possible, differently from COSMO5x8 case, to divide the whole antenna into two sub-apertures, thus using all the available panels. The phase centers of the two receiving sub-antennas are depicted as red dots.

COSMO6x8 SPAN2b

In **Figure II-6** and Tab. II-4 is described the COSMO6x8 SPAN2b configuration. The panels relative to the two receiving channels are colored in green and light blue. This configuration has the same number of panels of COSMO5x8 SPAN2b case, but has a greater phase centers displacement. The phase centers of the two receiving sub-antennas are depicted as red dots.

II.2.3 EI-R case study

In EI-R we aim to achieve an improvement in the azimuth resolution not diminishing the range swath extension. Using the system parameters reported in Tab. II-1 and the antenna configurations described above, we have evaluated the system performances in terms of AAR versus T_A calculated for each antenna configuration, for its uniform PRF. The variation of the acquisition time determines a variation of the achievable azimuth resolution.

In **Figure II-7** a comparison between the three configurations is reported. As shown in the figure, COSMO6X8 SPAN2b is able to achieve good azimuth ambiguity suppression only for low values of acquisition time, thus determining a smaller azimuth resolution improvement than the other antenna configurations. Moreover the analogous value of phase center displacement of COSMO5x8 SPAN2b and COSMO6x8 SPAN2c, determines the similar behavior of the AAR in these two configurations. The

slight difference between them is due to the different receiving azimuth pattern. In fact COSMO6x8 SPAN2c has a single-channel receiving antenna made by 3 panels, whereas in COSMO5x8 SPAN2b the RX-antenna has only 2 panels. Therefore the narrower azimuth pattern of COSMO6x8 SPAN2c guarantees a better azimuth ambiguity suppression. Posing a threshold on the AAR at -25 dB, for each antenna configuration, the best azimuth resolutions achievable are reported in Tab. II-5.

EVALUATION OF NESZ FOR EI-R

The EI-R operation mode needs a broadened azimuth transmitting pattern in order to improve the azimuth resolution. A phase tapering on the TX-antenna guarantees the desired azimuth pattern widening without reducing the transmitted power level. Anyway this power level is now irradiated on a greater angle, thus resulting in a reduction of the SNR or (which is equivalent) in an increase of the NESZ of a factor equal to the azimuth beam increase. Through a proper selection of the acquisition time (corresponding to the widened synthetic aperture) it is possible to obtain an azimuth integration gain equal to the above mentioned reduction. Therefore in EI-R it is possible to maintain the NESZ equal to the conventional Stripmap case.

II.2.4 EI-S case study

In **Figure II-8** a comparison of AAR for the three considered antenna configurations in EI-S is reported. As previously shown analyzing EI-R, COSMO6x8 SPAN2c and COSMO5x8 SPAN2b present a similar behavior due to the equal phase centers displacement. For the same reason, COSMO6x8 SPAN2b is able to obtain good azimuth ambiguity suppression for lower values of PRF in respect to the other configurations. Defining an AAR threshold at -25 dB, we might say that even if the interval of PRF values under the threshold is narrower in COSMO6x8 SPAN2b case, this interval is shifted toward lower values of PRF, thus permitting, among the considered configurations, a greater

range swath extension enlargement, if the mentioned range of PRF is range ambiguity free for the desired imaging incidence angle. Hence COSMO6x8 SPAN2b might allow the best geometric characteristics improvement in EI-S mode. COSMO6x8 SPAN2c allows a slightly lower improvement of the geometric characteristics but using a different range of PRF values. In **Figure II-8**, on the x-axis, the labelled values of PRF are those that allow to avoid nadir returns.

EVALUATION OF NESZ FOR EI-S

The EI-S needs a broadened transmitting elevation pattern in order to illuminate the widened range swath. A phase tapering on the TX-antenna guarantees this elevation beam widening not reducing the transmitted power level. Anyway this power level is now irradiated on a greater angle, thus resulting in a reduction of the SNR or, equivalently, in an increase of the NESZ of a value equal to the elevation beam widening factor. If the number of tiles in elevation of the chosen RX-antenna coincides with the number of tiles in elevation of the TX-antenna (using, for example, COSMO5x8 or COSMO 6x8 antenna), then an identical phase tapering is required for the RX-antenna. Differently from the EI-R case, where the increase of NESZ is counterbalanced by the improved azimuth integration gain, in EI-S there is a loss on the NESZ proportional to the elevation beam widening factor.

Referring to the antenna configurations presented above, and comparing the different COSMO6xY antennas with the COSMO6x8 one, at least two different NESZ loss factors arise: the first one is the loss due to the elevation beam widening through phase tapering, the second is the loss due to the reduced number of elevation tiles (i.e. of total transmitted power). With reference to the first factor loss, we might say that as the number of elevation tiles decreases, the elevation beam gets larger and so the widening beam factor relative to the phase tapering decreases too. This results in a diminished NESZ loss due to the phase tapering.

Moreover, considering the second factor loss, as the number of elevation tiles decreases, the NESZ loss due to the reduced number of antenna radiating elements increases. Therefore the overall NESZ loss due both to phase tapering and to the number of elevation tiles is about constant among the different COSMO6xY antenna configurations.

II.2.5 EI-T case study

For these simulations the same configuration parameters reported in Tab. II-1 have been used. A grid of values of T_A and PRF has been created and, for each pair of (T_A, PRF), the AAR parameter has been evaluated.

Among the grid of values of (T_A, PRF), we have considered only the pairs that guarantee an AAR better than -25 dB, and for these pairs we have evaluated the IG. The following sections report the simulated results of EI-T for the three considered configurations.

COSMO5x8 SPAN2b EI-T

Figure II-8 and **Figure II-9** report the performances of this antenna configuration in terms of AAR and IG. It is simple to notice that the azimuth ambiguity suppression decreases as the acquisition time increases, this is due to the increase of the Doppler bandwidth. As illustrated in **Figure II-8**, the best suppression is achieved around the uniform PRF value.

Within the considered interval of PRF, we have selected three different values of PRF. The first two values of PRF correspond to the minimum and maximum values that guarantees an AAR<-25 dB, whereas the third value corresponds to a uniform PRF. For these three values of PRF we have evaluated the IG versus T_A, as reported in the following **Figure II-11**. As it is apparent, at the same acquisition time (hence at constant azimuth resolution), the Information Gain is greater for lower values of PRF, which allows enlarged range swath extension. Moreover, this figure shows that, applying the EI, it is

possible to improve the information gain up to about 1.9. Values of IG greater than 1.9 closer to the theoretical upper bound of 2, can be obtained relaxing the constraint on AAR.

COSMO6x8 SPAN2c EI-T

Figure II-12, show the simulated results for COSMO6x8 SPAN2c. This antenna configuration presents a behavior similar to COSMO5x8 SPAN2b, therefore analogous considerations apply.

COSMO6x8 SPAN2b EI-T

The two following figures show the simulated results for COSMO6x8 SPAN2b. Comparing the AAR values obtained in **Figure II-15**, with those obtained in **Figure II-9** and in **Figure II-12**, it is possible to notice a worse azimuth ambiguity suppression. However, the values of IG obtained for this antenna configuration (**Figure II-17**) are comparable with those obtained in other cases (**Figure II-11** and **Figure II-14**) due to the lower values of uniform PRF.

II.2.6 Conclusions for the EI performance

From the analysis performed above, it is reasonable consider, for the three EI, the constraints reported in **Tab. II-6** on the AAR and on the NESZ.

The following losses of NESZ could be experienced with respect to the $NESZ_{nominal}$ (cfr. Section II.2.1), for the considered antenna configurations and for a swath increase up to 2 and resolution increase up to 2, in EI-S and EI-R respectively. The NESZ loss for the EI-T varies in dependence to the chosen combination of (r^{AZ}_{actual}, PRF_{actual}).

Considering this constraint for AAR, the following values of Swath Improvement, Resolution Improvement and Information Gain for the considered antenna configurations can be achieved (see Tab.

II-8, Tab. II-9 and Tab. II-10). These values represent the upper bounds that can be obtained using EI choosing conveniently the acquisition time and the PRF.

While an improvement of the geometric characteristics of the SAR image of a factor of two would be ideally desirable for the user, from the analysis above it is clear that this could obtained only with a significant reduction of the image quality, represented in terms of AAR and NESZ. Therefore, it is reasonable to set as user requirements slightly lower values for the geometric characteristic improvement, which still allow to guarantee an adequate quality of the resulting SAR image.

In particular, for achieving acceptable SAR image quality, the Azimuth Ambiguity Ratio is required to be not higher than -25 dB for EI-S, and EI-T and -20 dB for EI-R.

The specific user need for the three EI versions can be set as follows:

- EI-R: it is required to provide an increase of the azimuth resolution of a factor at least 1.5, without introducing any degradation in swath size, range resolution, and NESZ, with respect to the SAR image obtained using the full antenna aperture for the echo reception.

- EI-S: it is required to provide an increase of the range swath of a factor at least 1.5, without introducing any degradation in spatial resolution, and with a loss in NESZ not larger than 6 dB, with respect to the SAR image obtained using the full antenna aperture for the echo reception.

- EI-T: it is required to provide a joint increase of the range swath and azimuth spatial resolution, resulting in an Information Gain of a factor at least 1.75, with a loss in NESZ not larger than 6 dB, with respect to the SAR image obtained using the full antenna aperture for the echo reception.

Preliminary system requirements

In order to guarantee a proper operability of EI, the following preliminary system requirements must be met.

- Receiver channels

The system must support the simultaneous, fully coherent, operation of the two RX-channels.

Using two RX-channels the preferred channel configuration to be considered for the EI processing techniques are the following:

- EI-S: the configuration COSMO6x8 SPAN2b allows to achieve the best SAR image geometric characteristics among the considered antenna configurations, anyway all the three configurations allow to achieve the Swath Improvement reported as user requirement in the previous section.
- EI-R: the configuration COSMO5x8 SPAN2b allows to achieve the best SAR image geometric characteristics among the considered antenna configurations, anyway also the COSMO6x8 SPAN2c configuration allow to reach the Resolution Improvement reported as user requirement in the previous section.
- EI-T: the configuration COSMO6x8 SPAN2b allows to achieve the best SAR image geometric characteristics among the considered antenna configurations, anyway all the three configurations allow to achieve the Information Gain reported as user requirement in the previous section.

- Data-link channel, storage system, Central Processing Unit

In order to guarantee the applicability of the EI, due to the augmented range swath extension and/or augmented acquisition time, the satellite system has to be able to storage and down-link a volume of data greater than the nominal COSMO-SkyMed Stripmap case.

II.2.7 Adaptive antenna configurations

The analysis conducted above showed that a minimum AAR value can be obtained for PRF values in the proximity of the corresponding "uniform value" and that this value is set by the phase centers distance and by the platform velocity. Since the platform velocity cannot be change in general, especially when dealing with a space-borne platform, the only available degree of freedom for changing the "uniform value" of the PRF is represented by the phase center distance *dx*. A simple, but effective, way of changing the phase center distance can be to switch-off several columns of TR modules, for example by means of amplitude weights tapering. This makes the implementation of the EI techniques adaptive. In the following this simple idea has been investigated more in detail with reference to a sample phased-array antenna configuration, and imaging performance are evaluated.

The basic idea of this technique is, exploiting the potentials of a phased array antenna, to achieve different values of uniform PRF. This is obtainable varying the phase centers displacement of the two receiving sub-apertures through a proper amplitude tapering. In particular, for every amplitude tapering configuration, the elaboration consists in the application of the reconstruction algorithm presented in [3] to the data streams acquired on the two receiving channels. Due to the different phase centers displacements, different values of uniform PRF characterized by low levels of azimuth ambiguity are available. This may offer the possibility to select the PRF value in agreement with the restrictions due to nadir returns and transmission/reception overlap topics. Moreover it is interesting to notice that the proposed approach can be easily adapted to a bistatic passive SAR system. In such a configuration, the value of PRF is set by the transmitter and may not be modified to reduce the AAR, and therefore the above mentioned further degree of freedom in the PRF selection may become particularly suitable to limit azimuth ambiguities.

Reference Antenna Structure

The reference antenna structure is a modular phased array made by 6 x 8 tile (azimuth x elevation). Each tile is constituted by 5 x 8 T/R modules (azimuth x elevation) and each T/R module is formed by 10 radiating elements aligned in the along track direction. The resulting structure is depicted in **Figure II-18** (each rectangle representing a tile) with the two sub-apertures represented in orange and blue, whereas in **Tab. II-11** the main antenna parameters are reported.

Adaptive Antenna Configurations

In this section we define several antenna configurations which present different phase centers displacements. The different antenna configurations are obtained through specific amplitude tapering applied at T/R module level using attenuators. In fact in a phased array is not always possible to control every single radiating element, but typically several radiating elements are controlled by a single attenuator. Therefore we consider that all the elements in a T/R module are controlled by the same attenuator.

Each adaptive antenna configuration is obtained through an amplitude tapering that, switching off several T/R modules aligned along the elevation direction, permits to vary the azimuth length of both sub-aperture. Referring to **Figure II-19**, we can introduce five considered configurations:

- **CONF-A**: this configuration is obtained from the whole antenna switching off only the columns of T/R modules labeled with A;
- **CONF-AB**: this configuration is obtained from the whole antenna switching off only the columns of T/R modules labeled with A and B;
- **CONF-ABC**: this configuration is obtained from the whole antenna switching off only the columns of T/R modules labeled with A, B, and C;

- **CONF-ABCD**: this configuration is obtained from the whole antenna switching off only the columns of T/R modules labeled with A, B, C, and D;
- **CONF-ABCDE**: this configuration is obtained from the whole antenna switching off only the columns of T/R modules labeled with A, B, C, D, and E.

Varying the arrangement of the switched off T/R modules, other configurations could be obtained, but not everyone presents adequate sub-aperture pattern characteristics. For example, a large number of switched off T/R modules may not be able to guarantee a sufficient gain, whereas a non-uniform arrangement of the switched off T/R modules within the sub-aperture, could generate some irregularities in the sub-aperture pattern shape both in elevation and in azimuth direction.

The five considered configurations present different phase centers displacements, as reported in **Tab. II-12**. Obviously, the specific physical antenna structure, in particular the number of radiating elements controlled by the same attenuator, determines the beam forming capability and the level of accuracy achievable in the selection of the phase centers displacement.

The phase centers displacement variation is alternatively achievable with a phased array antenna if a staggered configuration is available. Such a configuration is characterized by a relative azimuth shift among tiles located at different positions in the elevation direction. The joint use of staggered antenna structure and switch off technique, as described in the previous sections, allows a finer phase centers displacement selection. The level of accuracy obtainable following this approach obviously depends on the specific staggered configuration.

Description of the Simulation Scenario

In order to prove the applicability of the proposed approach and to evaluate the achievable performances, several simulations have been performed. A signal simulator has been developed with the purpose to generate signal acquired by a monostatic dual-channel SAR sensor working in Stripmap

acquisition mode. A point target with unitary RCS placed in a broadside position has been injected. With the aim to simulate the presence of an ambiguous signal, a second target, with a Doppler centroid equal to PRF, is placed in the observed scene. The SAR signal reconstruction from the samples acquired on both receiving channels is realized applying the reconstruction filtering presented in [3]. The simulations have been performed for the five antenna configurations each one varying the PRF value. Focusing is done by a matched filter with a Doppler bandwidth chosen in agreement with the azimuth sub-aperture beamwidth of the considered antenna configuration. **Tab. II-13** reports the main system parameters used for the simulations.

In the following, the performance of the considered amplitude tapering configurations are reported in terms of azimuth resolution and range swath dimension improvements. Moreover, for each considered configuration, the available PRF values are determined and the azimuth ambiguity level is evaluated.

The following **Figure II-20** shows the behavior of AAR versus PRF for the considered antenna configurations. As apparent, the different antenna configurations present an AAR global minimum value in correspondence of the relative uniform PRF. **Figure II-20** also reports, along the PRF axis, the PRF values that allow to avoid interference between useful echoes reception and nadir returns for the considered acquisition geometry (PRF_{NADIR}). As it is shown in the figure, the application of the proposed technique makes available several intervals of PRF with low level of AAR, whereas using a single antenna configuration low values of AAR are obtainable only in one interval of PRF. Therefore, the adaptivity in the amplitude tapering configuration selection is demonstrated to permit the selection of a PRF value characterized by an AAR null, which is in the proximity of a “nadir return free” value.

Tab. II-14 reports the values of azimuth resolution obtained for the five considered tapering configurations with the relative uniform PRF values. Specifically the azimuth resolution improvement and the swath dimension improvement are considered, defined as the ratios between the obtained values and the nominal Stripmap single-channel counterparts.

As apparent, all the five tapering configurations permit to achieve an improvement in the image geometric characteristics. In particular it appears clear that as the sub-aperture antenna length decreases (moving from CONF-A to CONF-ABCDE), the sub-aperture azimuth beamwidth increases, thus permitting to acquire targets with a higher Doppler bandwidth and so with a higher azimuth resolution.

The range swath dimension improvement presents the same behavior, therefore the configuration CONF-ABCDE is able to achieve better geometric characteristics improvement with respect to the other considered configurations, however this configuration is influenced by a slightly higher value of AAR and by a lower sub-aperture gain (see **Tab. II-12**), which results in a received signal power loss.

In the application of the proposed technique to a dual-channel SAR system for wide swath and high azimuth resolution, the maximum allowed number of switched off T/R modules plays an important role. In fact, this limitation directly determines the number of adaptive antenna configurations which can be obtained and therefore the number of available uniform PRFs. On the other side, a high number of switched off T/R modules could penalize too much the maximum sub-aperture gain, as reported in **Tab. II-12**.

In conclusion, we have investigated the possibility to exploit the capability of a phased array to vary the phase centers displacement in a dual-channel SAR system. Adaptive antenna configuration, obtainable through amplitude tapering or staggered antenna structure, permits to improve the geometric characteristics of a SAR image without degradations due to azimuth ambiguities.

II.3 *MIMO SAR for Range Resolution Improvement*

In this section an innovative technique is presented for SAR ground range resolution improvement using multiple transmit and receive platforms with adequate cross-track displacement. Using orthogonal waveforms, that occupy the same bandwidth, for the different platforms of the constellation, a Multiple Input Multiple Output (MIMO) SAR systems is configured. The proposed technique allows to achieve a maximum theoretical range resolution improvement factor significantly greater than the number of operating SAR sensors, by jointly exploiting both the monostatic and the bistatic acquisitions. This can be exploited to obtain a ground range resolution much higher than the resolution corresponding to the frequency bandwidth transmitted by the single platform. After illustrating the proposed technique and its system requirements, a simulated dataset is used to show the effectiveness of the proposed approach.

As well known Synthetic Aperture Radar (SAR) ground range resolution depends on the transmitted signal frequency bandwidth, which is usually limited by regulation, or operating permission, as well as by technological constraints. From a regulation point of view, very often the international rules assign to radar applications only a limited fraction of bandwidth (for example, the International Telecommunication Union reserves only about 300 MHz at X-band). Moreover, from a technological point of view, a wider bandwidth imposes both stronger requirements on the hardware of the transmit and receive chain, and the requirement of a higher down-link capacity to ground (as usually done in most present spaceborne and airborne SAR systems).

It is clear that the chance to relax the hardware requirements of the SAR sensor has a major impact on the possibility to build low-mass and low-cost SAR sensors and therefore on the possibility to implement constellations of small SAR satellites, which has been widely considered in the recent years.

Among the main advantages of the constellation of SAR sensors, there are the robustness to failures as well as the system reconfiguration capability. Moreover, while the limited performance capability of the single sensor is the price to be paid for reducing mass and costs, the constellation is required to retrieve a performance level comparable, or even better, than usual SAR systems, by exploiting the joint operation of the multiple SAR sensors, once the synchronization issues have been appropriately dealt with. The same kind of considerations applies even more to airborne/Unmanned Air Vehicles (UAV) formations with each platform in the formation carrying a low-mass and low-cost radar system.

In particular, limiting the transmitted waveform frequency bandwidth contributes to make the single sensor cheaper and lighter, at the expense of a reduced range resolution. In this context, it is interesting to investigate whether it is possible to increase the overall range resolution by exploiting the signal received by multiple sensors, where the single sensor has only a limited ground resolution capability. It is especially interesting to achieve this, assuming that all the sensors use waveforms occupying the same frequency range (for example, the one permitted by the regulations).

In [5] a technique for improving range resolution by exploiting multiple surveys of the same area has been described. This technique allows a maximum theoretical improvement factor in range resolution equal to the number of surveys, if proper off-nadir angles are selected, see also [6] and [7]. As apparent, this improvement could be obtained by exploiting multiple SAR platforms that observe the same scene with appropriate off-nadir angles. However the contemporaneous presence of the multiple platforms is not required, so that a single SAR platform could be sufficient, provided that it can observe the desired scene with the required angles at different times. As an alternative, the same approach can be applied to a so-called Multistatic SAR system constellation of S_{REAL} sensors, as sketched **Figure II-21**. In this configuration, only one SAR sensor (for example *sensor 1*) is transmitting and all the S_{REAL} sensors, observing the same area on the ground with different off-nadir angles, are contemporaneously receiving. Therefore, the overall number of surveys for a Multistatic SAR system is

given by the monostatic acquisition of *sensor 1* plus all the S_{REAL}-*1* bistatic acquisitions. Hence, the resulting maximum range resolution improvement factor is equal to the number of sensors S_{REAL}.

For a MIMO (Multiple Input Multiple Output) SAR system, all the S_{REAL} sensors are simultaneously transmitting and receiving, as sketched in **Figure II-22**. By exploiting adequate orthogonal waveforms in transmission, each sensor is able to distinguish the echoes corresponding to the different transmissions. As a result, the overall number of surveys made available to the MIMO SAR system is given by all the S_{REAL} monostatic acquisitions plus all the possible combinations of bistatic acquisitions that are characterized by an equivalent off-nadir angle which lies between the transmitting and the receiving angles. Depending on the selected geometrical configuration, not all the bistatic acquisitions result in an independent survey. Anyway, by exploiting both the monostatic and the bistatic acquisitions, the geometrical configuration of the sensors can be designed such as the overall number of independent surveys (S_{TOT}) is greater than the number of SAR sensor (i.e. $S_{TOT} > S_{REAL}$). This will result in a maximum range resolution improvement factor greater than the number of sensors.

The focus of this section is on MIMO SAR systems: specifically the aim is to exploit the contemporaneous presence of the different transmit and receive platforms, together with their use of an orthogonal set of waveforms, so as to design a MIMO SAR system to achieve an improvement in the range resolution of a factor approaching the value $S_{REAL}(S_{REAL}+1)/2$ which can be sensibly larger than the number of platforms. As stated above, this possibility to obtain such an increase of range resolution via the proposed MIMO SAR concept can be of great interest in presence of strict limitations on the available frequency bandwidth allocated to radar remote sensing. Moreover the same technique could be also an add-on in a number of different situations, such as: (i) for two or more large transmit/receive satellites already available (tandem missions and constellations of satellites) which could be provided with the potentialities to increase range resolution up to a factor sensibly higher than the number of platforms when working with appropriate waveforms and orbital configurations; (ii) for constellations

of mini-satellites developed both for civil and defense applications; (iii) for formations of transmit/receive UAVs, especially for defense applications.

We notice that while the increase of ground range resolution has led to the full problem of SAR tomography, our technique to exploit MIMO approach to increase performance in a way sensibly greater than the number of platforms can also be applied to SAR Tomography, [7]-[11].

This section is organized as follows. To obtain the optimal geometrical configuration of a MIMO SAR system for each value of S_{REAL}, in Section II.3.1 we introduce the equivalence between chirp frequency bandwidth and equivalent cross-track aperture. In Section II.3.2 , we present the MIMO SAR concept for $S_{REAL} = 2$ SAR platforms that exploit both monostatic and bistatic sub-apertures, and show a demonstration of principle. In Section II.3.3 , we present the optimal configuration of S_{REAL} SAR platforms to achieve the large continuous aperture by means of monostatic and bistatic sub-apertures and convert it back to off-nadir angle for the SAR sensors. In Section II.3.4 the issue of waveform orthogonality is addressed. Section II.3.5 is devoted to the processing techniques to combine the signals collected by the different sensors to achieve the best possible ground resolution, while in Section II.3.6 the effectiveness of the proposed approach is tested over a simulated dataset. Finally, in Section II.3.7 we draw our conclusions.

II.3.1 Range resolution improvement using equivalent cross-track apertures

When dealing with SAR systems, one is familiar with the equivalence between the platform motion in the along-track direction (synthetic aperture) and the frequency bandwidth of the corresponding chirp signal in the slow-time domain. If we use the dual form of this equivalence and we apply it to the range dimension, we can consider the frequency bandwidth of the transmitted chirp in the fast-time domain as equivalent to an aperture in the cross-track direction.

The range resolution cell obtained after chirp compression can be directly related to an equivalent aperture of length L_1' seen under an angle $\Delta\theta_1^{eq}$ and aligned in the cross-track direction normal to the sensor-target Line Of Sight (LOS), as sketched in **Figure II-23**. The expression of the equivalent beam width $\Delta\theta_1^{eq}$ as a function of the off-nadir angle θ_1 and of the bandwidth of the transmitted waveform B can be obtained considering that the projection of the equivalent beam in the ground range direction has to be equal to the achievable ground range resolution (r_{gr}):

$$r_{gr} = \frac{\lambda}{2 \cdot \Delta\theta_1^{eq} \cdot cos(\theta_1)} = \frac{c}{2B \cdot sin(\theta_1)} \Rightarrow \Delta\theta_1^{eq} = \frac{\lambda \cdot B \cdot tan(\theta_1)}{c} \qquad \text{Eq. II-5}$$

being λ the carrier wavelength, and c the speed of light.

The range resolution can be increased by incrementing the corresponding equivalent aperture (i.e. incrementing $\Delta\theta^{eq}$). This can be done by considering several SAR sensors observing the same area on the ground with different off-nadir angles, so that their equivalent apertures are adjacent one another. For the purpose of illustration, the sketch of the case of two sensors is reported in **Figure II-24**. As it is apparent, the two equivalent apertures in **Figure II-24** result to be perfectly contiguous, in such a way that the beginning of *aperture 2* exactly coincides with the end of *aperture 1* (i.e. neither overlap nor gap is present between the two apertures). It is worth noticing that a partial overlap between the two apertures will not prevent the possibility to integrate them coherently in order to synthesize a single longer aperture, but it will result in a non-maximum length of the overall aperture and, hence, in a non-maximum range resolution improvement. We will now consider the *optimum* case of two contiguous apertures without partial overlap; partially overlapped apertures will be addressed later on in this paper. By recalling Eq. II-5, it is possible to directly derive a geometrical constraint on the off-nadir angles of the two sensors which guarantees perfect contiguity between the two apertures. To determine such a constraint, we consider a second sensor observing the same area on the ground with an off-nadir angle θ_2, as sketched in **Figure II-24**, and transmitting an almost orthogonal waveform with the same

bandwidth B. Indicating the middle off-nadir angle as $\theta_3=(\theta_1+\theta_2)/2$ and the difference between the two angles as $\Delta\theta = \theta_1-\theta_2$, the expression in Eq. II-5 can be re-written as:

$$\Delta\theta_1^{eq} \cong \frac{\lambda \cdot B}{c} \cdot \left(tan\theta_3 + \frac{\Delta\theta}{2\cos^2(\theta_3)} \right). \qquad \text{Eq. II-6}$$

Similarly, for the second sensor we have:

$$\Delta\theta_2^{eq} \cong \frac{\lambda \cdot B}{c} \cdot \left(tan\theta_3 - \frac{\Delta\theta}{2\cos^2(\theta_3)} \right) \qquad \text{Eq. II-7}$$

Therefore, the off-nadir angles constraint that ensures *optimum*[4] apertures contiguity is:

$$\Delta\theta = \frac{\Delta\theta_1^{eq}}{2} + \frac{\Delta\theta_2^{eq}}{2} = \frac{\lambda B}{c} tan(\theta_3). \qquad \text{Eq. II-8}$$

Referring to Eq. II-6 and to Eq. II-7, it has to be noticed that numerical values of $\Delta\theta_1^{eq}$ and $\Delta\theta_2^{eq}$ are only slightly different, so that they are assumed to be equal to $\Delta\theta^{eq}$ in the following.

Eq. II-8 states a geometrical constraint in terms of off-nadir angles difference that allows two different observations to be contiguous without overlap. It should be clear that this is a needed condition to achieve a longer aperture and therefore a higher range resolution. In addition to that, a proper coherent integration of the two apertures has to be performed, as described in Section II.3.2 .

It is worth to notice that an analogous formulation of the constraint in Eq. II-8 can be derived following the approach described in [5]. In this case, the signals received from the two sensors are demodulated with respect to a common reference signal so that a relative spectral shift (i.e. the wavenumber shift) is experienced between the two down-converted signals (see **Figure II-25**). As it is

4 In case of partial aperture overlap, the equality in equation (4) will become an inequality.

explained in [5], the value of this wavenumber shift Δf depends only on the different off-nadir angles of the two observations θ_1 and θ_2. Specifically, the expression of the wavenumber shift Δf derived in [5] is:

$$\Delta f \cong f_c \frac{\Delta\theta}{\tan(\theta_3)}, \qquad \text{Eq. II-9}$$

being f_c the carrier frequency.

The maximum value of Δf that ensures contiguity between the two spectra is equal to the bandwidth B of the transmitted signal. Substituting B in Eq. II-9, the equivalence between Eq. II-8 and Eq. II-9 can be easily verified.

It has to be noticed that local variations of the incident angle of a particular patch on ground might be experienced, leading to different wavenumber shifts. This can be due to the presence of topography in the observed area, or, in general, to a variation of the incidence angle within the swath moving from the near to the far range. In [7] all these effects have been taken into account, especially for the airborne case. Local variations of the incident angle can be easily taken into consideration if data acquired from different sensors are first range compressed separately and then coherently combined to improve the range resolution. A viable implementation approach is presented in Section II.3.5 .

II.3.2 MIMO SAR system concept based on equivalent cross-track apertures

From the concept presented in the previous Section, if the constellation is composed of active sensors transmitting a set of orthogonal waveforms[5] a MIMO SAR system with improved range

[5] In the analysis conducted within this Section, we will consider the simple case of a MIMO SAR system constituted of 2 SAR sensors (as sketched in Figure 6) transmitting an up- and a down-chirp. An analysis of other suitable waveforms having better characteristics in terms of orthogonality is reported in Section 5

resolution can be obtained. In particular, the sensors are assumed able to receive and separate the echoes from their own transmission from the echoes of other sensors transmissions: by combining the corresponding monostatic and bistatic acquisitions the SAR image with improved range resolution can be obtained. Such an approach has the appealing advantage that the range resolution can be theoretically improved of a factor greater than the number of sensors.

A simple MIMO system made of $S_{REAL} = 2$ SAR sensors is sketched in **Figure II-26**. In particular, the equivalent apertures L_1' and L_2' are obtained by *sensor 1* and *sensor 2* respectively, working as usual monostatic systems. Equivalent aperture L_3' is obtained when *sensor 1* transmits and *sensor 2* receives, thus leading to a bistatic acquisition. Since the bistatic acquisition is equivalent to a monostatic acquisition located on the bisector between the transmit and the receive path, a corresponding frequency shift is experienced in the down-converted bistatic signal, according to Eq. II-9. Therefore, by properly selecting both the two off-nadir angles and the equivalent aperture lengths, it is possible to define a geometry in which the bistatic equivalent aperture L_3' exactly fills the gap between the apertures L_1' and L_2', thus ensuring continuity in the overall aperture. In practical cases, a small overlap between adjacent apertures will be considered to facilitate the recombination processing. Indicating with $\eta<1$ the desired fractional overlapping between adjacent apertures, the overall bandwidth that can be synthesized is equal to $(3-2\eta)B$. This results in a maximum theoretical range resolution improvement factor equal to $(3-2\eta)$. Moreover, the relative spectral shift between the two monostatic acquisitions is equal to $\Delta f=2B(1-\eta)$, thus leading to the following value of $\Delta\theta$:

$$\Delta\theta = \frac{\lambda \cdot 2B(1-\eta)}{c} \cdot \tan\theta_3 \quad . \qquad \text{Eq. II-10}$$

As stated above, we assume the two SAR sensors to transmit an up and a down-chirp, $s_1^{RF}(t_{e,1})$ and $s_2^{RF}(t_{e,2})$ respectively. The expressions of the two transmitted waveforms at Radio-Frequency (RF) are:

$$s_1^{RF}(t_{e,1}) = \exp[+ j\pi f_c \cdot t_{e,1}] \cdot \exp[j\pi k \cdot t_{e,1}^2] \cdot rect_T(t_{e,1})$$

$$s_2^{RF}(t_{e,2}) = \exp[+ j\pi f_c \cdot t_{e,2}] \cdot \exp[- j\pi k \cdot t_{e,2}^2] \cdot rect_T(t_{e,2}),$$

Eq. II-11

where $t_{e,1}$ and $t_{e,2}$ represent the fast times of the first and of the second sensor, k is the chirp rate, T is the pulse length and the function $rect_\Delta(t)$ is equal 1 when $|t| \leq \Delta/2$ and 0 otherwise.

Sensor 2, transmitting $s_2(t_{e,2})$, is supposed to have a second receiving channel matched to the transmission from *sensor 1* ($s_1(t_{e,1})$), thus providing the bistatic signal $s_3(t_e)$.

The signals at RF, received by the two radar systems, have to be projected to a common reference axis, in order to give rise to the corresponding wavenumber shift. In this paper we consider as the common axis a common demodulating reference signal: this is equivalent to the approach presented in [5], where the two signals are projected on the same ground range axis. With reference to the geometry in **Figure II-26**, and by considering the central acquisition (i.e. the bistatic) as a common reference for demodulation, the two monostatic down-converted signals received by *sensors 1* and *sensors 2* can be expressed in the common fast-time domain te as:

$$s_1(t_e) = \exp[+ j\pi\Delta f \cdot t_e] \cdot \exp\left[j\pi k \left(t_e - \frac{2R_1}{c} \right)^2 \right] \cdot rect_T\left(t_e - \frac{2R_1}{c} \right)$$

$$s_2(t_e) = \exp[- j\pi\Delta f \cdot t_e] \cdot \exp\left[- j\pi k \left(t_e - \frac{2R_2}{c} \right)^2 \right] \cdot rect_T\left(t_e - \frac{2R_2}{c} \right)$$

Eq. II-12

Wherein Eq. II-12 the first exponential term represents the wavenumber shift resulting from the demodulation and the second exponential term corresponds to the delayed transmitted chirp.

Indicating with $R_3=(R_1+R_2)/2$ the slant range distance associated with the equivalent bistatic acquisition, the corresponding signal can be expressed as:

$$s_3(t_e) = \exp\left[j\pi k\left(t_e - \frac{2R_3}{c} \right)^2 \right] \cdot rect_T\left(t_e - \frac{2R_3}{c} \right) \qquad \text{Eq. II-13}$$

It is worth to notice that in Eq. II-13 no exponential term corresponding to the wavenumber shift is present, due to the reference signal used for demodulation.

Down-converted signals in Eq. II-12 and Eq. II-13 can be processed coherently to synthesize a signal with improved range resolution, following the scheme of principle sketched in **Figure II-27**. A detailed analytical derivation of range resolution improved signal is reported in the appendix in Section II.3.8 . Simply recalling the Eq. II-23 in Section II.3.8 , the obtained signal with improved range resolution can be expressed as:

$$\begin{aligned} s(t_e) &= \Im^{-1}[S(f_e)] = \Im^{-1}[S_1(f_e)\cdot\Phi_1(f_e)\cdot W_1(f_e) + S_2(f_e)\cdot\Phi_2(f_e)\cdot W_2(f_e) + S_3(f_e)\cdot\Phi_3(f_e)\cdot W_3(f_e)] = \\ &= \Im^{-1}\left[\exp\left(-j\pi\frac{4R_3}{c} f_e \right) \cdot rect_{B+\Delta f}(f_e) \right] = \\ &= \mathrm{sinc}\left[\pi(B+\Delta f)\cdot\left(t_e - \frac{2R_3}{c} \right) \right] \end{aligned} \qquad \text{Eq. II-14}$$

where $\Im^{-1}$ represents the inverse Fourier transform, $S_i(f_e)$ $i=1,2,3$ are the Fourier transforms of Eq. II-12 and Eq. II-13, $\Phi_i(f_e)$ $i=1,2,3$ are proper phase compensation terms representing matched filtering, $W_i(f_e)$ $i=1,2,3$ are window functions needed when the different acquisitions are partially overlapped and finally *sinc(x)* is defined as *sin(x)/x*.

From Eq. II-14, the slant range resolution is easily obtained by evaluating the first null of the *sinc(x)* function. The resulting range resolution after coherent recombination of the signals is equal to $r_{sr} = c/[2(B+\Delta f)]$, and is directly related to the wavenumber shift Δf. The maximum achievable resolution is obtained for the case of optimum apertures contiguity, i.e. when the three observations are adjacent and not overlapped ($\eta=0$, $\Delta f=2B(1-\eta)=2B$). In this case a range resolution improvement factor equal to 3 is obtained. A higher range resolution improvement factor would result in a corresponding wavenumber shift greater than $2B$. This would create gaps in the spectrum of the signal $s(t_e)$, not

making the coherent recombination here presented effective. On the other hand, a partial overlap of the apertures (i.e. $\eta>0$) will not prevent an effective coherent signal recombination, but a range resolution improvement factor lower than the optimum will be experienced. In the case limit of $\eta=1$, the three apertures will be perfectly overlapped (i.e. no relative wavenumber shift, $\Delta f=0$), and the achievable range resolution after signal recombination will be the same as in the monostatic case. It is worth noticing that even if only the two sensors case is here considered, the same principle (and also the same scheme of principle as in **Figure II-27**) can be easily extended without conceptual modifications to constellation of S_{REAL} SAR sensors with $S_{REAL}>2$.

Concerning the above derivation, two different comments are in order. The first one concerns the electromagnetic scattering properties of the targets composing the imaged scene. In fact, we have assumed in the above derivation that all the scatterers in the image behave as a perfect ideal point scatterer showing the same amplitude and phase for all the equivalent sensors, thus neglecting the decorrelation arising from the change of the view angle and from the different scattering properties observed from monostatic and bistatic acquisitions. This results in the assumption of a complete coherence of the shifted versions of the spectrum corresponding to the different sensors. A number of detailed studies have addressed this point in detail with specific attention at the differences between monostatic and bistatic scattering, among which for example [12]. As apparent, this hypothesis is not always verified, especially when operating at high resolution and experiencing a wide change in the observation angle. However, in this paper we focus on cases where the resolution is not extremely high, namely we investigate whether it is possible to increase the overall range resolution by exploiting the signal received by a satellite constellation, where the single sensor has only a limited ground resolution capability. This limitation on the overall range resolution results in a corresponding limit on the angular displacement required between each couple of adjacent real sensors $\Delta\theta$. For example, in an application at X-band a SAR image with overall range resolution equal to 0.5 m could be obtained via MIMO-SAR

with two radar systems transmitting two orthogonal waveforms with $B=100$ MHz observing the scene with mean off-nadir angle value equal to $\pi/3$ and angular displacement between the two platforms lower than 0.035 radians (1.98°). This very limited value of the angular displacement should allow us to consider the shifted spectra from the two monostatic acquisitions as coherent. For the same reason, in such a case, even for complex targets such as ships, aircrafts or ground vehicles, we can assume to be in the pseudo-monostatic RCS (Radar Cross Section) region, [13]. Under this hypothesis the bistatic RCS of the target can be assumed equal to the monostatic RCS measured on the bisector on the bistatic angle. Obviously a moderate degradation of the image quality will be present if the operative conditions do not comply with the previous assumptions (namely in presence of a wide angular separation among the sensors).

The second comment aims at pointing out that the achievement of the expected range resolution improvement requires also the synchronization of the different sensors. The impact of synchronization errors in Multistatic imagery has been already analyzed in [14] and, to solve the problem, different synchronization schemes have been proposed and their performance analysed in [15] or in [16]. Therefore in this section we assume that the synchronization is obtained by applying these schemes and we do not consider this issue in the following.

II.3.3 MIMO SAR constellation configurations

The MIMO configuration is an especially interesting case, since it allows us to reach an improvement in range resolution greater than the number of available platforms. In particular, the MIMO SAR configuration with S_{REAL} platforms can make available a full set of equivalent off-nadir angles, which is upper bounded by the number of platforms plus the number of couples without repetitions, i.e. $S_{REAL}+\binom{S_{REAL}}{2}=\frac{S_{REAL}(S_{REAL}+1)}{2}$, so that also the increase of resolution has this same bound.

As apparent the increase of resolution is directly proportional to the number of independent equivalent off-nadir angles, and the displacement of the SAR sensors has direct implications on the number of independent off-nadir angles, among the $S_{REAL}(S_{REAL}+1)/2$, that are independent (namely non-coincident). Therefore, an appropriate constellation configuration must be considered in order to get close to the bound $S_{REAL}(S_{REAL}+1)/2$. The optimization of the positions of a set of MIMO sensors to provide maximum angular coverage without gaps has been considered for obtaining synthetic aperture images of the surface in [17] for the case of the along-track aperture. For small number of real sensors S_{REAL}, **Tab. II-15** reports the number of effective sensors S_{TOT} available for a continuous aperture without gaps. This directly applies to the case of cross-track apertures.

To obtain the largest possible contiguous global view angle $\Delta\theta_{eq}^{TOT} = S_{TOT}\,\Delta\theta$, using the S_{REAL} sensors for our MIMO SAR application, it is necessary to appropriately displace the real sensors. In particular, the angular displacement required between each couple of adjacent real sensors is reported in the fourth column of **Tab. II-15**, expressed in integer numbers of $\Delta\theta$. The optimization of the selection of off-nadir angles for a set of MIMO sensors to obtain maximum angular coverage $\Delta\theta_{eq}^{TOT}$ is conducted following the optimization procedure presented by Correll in [17]. Specifically, the angular displacements are obtained by increasing by a factor one the number of along-track apertures selected in [17].

As an example, to obtain the global effective angular spacing of $\Delta\theta_{eq}^{TOT} = 9\Delta\theta$ for the MIMO SAR with $S_{REAL} = 4$ real sensors the angular spacings must be assigned as follows: $2\Delta\theta$ between *sensor 1* and *sensor 2*, $4\Delta\theta$ between *sensor 2* and *sensor 3*, $2\Delta\theta$ between *sensor 3* and *sensor 4*. As evident, the choice of the basic displacement angle $\Delta\theta$ is essential both to avoid the gaps in the global MIMO SAR angle ($\Delta\theta \le \Delta\theta^{eq}$), and to achieve the maximal resolution improvement (largest possible value of $\Delta\theta$). As apparent the optimum value is $\Delta\theta = \Delta\theta^{eq}$.

Figure II-28 shows the extension of the MIMO SAR case of Section II.3.2 to higher values of S_{REAL}, up to $S_{REAL}=10$, using the configurations in **Tab. II-15**. In particular, the red and the white squares respectively represent the real and the fictitious cross-track angular apertures used in the distributed configuration, where the term "real aperture" indicates the equivalent cross-track aperture for the sensors operating in monostatic configuration, whereas "fictitious aperture" corresponds to bistatic configurations based on different transmit and receive real sensors.

In **Figure II-29**, the value of the maximum range resolution improvement is shown for both the Multistatic distributed SAR and the MIMO distributed SAR. As it is apparent, in the Multistatic case the maximum achievable range resolution improvement increases linearly with the number of platforms S_{REAL} since $S_{TOT} = S_{REAL}$. In the MIMO case the maximum can be considerably higher than the number of platforms S_{REAL} since the gain S_{TOT} of the MIMO configuration, that is the number of equivalent sensors considered, increases faster as the number of platforms increases.

The quantification of the improvement made available by the MIMO configuration with respect to the Multistatic configuration is provided by the ratio S_{TOT}/S_{REAL}, that is reported in the fifth column of **Tab. II-15**. As apparent, for larger values of S_{REAL} the improvement increases, remaining below the quantity $(S_{REAL}+1)/2$, which represents an upper bound to the potential improvement. It is interesting to observe that as S_{REAL} increases it is more difficult to identify configurations for the real sensors such that the couples are independent, so that the highest achievable number of contiguous apertures is lower than the bound. This is easily observed by comparing columns 2 and 3 of **Tab. II-15**, while the relative loss with respect to the bound is reported in its last column, showing a slow increase to about 30% when using 11-14 platforms. The results in [17] show that in the limit for $S_{REAL}\rightarrow\infty$ the value of $S_{TOT}\rightarrow S_{REAL}^2$ so that the MIMO improvement tends to be quadratically related to the number of sensors, similarly to the bound, and the ratio S_{TOT}/S_{REAL} goes asymptotically to S_{REAL}.

Based on the efficient collection geometries for the MIMO SAR reported in column 4 of **Tab. II-15**, it is possible to synthesize equivalent contiguous cross-track apertures S_{TOT} times larger than the equivalent aperture of the single sensor. Obviously, the sequence of apertures reported in column 4 is easily converted in difference of off-nadir angles, that must be imposed to the sensors when jointly observing the same area to obtain the SAR image with S_{TOT} times higher resolution. A similar approach has been exploited differently in [18]-[19] for a multi-platform ISAR case.

In the practical case, the presence of non-flat topography implies that the above discussion should be presented in terms of the local incidence angle, instead of the off-nadir angles. This also applies for the well known differences in the incidence angle between near-range and far-range inside a typical SAR image. Due to the non-constant slope of the terrain, it is clear that to be sure of avoiding gaps in the total equivalent aperture, some margins of overlap should be maintained, so that, as for the case of $S_{TOT}=2$, the maximum improvement is limited by $S_{TOT} - (S_{TOT}-1)\eta$, being η the fractional overlap.

II.3.4 MIMO SAR waveforms

As well known, the up and down chirp waveforms are not fully orthogonal, and the presence of their non-zero cross-correlation produces a degradation of the image quality. In particular, the sidelobe structure and level of each of the single images is affected by this selection, so that the increase in resolution for the strong scatterers is paid off with a degradation in the peak to sidelobe ratio and in the integrated sidelobe ratio levels. The same type of problems of the up and down chirp waveforms are experienced by set of waveforms that are not fully orthogonal.

Different possible solutions could be considered to obtain fully orthogonal signals, based on a separation of the signals in the temporal domain. This can be achieved in two different ways:

A. by using a (low) pulse repetition frequency (PRF) such that the range ambiguous window is at least twice the slant range swath (S_R), intended as the antenna footprint on ground in the range dimension.

By properly alternating the transmissions of the waveforms emitted by the two platforms, it is possible to obtain that the corresponding returns are made fully orthogonal in the fast time domain (i.e. the transmissions from the two platforms are interleaved so that at each receiver, for every fast time instant, the received signal is constituted by radar echoes generated by a single transmission). With reference to the geometry sketched in **Figure II-24**, the timing of the returns, required by this first strategy, is sketched in **Figure II-30**. The sketch includes the case of airborne SAR (with range ambiguity order $n=n'=0$) - where the echo is typically assumed to be received with a delay smaller than the pulse repetition time (PRT), - and satellite SAR (with $n,n' \neq 0$) - where the echo is typically assumed to be received with a delay greater than the PRT. This strategy appears to be a natural approach for airborne radar that typically do not require high PRFs due to the slow motion of the platform. In this case ($n=n'=0$), for the timing diagram to be consistent the following inequalities must be verified:

$$\begin{aligned} T &< \max\left\{\frac{2R_1}{c}, \frac{2R_2}{c}, \frac{R_1+R_2-2\Delta}{c}\right\} \\ \Delta T &> \max\left\{\frac{R_1+R_2}{c}, \frac{2(R_1-\Delta)}{c}\right\} + \frac{2S_R}{c} + T \\ PRT &> \Delta T + \max\left\{\frac{R_1+R_2}{c}, \frac{2(R_2-\Delta)}{c}\right\} + \frac{2S_R}{c} + T \end{aligned} \qquad \text{Eq. II-15}$$

Specifically the first line of Eq. II-15 implies that:

- ✓ platform 1/2 has completed its own transmission (TX1/2) when the corresponding echo arrives at RX1/2 (Echo to TX1/2);
- ✓ at platform 1/2 the transmission of platform 2/1 (TX2/1) and the corresponding echo (Echo to TX2/1) do not overlap;

the second line of Eq. II-15 implies that:

- ✓ at platform 1 the echo concerning its own transmission (Echo to TX1) does not overlap with the transmission of platform 2 (TX2);
- ✓ platform 2 has completed the reception of the echo corresponding to the transmission of platform 1 (Echo to TX1) when starting its own transmission (TX2);

and finally the third line implies that:

- ✓ platform 1 has completed the reception of the echo corresponding to the transmission of platform 2 (Echo to TX2) when starting its own new transmission (TX1);
- ✓ at platform 2 the echo concerning its own transmission (Echo to TX2) does not overlap with the transmission of platform 1 (TX1).

By combining the second and third line of Eq. II-15 we get

$$PRT > \max\left\{\frac{R_1 + R_2}{c}, \frac{2(R_1 - \Delta)}{c}\right\} + \max\left\{\frac{R_1 + R_2}{c}, \frac{2(R_2 - \Delta)}{c}\right\} + \frac{4S_R}{c} + 2T \qquad \text{Eq. II-16}$$

As apparent from Eq. II-16, this strategy leads to a PRF slightly lower than half of the PRF for a standard SAR (giving rise to about the same equivalent PRF perceived by the two receivers due to the two transmitters being alternatively activated). This typically reduces of a factor two the amount of pre-summing applied to the collected data.

A similar analysis can be applied to the satellite-based case, taking into account the presence of multiple PRTs inside the echo delay time. Therefore, a similar conclusion of slightly less than half of the standard PRF is obtained for the satellite case, with the more complex definition of appropriate reception windows. The proposed approach can be applied in satellite based spotlight SAR if the sensor is not already designed to collect the "maximum amount of information", [20], namely if the swath in slant range, defined from the antenna footprint, is not shorter than half of the inverse of the frequency bandwidth of the echoes received by the antenna.

B. The other possibility is to separate the echoes in the Doppler frequency domain, by exploiting the azimuth phase coding approach, [21]-[22]. In this case, instead of using a lower PRF, we can maintain the initial PRF with the two sensors and make so that the echoes to TX1 and TX2 arrive at both sensors overlapped in time. However, TX1 applies a phase coding to the transmitted sequence of pulses having the following expression:

$$c(n) = e^{-j\frac{\pi}{2}n^2}, \quad n = 1,.....,N \qquad \text{Eq. II-17}$$

where N indicates the overall number of transmitted pulses within the synthetic aperture. The same sequence is used to apply phase coding in transmission to TX2, but with a delay of one sample. When the two overlapped echoes are received by each one of the receivers and the transmission phase is compensated for, the echoes to the transmitted pulse are received unaffected, while the echoes to the waveform generated by the other transmitter is shifted in the slow-time frequency domain. By filtering in this domain, both images can be separated and focused separately.

As apparent, this requires that the surface echoes received by each platform have a frequency bandwidth that occupies not more than half of the PRF. If this is not the case, the spectral shift provided by the azimuth phase coding do not lead to echoes non-overlapped in the frequency azimuth domain.

Again this is a more typical condition for the airborne SAR sensors, but it can be also applied to spaceborne SAR, provided that not the full exploitation of the imaging capability of the platform is performed. In practice it is required that at the maximum admissible PRF to avoid range ambiguities, the echoes bandwidth does not exceed the half of the frequency span. This approach has the advantage of requiring a slightly lighter control of the alternating timing of the two platforms, while using a higher PRF and thus producing a higher data rate.

It is interesting to notice that essentially the applicability of the perfect separation (fully orthogonal waveforms) requires that the full imaging capabilities for assigned antenna size are not used, namely using only a smaller (i.e. about half size) swath in range (case A) or a lower resolution (i.e. about factor of two worse) in the azimuth direction (case B) than for a sensor that collects images at its full potentialities but without an increase of ground range resolution larger than the number of sensors. This is the price to be paid so that the echoes can be perfectly separated. The alternative is to use partially correlated signals (as up and down chirps) and accept the resulting image quality degradation.

For the more general case of S_{REAL} platforms, there are many usable sets of nearly orthogonal waveforms, among which an extension of the set considered for the up-down chirp. Specifically, using linear frequency modulation in **Figure II-31** we show that a set of 4 waveforms with low correlation can be obtained by using: an up-chirp, a down-chirp and two triangular frequency modulated waveforms, [23].

As apparent this set of waveforms suffers the same problem of image degradation discussed before, but gives the advantage of not requiring potential reduction of the imaging capability of the single sensor.

As for the case of $S_{REAL} = 2$, it is possible to obtain fully orthogonal waveforms by separating the returns either A) in slow-time or B) in Doppler frequency:

A. Define an appropriate timing as an extension of the approach in A) to more than two sensors so that the S_{REAL} returns to the S_{REAL} different transmissions are not overlapped in time. This obviously requires to use, for the single transmitter, a PRF about S_{REAL} time slower than the maximum value allowed to avoid range ambiguities. This is possible only if the frequency bandwidth in the slow time domain is small enough.

B. Use an appropriate azimuth phase coding, as an extension of approach B) above, to more than two sensors so that the S_{REAL} returns to the S_{REAL} different transmissions are discriminated in the frequency azimuth domain. For example this can be obtained using the sequence:

$$c(n) = e^{-j\frac{\pi}{M}n^2}, \quad n = 1,.....,N \qquad \text{Eq. II-18}$$

where now $M = \lfloor PRF / B_{Doppler} \rfloor$. This is valid provided that again the PRF is high enough so that the frequency of the returns occupy not more than a fraction $1/S_{REAL}$ of it.

As discussed for the case of two sensors, this typically applies very easily to airborne sensors (that can afford a significant presuming), while it is more critical for space-base SAR sensors. In fact it requires that the amount of information by the single sensor is $1/S_{REAL}$ of the maximum possible.

II.3.5 MIMO SAR processing techniques

The practical implementation of the MIMO SAR processing required to achieve in practice the desired increase in the range resolution is clearly based on the scheme of principle described in Section II.3.2 . However, it must be extended to operate with the full SAR image swath, thus taking into account all real effects. In principle, two different approaches can be followed to obtain a full resolution SAR image:

- Centralized Technique: the radar data from the 3 (S_{TOT}) channels can be properly pre-processed and coherently combined, so as to obtain an extended data set. Thereafter, the extended data set is focused by using an appropriate 2D single channel SAR processing scheme: this is basically shown in a preliminary work of the authors reported in [24].

- Decentralized Technique: first 3 (S_{TOT}) low resolution images are independently focused, by applying separate focusing techniques, and then the 3 (S_{TOT}) images are combined coherently (after appropriate registration if necessary) to achieve the final image with higher ground range resolution.

The two approaches are separately detailed in the following.

MIMO SAR Centralized Focusing Technique

The MIMO SAR centralized focusing technique is the natural two-dimensional extension of the recombination processing described in Section II.3.2 . The processing scheme needed to combine the different acquisitions and obtain the improved range resolution is shown in **Figure II-32**. Its main steps are the following: 1) the raw down-converted data from the i-th channel are Fourier transformed in the range dimension; 2) for each channel the matched filter is applied by multiplying the Fourier transformed signal by $S_i^*(f)$, thus performing the range compression; 3) the channel is realigned in phase and time to a reference common to the three channels; 4) the three channels are combined in frequency domain to obtain the overall synthetic bandwidth. If adjacent spectra are partially overlapped (η<1) a frequency selection step has to be applied previously to combination; 5) the inverse Fourier transform can finally be applied to obtain the high resolution range profiles. The output of this coherent recombination procedure is the input of the subsequent single channel focusing processing chain: at this point any 2D synthetic aperture radar focusing technique would be quite adequate to perform the appropriate 2D focusing. It is worth to notice that the phase multiplication with $S_i^*(f)$ in step 2) removes the phase quadratic term (i.e. the chirp) from signals received at each channel. As a consequence, the recombined signal after step 5) is de-chirped or, which is equivalent, range compressed. To allow a proper elaboration of this recombined signal with a conventional 2D SAR focusing technique such as the Chirp Scaling Algorithm ([25]-[26]), a proper elaboration of the signal has to be performed. Specifically, the quadratic phase term has to be re-inserted in the recombined signal. We will refer to this operation as a *rechirping*, see **Figure II-32**. To limit the computational burden, the *rechirping* can

be applied in frequency domain before the inverse Fourier transform. However, also other techniques, such as the Frequency Scaling Algorithm, [27], or the Range Migration Algorithm, [28], could be applied as well, each one of which might require a different specific pre-adaptation step to the recombined signal. It is worth to notice that in the centralized focusing technique, the multi-sensor data recombination is performed before range compression. This leads to a processing scheme effective if and only if no local variations of the incident angle are experienced over the swath (i.e. constant wavenumber shift over the image).

MIMO SAR Decentralized Focusing Technique

As already mentioned in Section II.3.1 , local variations of the incident angle within the observed area might result in non negligible variations of the corresponding wavenumber shift (i.e. *range dependent* wavenumber shift). These variations may be experienced either in airborne scenarios (due to relatively low platform height and wide antenna elevation patterns), and/or if topography is present in the observed area (i.e. non flat observed terrain). In the following, without lack of generality, we will refer to local variations of the incident angle from near to far range for a flat Earth observed area. Nevertheless, the proposed technique can be directly extended to the presence of topography in the observed area without any conceptual modification. In this latter case, a Digital Elevation Model (DEM) has to be considered, to retrieve topographic information of the observed area.

Regardless of the reason which causes variations of the wavenumber shift with range, it is clear that a range dependent wavenumber shift requires a range dependent coherent signals recombination, which can not be performed prior to range compression over the single acquisition (i.e. range compression at *low resolution*). Once that a coarse range compression has been performed, multi-channel echoes coming from different ranges can be distinguished and processed separately according

to the corresponding wavenumber shift. After that, recombined data have to be merged together to obtain the final image with improved range resolution.

A viable implementation of the aforementioned scheme is presented in the decentralized technique, sketched in **Figure II-33**. Specifically, we propose to first process separately the multi-channel data corresponding to different acquisitions, thus obtaining S_{TOT} different range compressed images at *low resolution* (i.e. range resolution corresponding to the single acquisition). After that, a sliding rectangular window is passed over each image, so that a single range bin (i.e. a single multi-channel snapshot) can be extracted for each different shift of the sliding window. Multi-channel snapshots can then be processed separately each one of them according to the corresponding wavenumber shift, and combined to obtain the final image with improved range resolution. The processing to coherently combine multi-channel data from a single range bin is exactly the same as in the centralized technique (see **Figure II-32**), except for the phase multiplication with $S_i^*(f)$, which has not to be considered, since data are already range compressed. Obviously the phase and time channel realignment and the frequency selection steps have to be tailored to the specific wavenumber shift. If the rectangular sliding window shifts one range bin per one range bin, as considered up to know, the resulting decentralized technique is somehow *optimal*, since each range bin is processed exactly according to its wavenumber shift. However, such an optimal processing scheme might require a high computational load, hence it will not be considered in the following. Nevertheless, a sub-optimal decentralized approach can be considered to ensure both low performance losses w.r.t. the optimal approach and affordable computational burden. Specifically, a sub-optimal decentralized approach can be directly derived from the optimal one, by windowing R adjacent range bins each time ($R>1$), and by applying the same coherent recombination processing to all the R range bins. As a consequence, the whole range extent of the image will be divided in several strips, each one processed separately. In the

following, a given range strip will be processed according to the wavenumber shift experienced by the central range bin of that strip.

After multi-channel data recombination, the different *strips* are placed side by side and, finally, the high-resolution image is obtained. A block diagram of the resulting sub-optimal decentralized approach is sketched in **Figure II-33**. As it is apparent, the optimal decentralized approach can be obtained by simply choosing $R=1$ (i.e. only one range cell per strip), while the centralized technique can be obtained by placing all the range bins of the image in the same *strip*.

It is clear that processing several range bins together (that is, according to a common wavenumber shift), will cause some degradations in the resulting final focused image mainly in terms of degraded range resolution and increased side-lobes level. This is the price to be paid for a reduction of the overall computational burden. Therefore, a main issue in the implementation of the sub-optimal decentralized technique is the evaluation of the range resolution losses (w.r.t. the optimal decentralized case) versus R (i.e. the number of range bins per *strip*). If all the range bins within a given strip are processed according to the wavenumber shift of the central range bin of that strip, the higher range resolution losses will be experienced for the range bins at the edge of the strip. Therefore, we define the *Range Resolution Loss* (*RRL*) as the ratio between the range resolution measured at the edge of the strip by applying the sub-optimal decentralized approach and the range resolution measured at the same range bin by applying the optimal decentralized technique. Obviously, *RRL* depends both on the range and on R (range strip size). Since the dependency of *RRL* on range is negligible with respect to its dependency on R, only this second one is considered in the following. By setting an acceptable level of *RRL*, the number of range bins per strip (i.e. the value of R) can be derived.

II.3.6 MIMO SAR performance analysis

Preliminary Point Spread Function Analysis

A preliminary range Point Spread Function (PSF) analysis has been conducted only along the range dimension to show the effectiveness of the MIMO scheme of principle. This first analysis aims at testing the effective slant range resolution improvement using $S_{REAL} = 2$ real sensors, while varying the cross-track sub-apertures fractional overlap η. Obtained results are reported in **Figure II-34**, together with measured slant range resolutions (r_{sr}) for a transmitted chirp bandwidth $B=30\ MHz$. In particular, it is easy to observe that using a single platform, a resolution of $5\ m$ is achieved with the single SAR platform, whereas using the $S_{REAL} = 2$ MIMO SAR, a maximum resolution of $5/3=1.67\ m$ is obtained avoiding overlap (namely for η=0). The results obtained using the same scheme of principle with a partial overlap, provide a slightly lower increase of resolution equal to $5/(3-2\eta)$. This clearly shows that using the presented geometrical platform configuration and scheme of principle, the desired increase in the range resolution is directly achieved.

MIMO Techniques Performance Analysis

To analyze the performance of the MIMO SAR technique, we consider the case of S_{REAL} = 2 platforms (S_{TOT} = 3) and we refer directly only to the decentralized technique, which is able to take into account the variation of the wavenumber shift inside the imaged scene. As mentioned in Section II.3.5 , we consider the processing using the same correction parameters inside range cell strips of assigned dimensions. To determine the number of range bins per strip *R*, an evaluation of *RRL* versus *R* has been conducted, both for an airborne system and for a spaceborne system observing an area on ground with no topographic features. Main system parameters used are reported in **Tab. II-16**, whereas obtained results are reported in **Figure II-35**. As is apparent, when an airborne system is considered, limited range resolution degradation is experienced only for very few range bins within each strip, namely 2 or 3. Therefore, in this case the decentralized approach has to be applied almost on a range cell by range cell mode. On the other hand, when a spaceborne system is considered (see **Figure II-35**), up to 100

adjacent range cells can be processed with the same phase compensation term, if range resolution degradation within 10% can be tolerated. This makes the sub-optimal decentralized approach (namely strip by strip, instead of range cell by range cell) an appealing technique to reduce the overall computational burden. It is worth to notice that, even in the spaceborne case, by applying the sub-optimal decentralized technique, the partition of the whole image in different stripes, has to take into account also the topographic information over the observed area. This may lead to a reduction of the maximum allowable number of adjacent range cells to be processed together, with respect to the analysis conducted above.

Following the results of the analysis above, two different simulations have been conducted. In the first simulation, the optimum (namely range cell by range cell) decentralized approach described above has been considered. The first simulation is referred to a sample airborne case study with two X-band SAR sensors working in stripmap mode observing the same area on the ground with angles θ_1 and θ_2, for a flat Earth geometry (see **Tab. II-16**). The selected off-nadir angles guarantee a spectral overlap corresponding to $\eta = 0.15$. Moreover, it is assumed that *sensor 1* transmits an up-chirp, while *sensor 2* transmits a down-chirp (both with bandwidth $B = 30\ MHz$ so that a ground range resolution equal to *5.8* meters is obtained for the single sensor). This ensures almost waveform orthogonality, allowing each sensor to separate the monostatic from the bistatic contributions. The observed scene has dimensions $100m \times 100m$ (azimuth × ground range) in which six different point-like targets have been placed. In particular, four targets are placed at the corners of the squared scene, one at the scene center and the sixth is separated 4 meters from the scene center (same azimuth cell). We expect that the last target will not be discriminated with respect to the scene center if a conventional single channel SAR processing is performed, whereas we expect that the range resolution improvement allows us to discriminate them. **Figure II-36** shows the focused scene with improved range resolution as it is obtained after the application of the MIMO optimum decentralized technique, showing clearly that all the six scatterers

have been correctly imaged. To demonstrate the achieved range resolution improvement, we report in **Figure II-37** and in **Figure II-38** the point target responses of both the conventional (single sensor) SAR and the MIMO SAR focused images for azimuth equal to *0* and *100m*, respectively. As it is apparent from these figures the use of the proposed MIMO SAR scheme allows us to move from a ground range resolution of about *5.85m* in the single-sensor case to about *2.17m* in the multi-sensor case with a range resolution improvement equal to $3-2\eta=2.7$. The resolution improvement allows to resolve scatterers not resolved in the conventional case, as apparent from **Figure II-37**.

The second simulation refers to a sample spaceborne case study, with two SAR sensors working in stripmap mode. As in the previous case, *sensor 1* and *sensor 2* transmit an up and a down chirp with a bandwidth of $B = 30\ MHz$, see **Tab. II-16**. For this second simulation, the sub-optimal (namely range strip by range strip) decentralized MIMO SAR technique has been considered. In particular, following the analysis conducted in Section II.3.5 , the number of range bins per strip it is set in order to keep the *RRL* within *10%*. This results in about $R=100$ adjacent range bins to be processed together. Simulations have been conducted to evaluate the defects on the range response related to the implementation of the sub-optimal decentralized technique w.r.t. the optimal one. To do this, a worst case situation has to be considered: target located at the edge of a given strip and coherent recombination conducted accordingly to the wavenumber shift of the central range bin of that strip. Obtained result is reported in **Figure II-39**. To allow the analysis of the resolution improvement, as in the airborne case, in **Figure II-40** the MIMO SAR range main cut is shown and compared to the conventional single-channel SAR response for the worst case situation inside the considered swath. As apparent, also in this case the desired resolution improvement is clearly obtained. The resulting effects due to the application of a constant wavenumber shift within a given strip are the increased range resolution and increased side lobe level. It is worth to notice once again, that these defects are not present if the optimal decentralized

technique is applied (see previous simulation) and, hence, they are directly related to the sub-optimal implementation of the decentralized technique. These defects represent the price to be paid for a reduced overall computational load.

II.3.7 Conclusions

In this section a MIMO technique has been presented for range resolution improvement using a constellation of SAR systems. The constellation configuration has been determined in correspondence with the sensor parameters so as to achieve the highest increase in the ground range resolution. The principle is based on the idea that the waveform with assigned frequency bandwidth transmitted by each SAR sensor is equivalent to a specified cross-track aperture. Depending on the geometry, the different monostatic acquisitions may result in non-contiguous cross-track apertures. However, by exploiting also the bistatic acquisitions, it is possible to achieve additional effective apertures that fill the gaps between the non-contiguous monostatic acquisitions, possibly with a partial overlap. This provides an overall continuous aperture sensibly larger than the product of the aperture of the single platform and the number of platforms.

Therefore the strength of this approach resides in the possibility to increase the range resolution of a factor greater than the number of SAR sensors. Specifically with two SAR sensors a range resolution improvement up to a factor 3 can be obtained, while for S_{REAL} platforms the increase is upper bounded by $S_{REAL}(S_{REAL}+1)/2$.

It has to be noticed that the practical implementation of the proposed MIMO SAR technique requires some constraints to be met. First of all, the improvement of range resolution via the proposed MIMO SAR concept requires the strict control of the acquisition geometries concerning the different satellite/airborne sensors in order to guarantee a continuous synthesized bandwidth. Moreover the achievement of the expected range resolution improvement requires also the application of proper

strategies to guarantee the synchronization of the different sensors in order to make possible the distributed imaging. The waveforms transmitted by the different radar systems need also to be properly selected: specifically, as stated above, the applicability of the perfect separation (fully orthogonal waveforms) requires that the full imaging capabilities for assigned antenna size are not used at the single sensor level. This is the price to be paid so that the echoes can be perfectly separated. The alternative is to use partially correlated signals (such as up and down chirps as considered in this paper) and accept the resulting image quality degradation. Finally a complete coherence of the shifted versions of the spectrum corresponding to the different sensors has been assumed. This assumption can be reasonable for the cases considered in this paper where the single sensor resolution is not extremely high requiring a limited angular displacement between each couple of adjacent real sensors. Obviously a moderate degradation of the image quality will be present if the operative conditions do not comply with the previous assumptions (namely in presence of a wide angular separation among the sensors).

Other than demonstrating the basic resolution increment principle, appropriate focusing techniques have been devised, that are able to deal with both typical airborne and spaceborne SAR geometries, and can take into account the local topography. To this purpose the decentralized solution has been shown to be preferable with respect to the centralized one and its effectiveness has been demonstrated against simulated data.

II.3.8 Appendix 1

After range Fourier transform, the three signals in Eq. II-12 and in Eq. II-13 can be expressed as:

$$S_1(f_e) = \exp\left\{-j\pi\left[\frac{(f_e - \Delta f/2)^2}{k} + 2(f_e - \Delta f/2)\frac{2R_1}{c}\right]\right\} \cdot rect_B(f_e - \Delta f/2) \qquad \text{Eq. II-19}$$

$$S_2(f_e) = \exp\left\{+ j\pi\left[\frac{(f_e + \Delta f/2)^2}{k} - 2(f_e + \Delta f/2)\frac{2R_2}{c}\right]\right\} \cdot rect_B(f_e + \Delta f/2)$$

$$S_3(f_e) = \exp\left[- j\pi\left\{\frac{f_e^{\,2}}{k} + \frac{4 f_e R_3}{c}\right\}\right] \cdot rect_B(f_e)$$

In the range frequency domain, we can perform separately for the three signals the compensation of the quadratic phase term together with the removal of the additional phase terms. This is obtained by multiplying $S_1(f_e)$, $S_2(f_e)$, and $S_3(f_e)$ with the following exponential terms:

$$\Phi_1(f_e) = \exp\left\{+ j\pi\left[\frac{(f_e - \Delta f/2)^2}{k} - \Delta f\,\frac{2R_1}{c} + \frac{4(R_1 - R_3)}{c} f_e\right]\right\}$$

$$\Phi_2(f_e) = \exp\left\{- j\pi\left[\frac{(f_e + \Delta f/2)^2}{k} - \Delta f\,\frac{2R_2}{c} - \frac{4(R_2 - R_3)}{c} f_e\right]\right\} \qquad \text{Eq. II-20}$$

$$\Phi_3(f_e) = \exp\left\{j\pi\,\frac{f_e^{\,2}}{k}\right\}$$

Subsequently, after windowing of the spectra with rectangular functions, the three signals can be recombined, thus leading to $S(f_e)$:

$$\begin{aligned} S(f_e) &= S_1(f_e)\cdot\Phi_1(f_e)\cdot W_1(f_e) + S_2(f_e)\cdot\Phi_2(f_e)\cdot W_2(f_e) + S_3(f_e)\cdot\Phi_3(f_e)\cdot W_3(f_e) = \\ &= \exp\left[- j\pi\,\frac{4R_3}{c} f_e\right]\cdot rect_{B+\Delta f}(f_e) \end{aligned} \qquad \text{Eq. II-21}$$

where the window functions can be expressed as:

$$W_1(f_e) = rect_{(1-\eta/2)B}\left[f_e - \frac{1}{2}\left(\Delta f + \eta\frac{B}{2}\right)\right]$$

$$W_2(f_e) = rect_{(1-\eta/2)B}\left[f_e + \frac{1}{2}\left(\Delta f + \eta\frac{B}{2}\right)\right] \qquad \text{Eq. II-22}$$

$$W_3(f_e) = rect_{(1-\eta)B}[f_e]$$

By applying a range inverse Fourier transform,, the following expression is obtained for the Point Spread Function (PSF):

$$s(t_e) = \mathrm{sinc}\left[\pi\left(B + \Delta f\right)\cdot\left(t_e - \frac{2R_3}{c}\right)\right]. \qquad \text{Eq. II-23}$$

where the *sinc(x)* function is defined as *sinc(x)=sin(x)/x*.

II.4 *Figures*

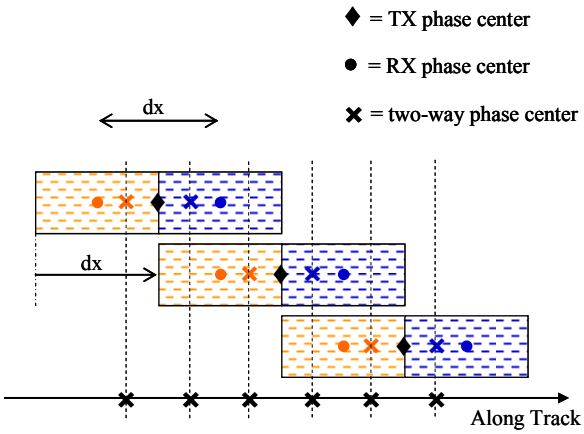

Figure II-1 Uniform sampling along the synthetic aperture

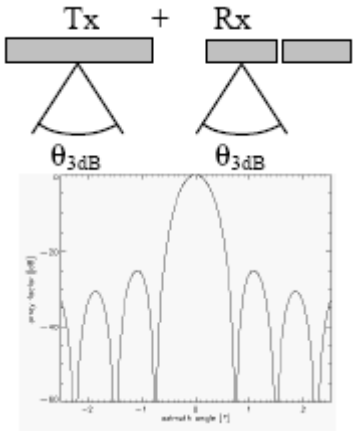

Figure II-2 Two-way pattern from wide TX and wide RX

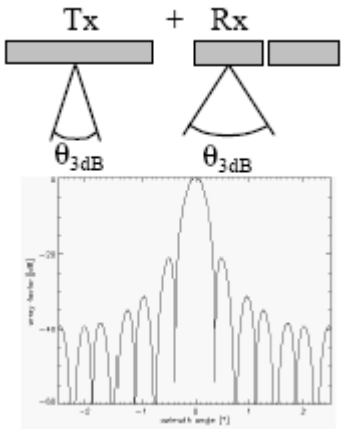

Figure II-3 Two-way pattern from narrow TX and wide RX

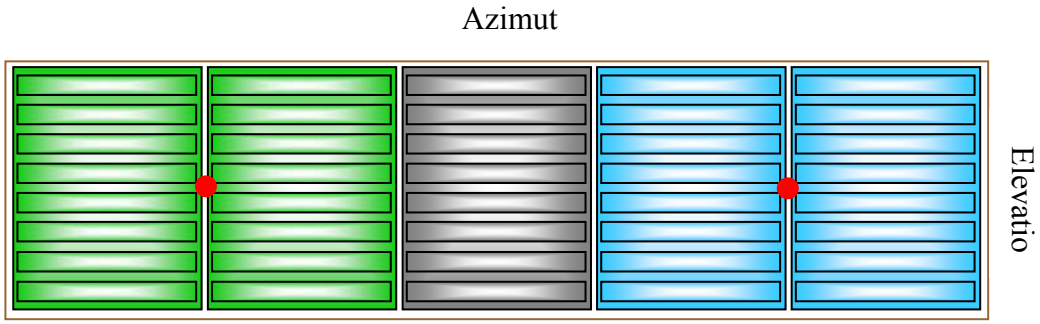

Figure II-4 COSMO5x8 SPAN2b

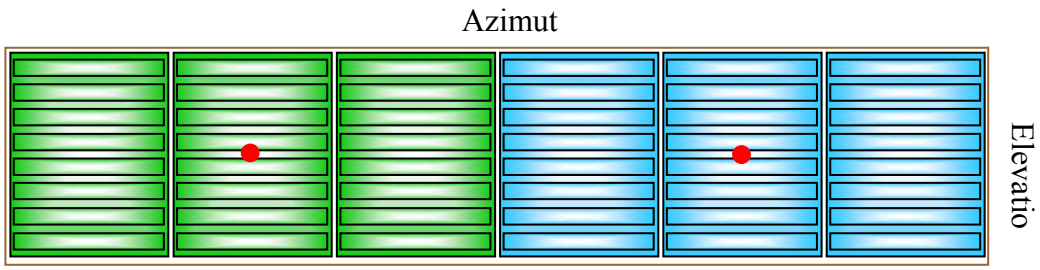

Figure II-5 COSMO6x8 SPAN2c

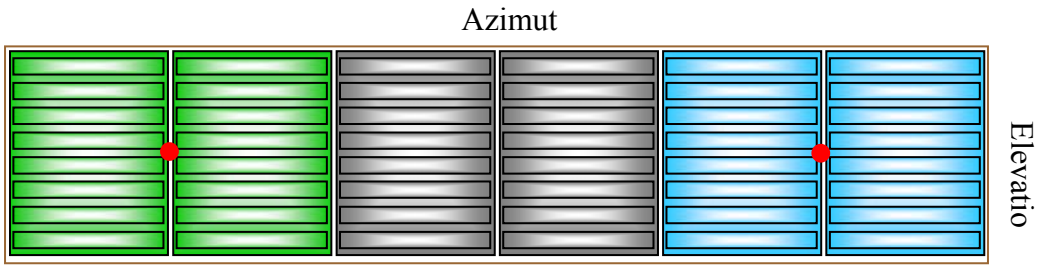

Figure II-6 COSMO6x8 SPAN2b

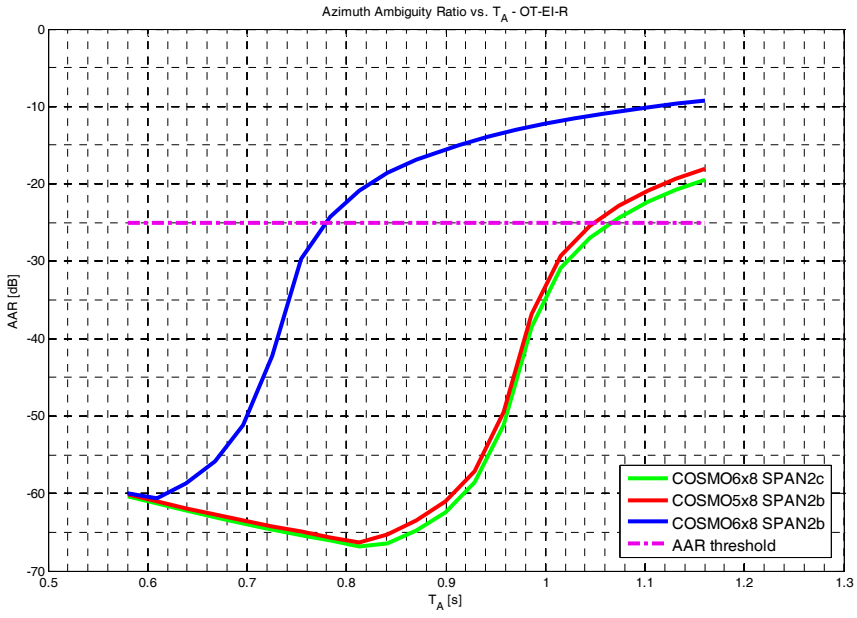

Figure II-7 AAR vs. T_A for COSMO6x8 SPAN2b, COSMO5x8 SPAN2b and COSMO6x8 SPAN2c in EI-R

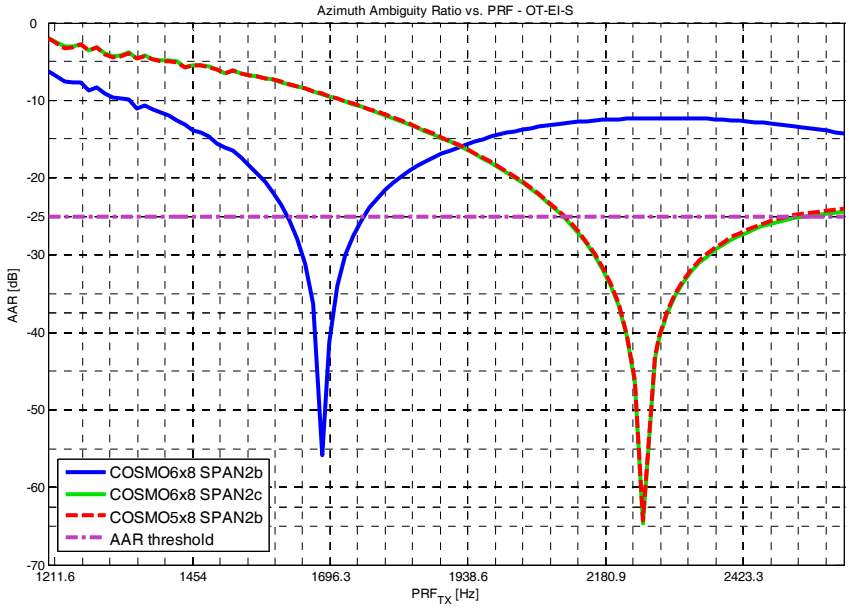

Figure II-8 AAR vs. PRF for COSMO6x8 SPAN2c, COSMO6x8 SPAN2b and COSMO5x8 SPAN2b in EI-S

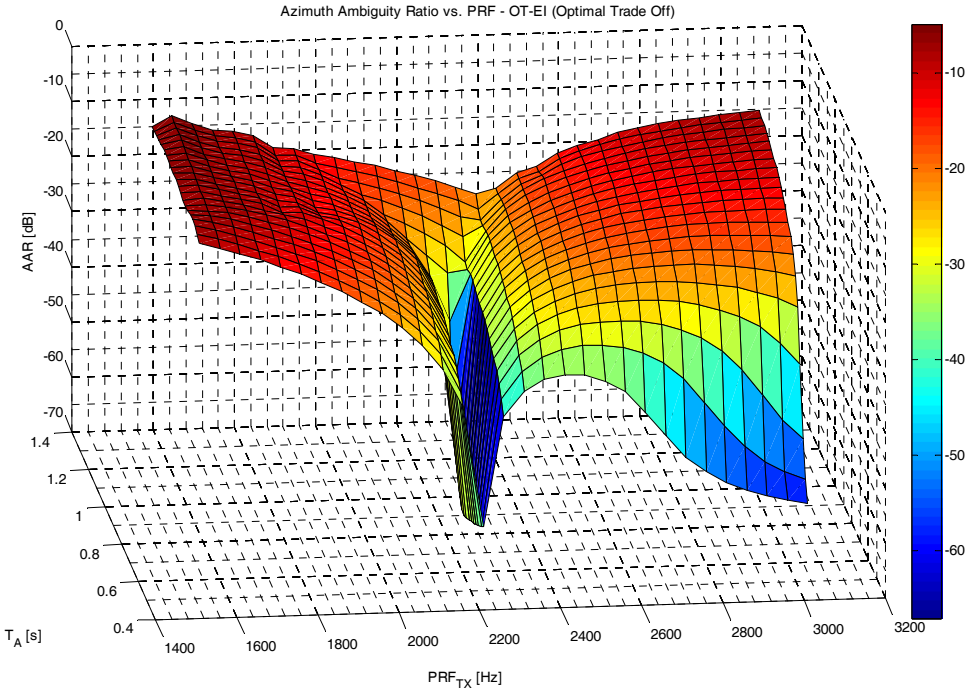

Figure II-9 AAR versus (T_A, PRF) for COSMO5x8 SPAN2b

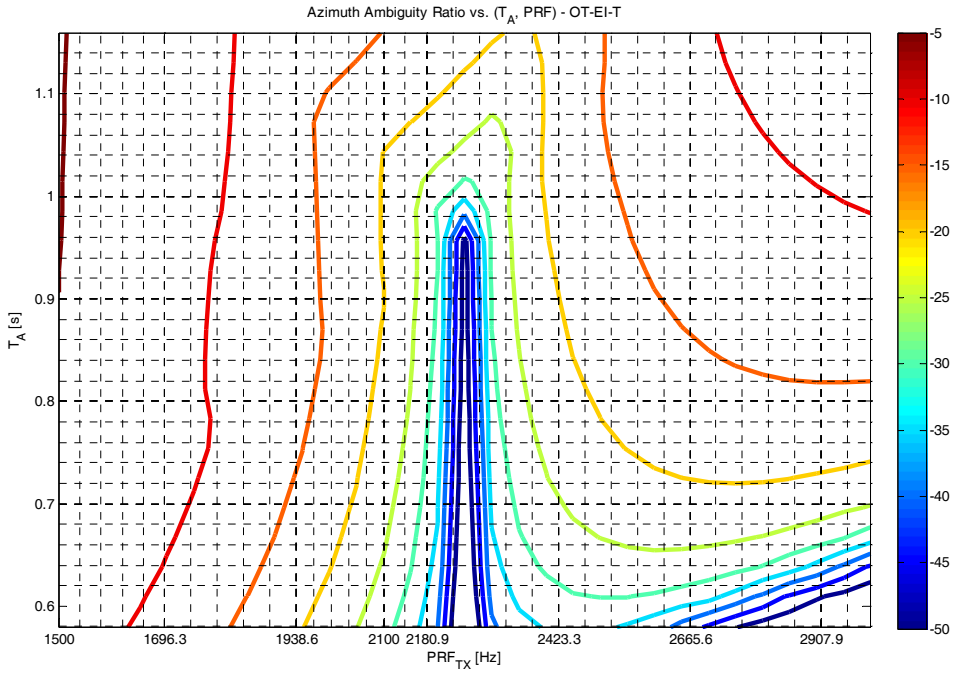

Figure II-10 AAR versus (T_A, PRF) for COSMO5x8 SPAN2b (contour plot)

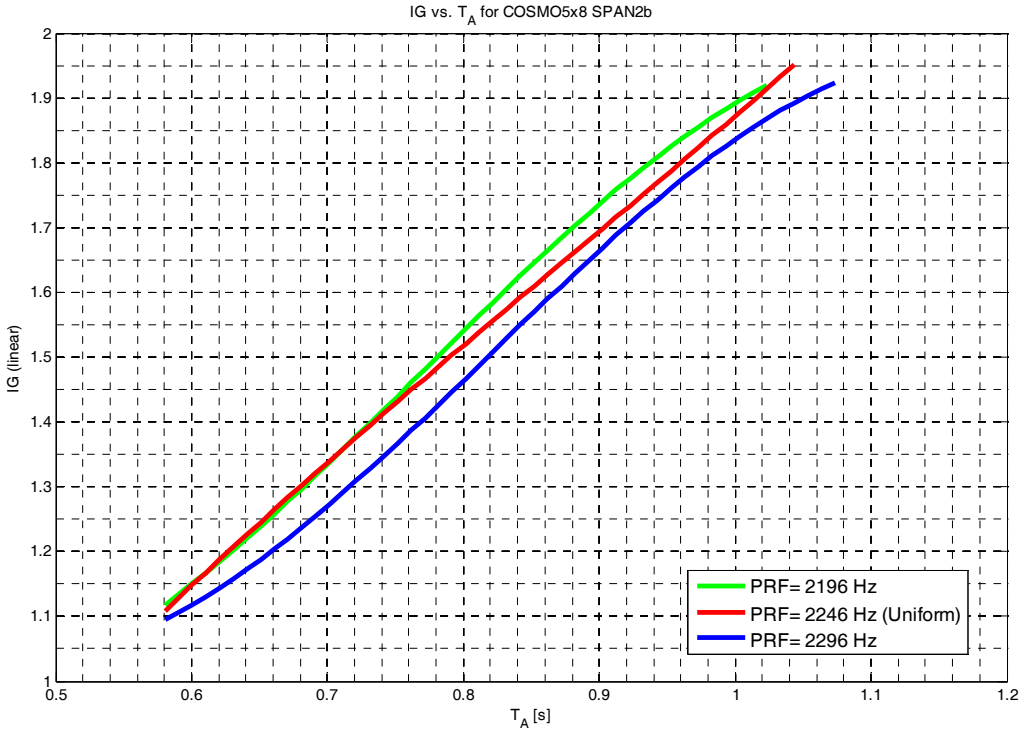

Figure II-11 Evaluation of the Information Gain for COSMO5x8 SPAN2b

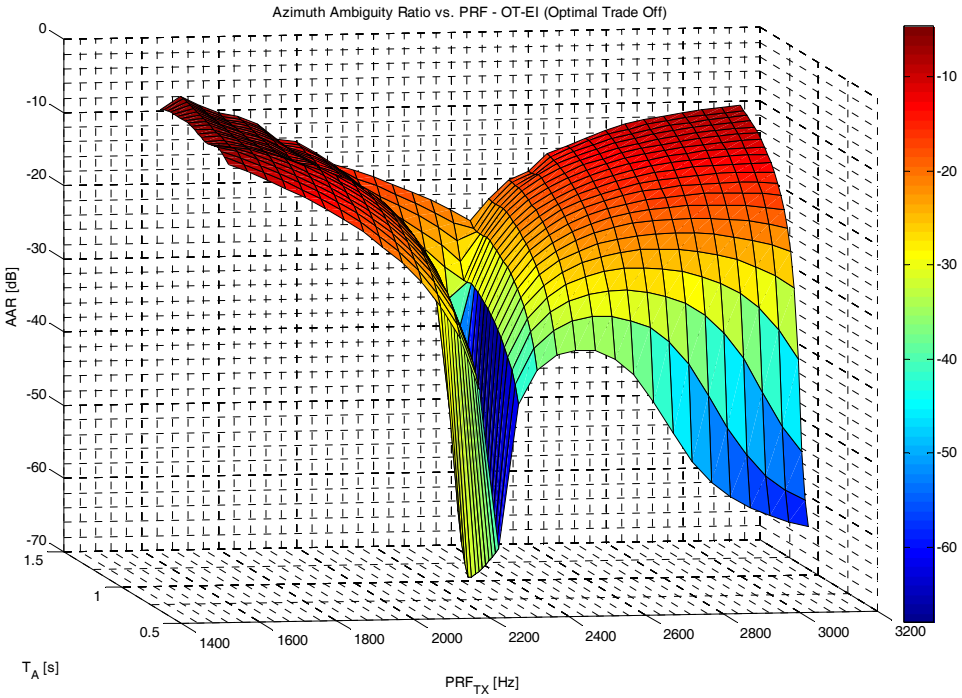

Figure II-12 AAR versus (T_A, PRF) for COSMO6x8 SPAN2c

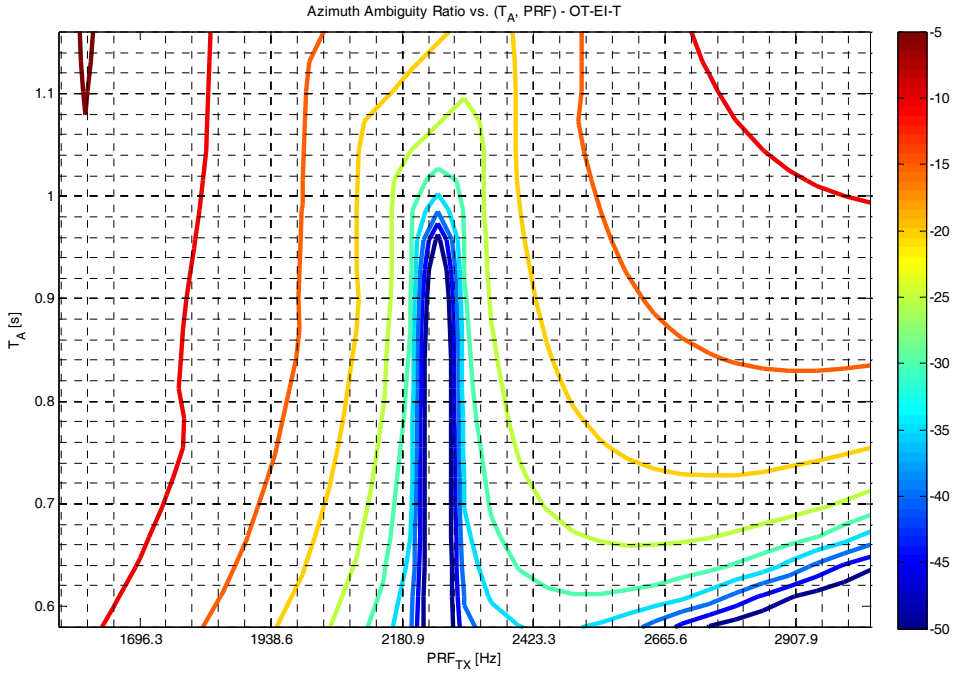

Figure II-13 AAR versus (T_A, PRF) for COSMO6x8 SPAN2c (contour plot)

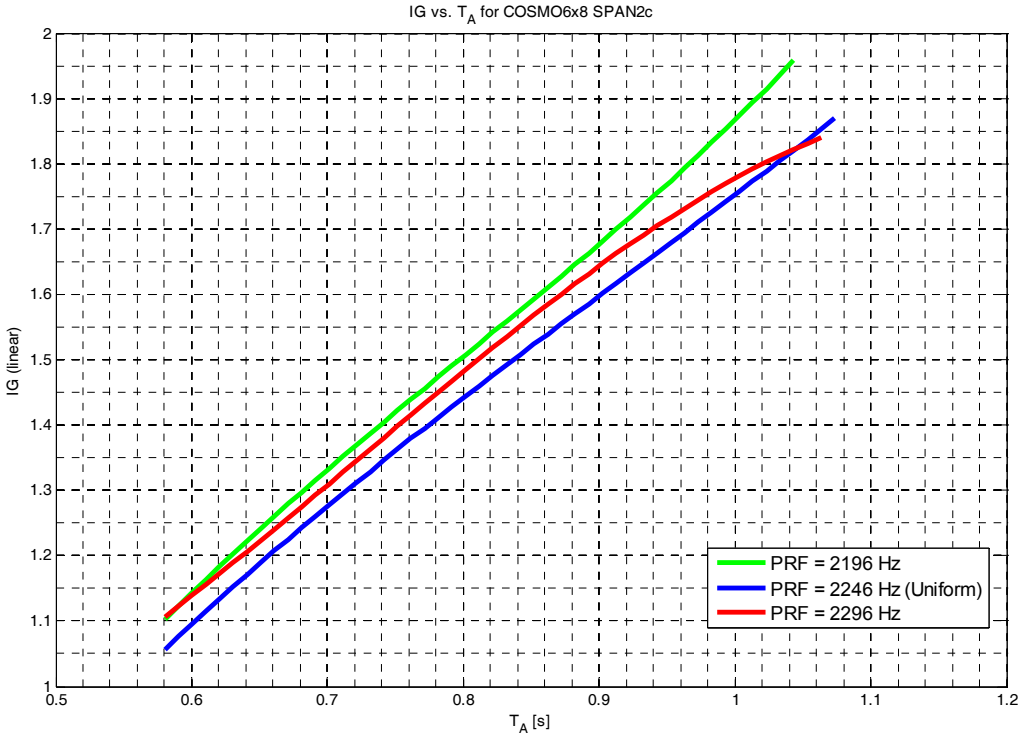

Figure II-14 Evaluation of the Information Gain for COSMO6x8 SPAN2c

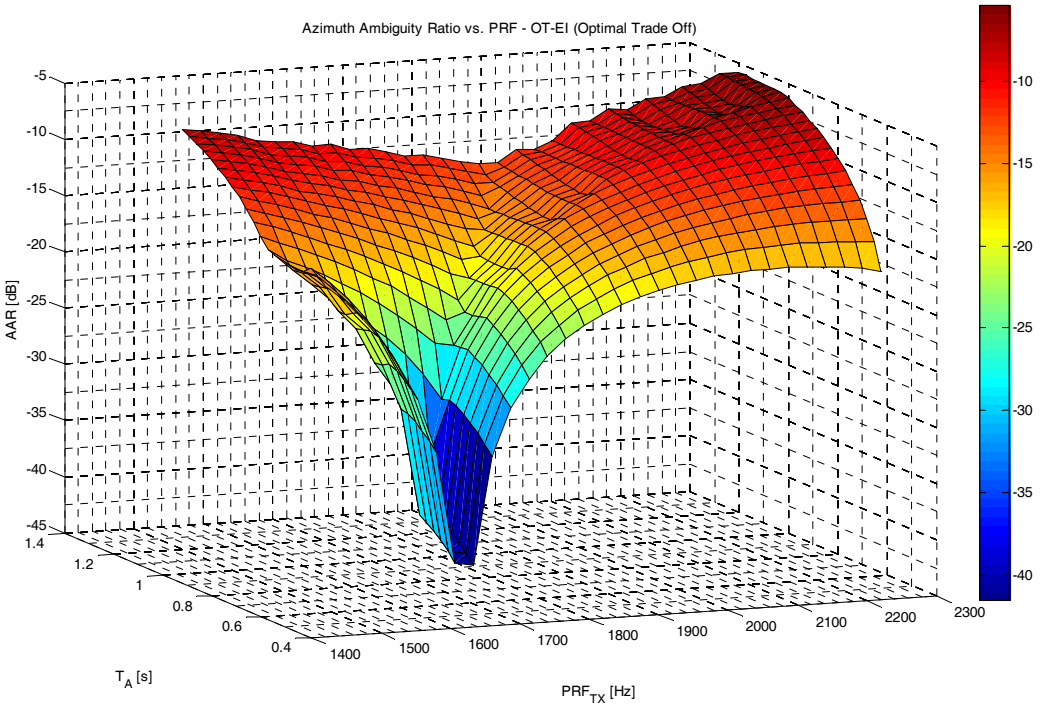

Figure II-15 AAR versus (T_A, PRF) for COSMO6x8 SPAN2b

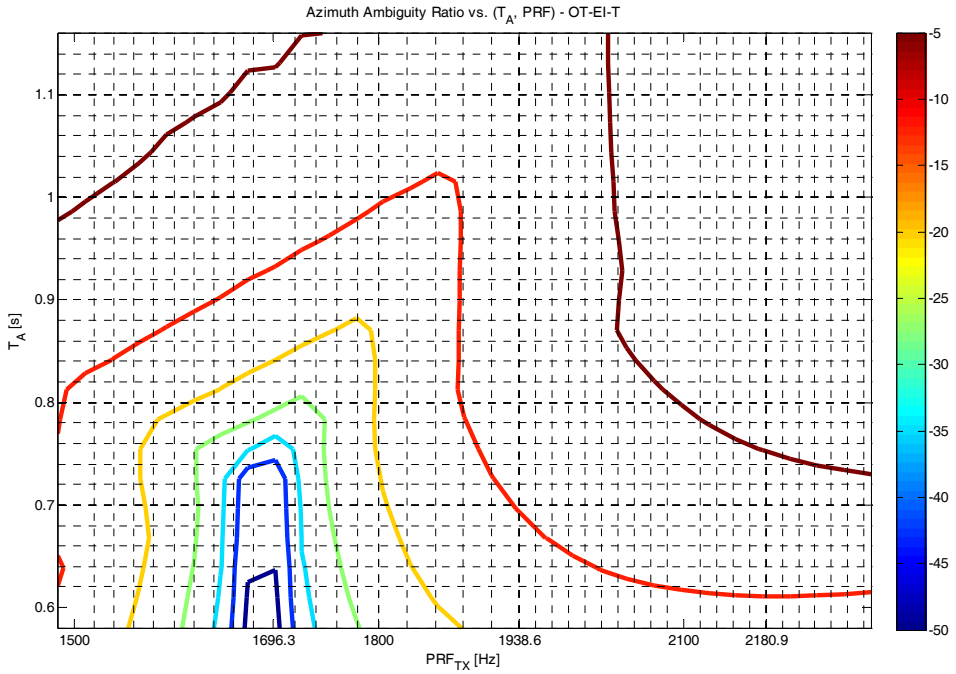

Figure II-16 AAR versus (T_A, PRF) for COSMO6x8 SPAN2b (contour plot)

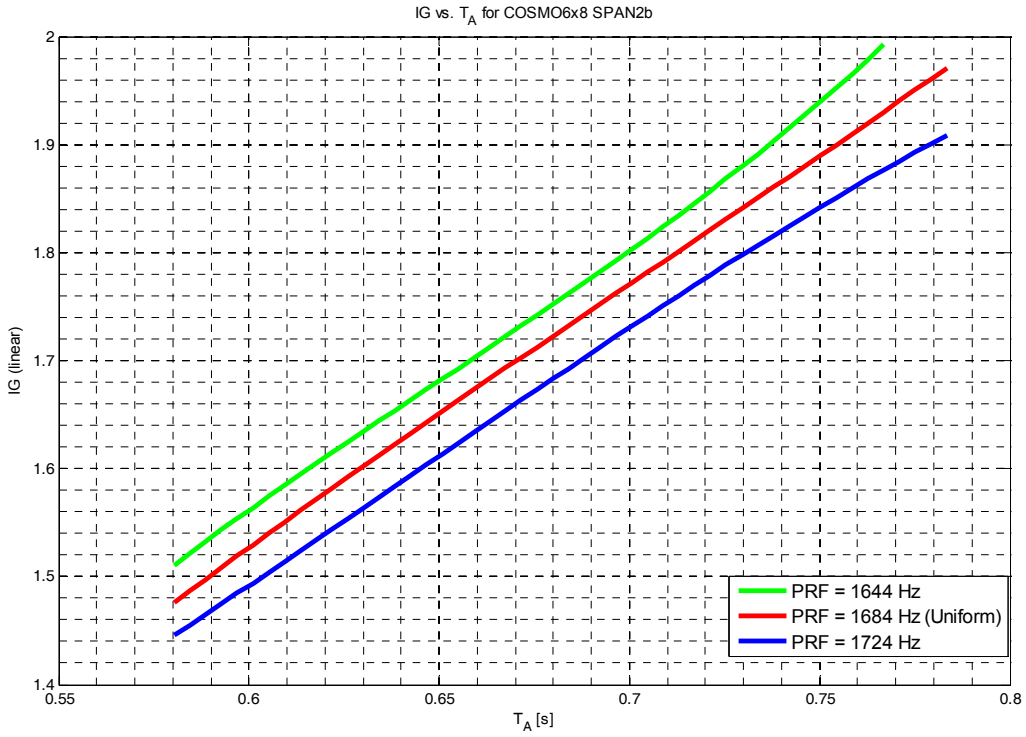

Figure II-17 Evaluation of the Information Gain for COSMO6x8 SPAN2b

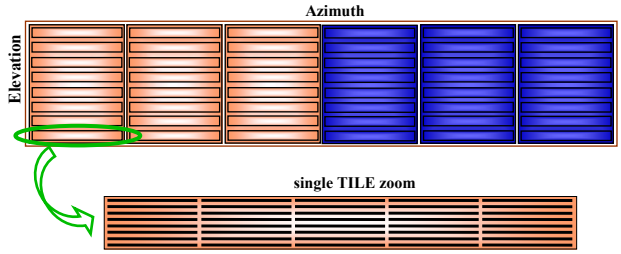

Figure II-18 Physical antenna structure (each black box indicates a T/R module)

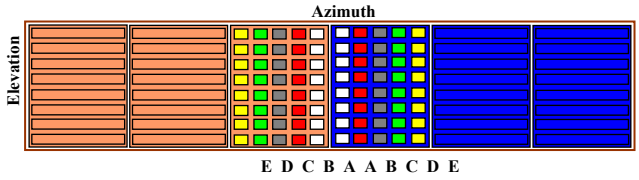

Figure II-19 Adaptive antenna configurations

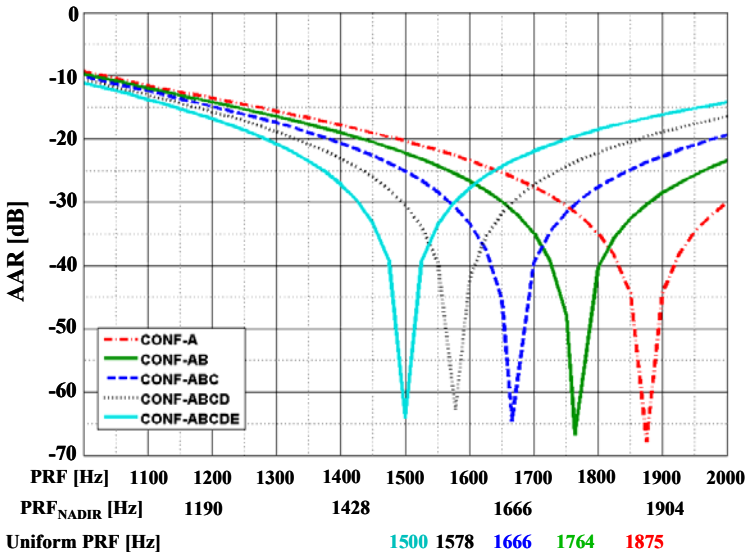

Figure II-20 AAR versus PRF for the five considered antenna configurations

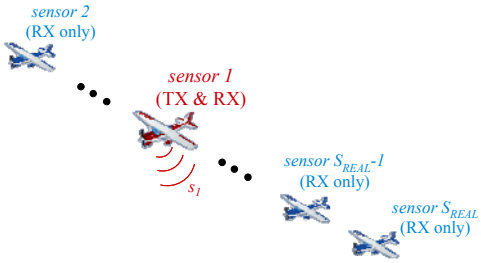

	Transmitted signals	Received signals
sensor 1	s_1	s_1
sensor 2	-	s_1
sensor 3	-	s_1
. . .	. . .	. . .
sensor S_{REAL}	-	s_1

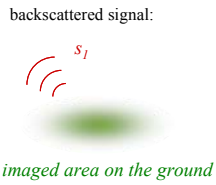

Figure II-21 Multistatic SAR: scheme of principle

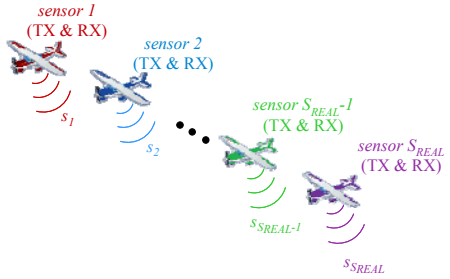

	Transmitted signals	Received signals
sensor 1	s_1	$s_1+s_2+s_3+\ldots+s_{S_{REAL}}$
sensor 2	s_2	$s_1+s_2+s_3+\ldots+s_{S_{REAL}}$
sensor 3	s_3	$s_1+s_2+s_3+\ldots+s_{S_{REAL}}$
. . .	. . .	. . .
sensor S_{REAL}	$s_{S_{REAL}}$	$s_1+s_2+s_3+\ldots+s_{S_{REAL}}$

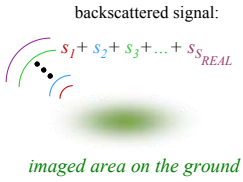

Figure II-22 MIMO SAR: scheme of principle

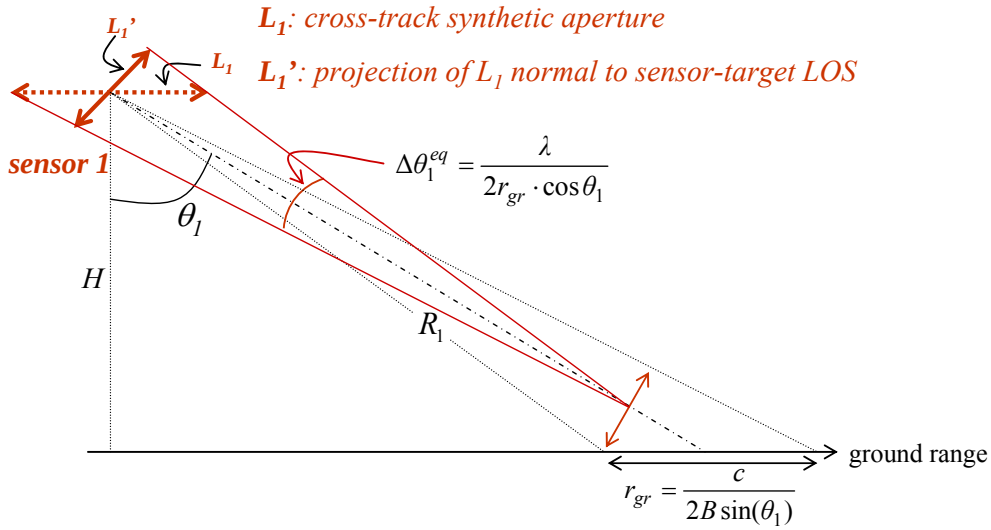

Figure II-23 Range resolution and equivalent aperture

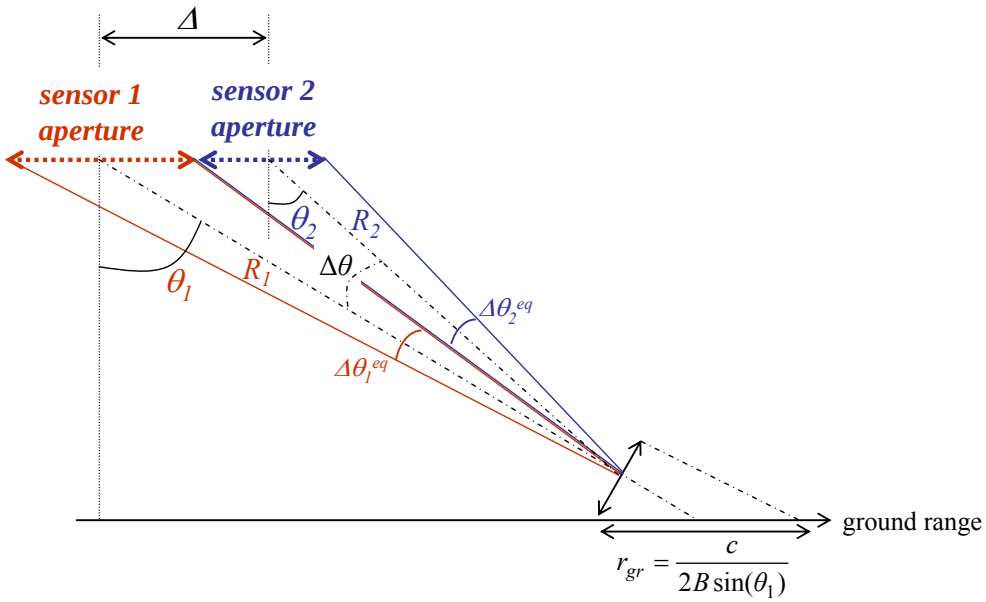

Figure II-24 Range resolution improvement with 2 SAR sensors

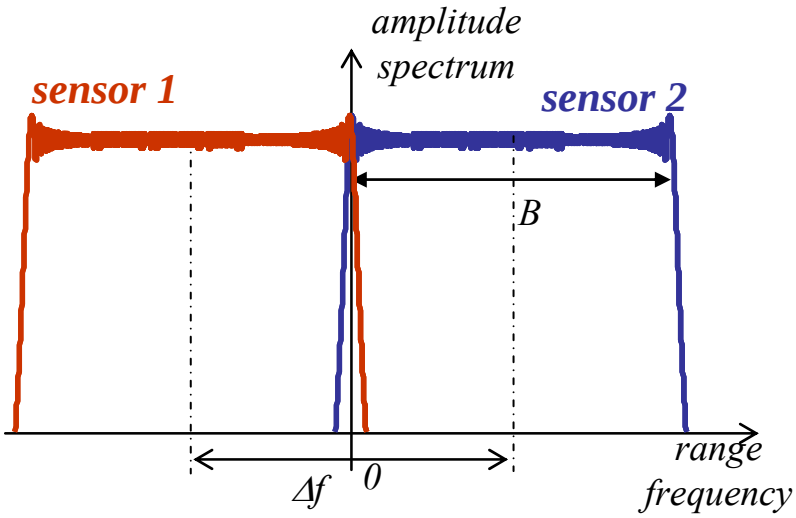

Figure II-25 Down-converted spectra

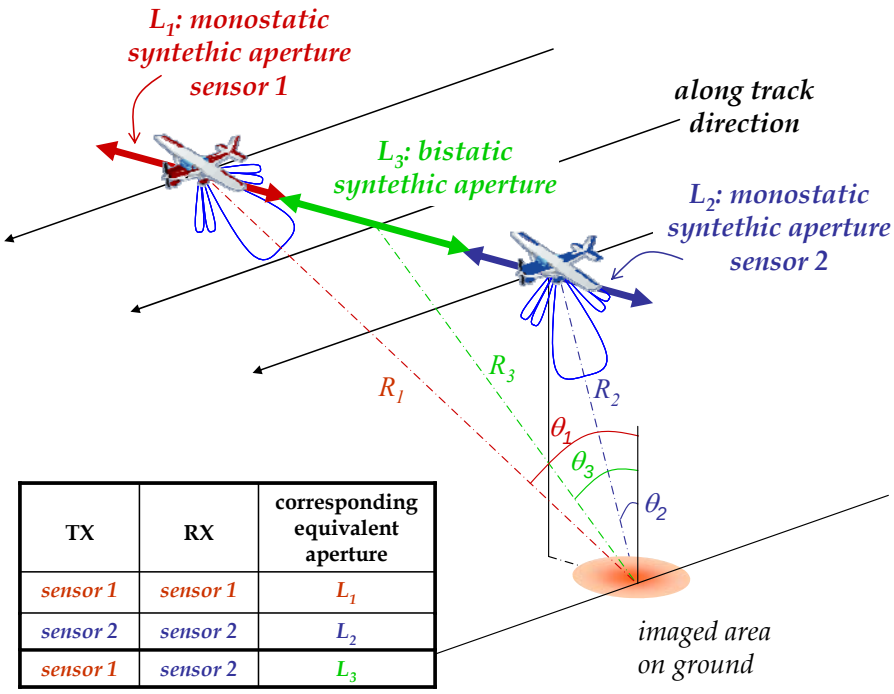

TX	RX	corresponding equivalent aperture
sensor 1	sensor 1	L_1
sensor 2	sensor 2	L_2
sensor 1	sensor 2	L_3

Figure II-26 MIMO acquisition geometry using 2 SAR sensors

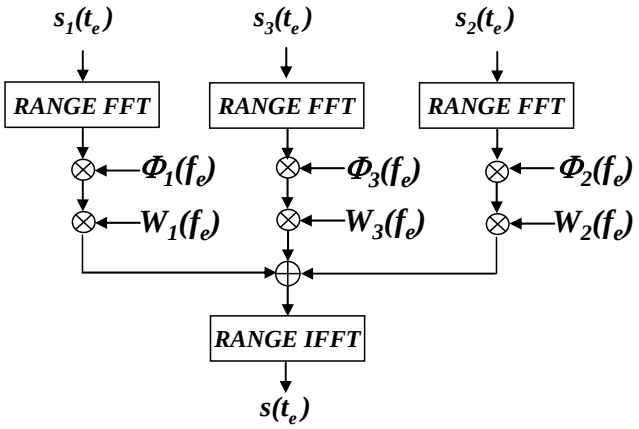

Figure II-27 MIMO scheme of principle

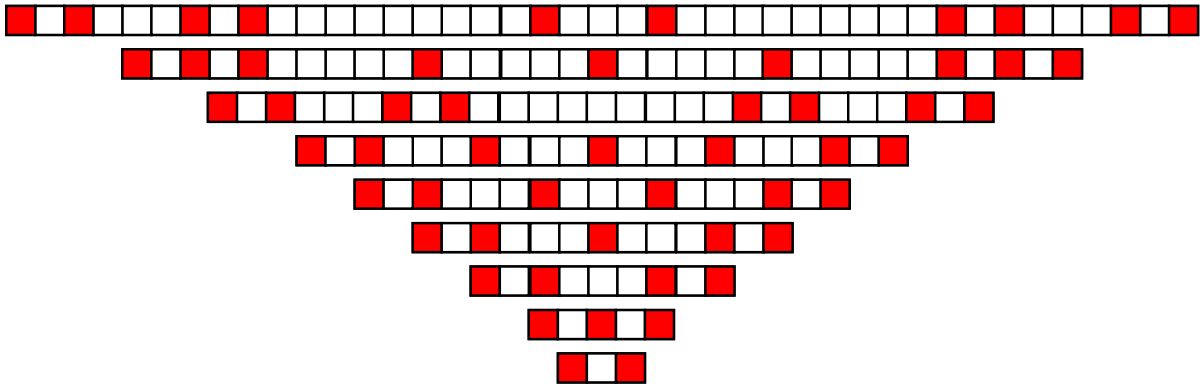

Figure II-28 Map of real and virtual apertures (angles of view) in the MIMO SAR

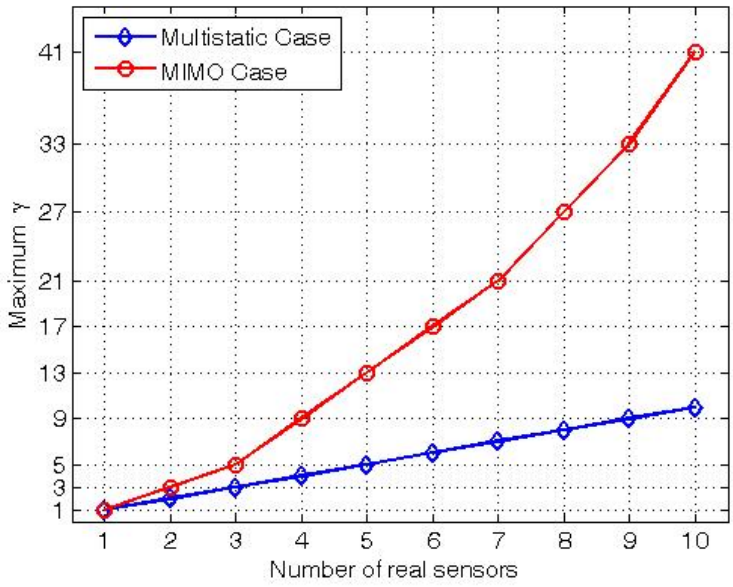

Figure II-29 Maximum range resolution improvement γ in the multistatic and MIMO cases

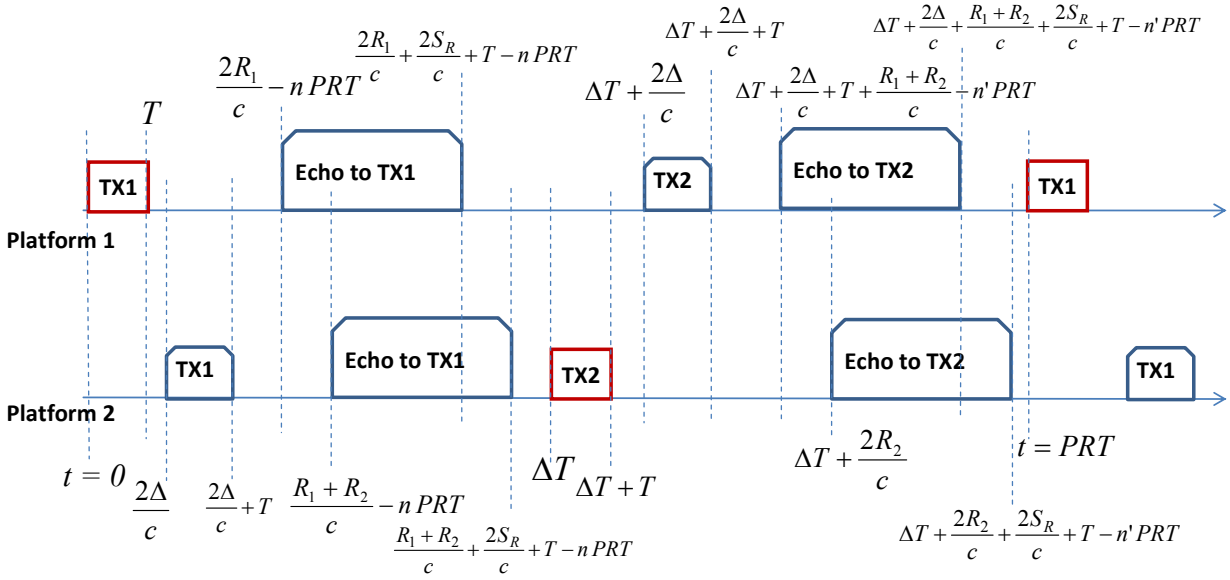

Figure II-30 Timing of the signals received by the two platforms

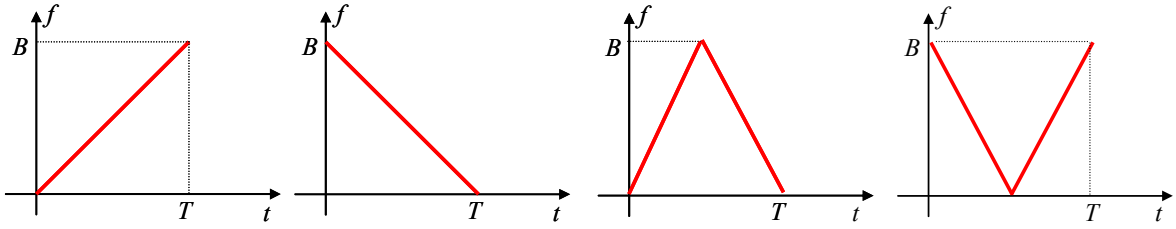

Figure II-31 Time-frequency representation of 4 different quasi-orthogonal waveforms suitable for a MIMO SAR

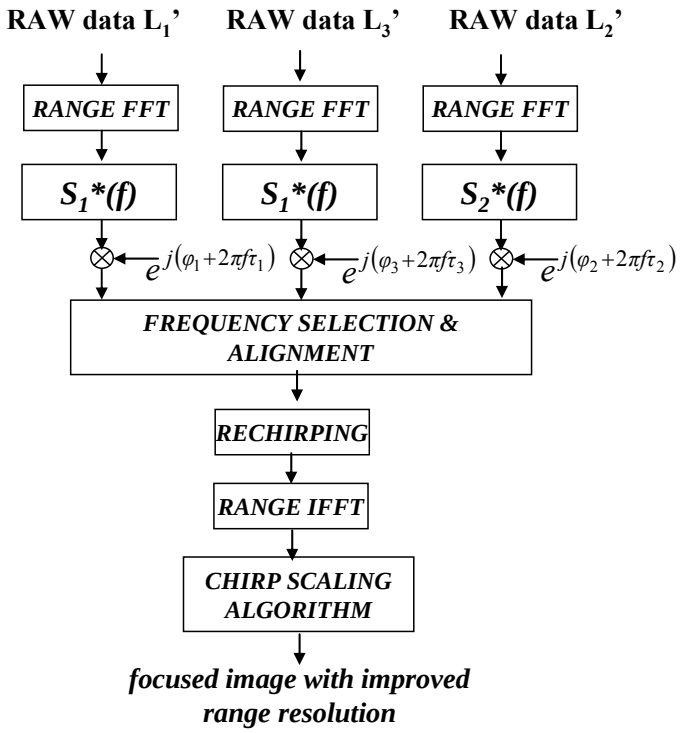

Figure II-32 MIMO processing: centralized technique

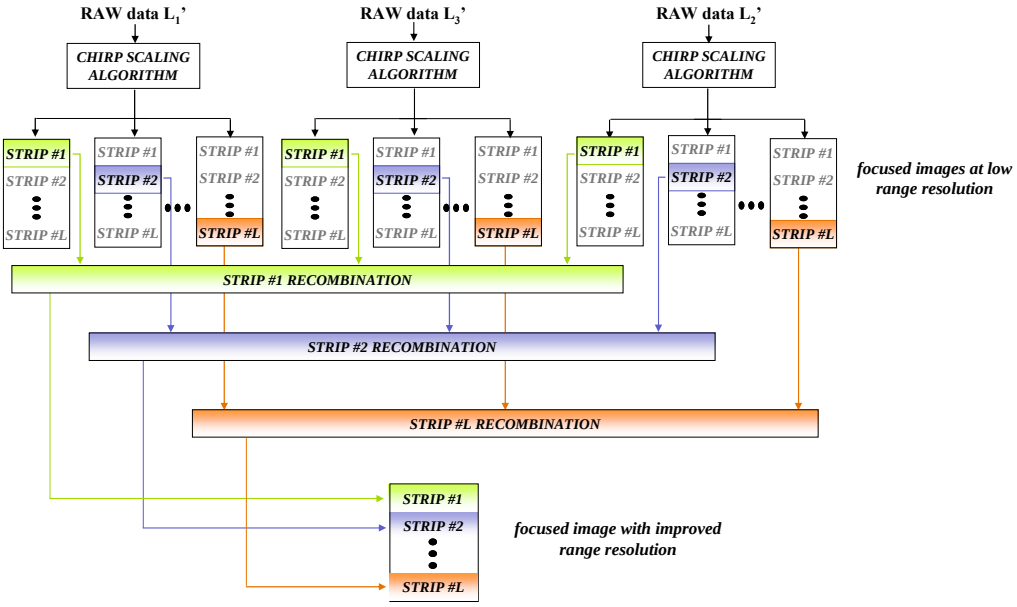

Figure II-33 MIMO processing: decentralized technique

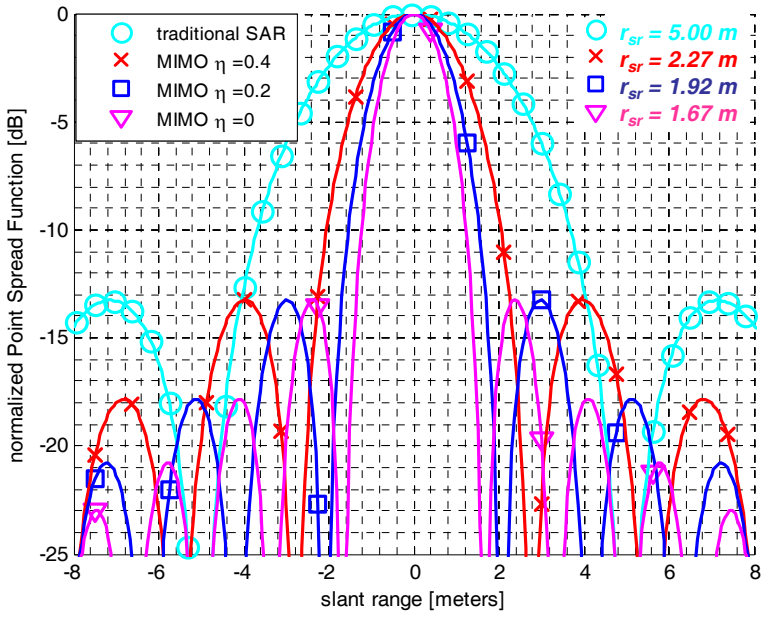

Figure II-34 MIMO PSF varying the spectral overlap η

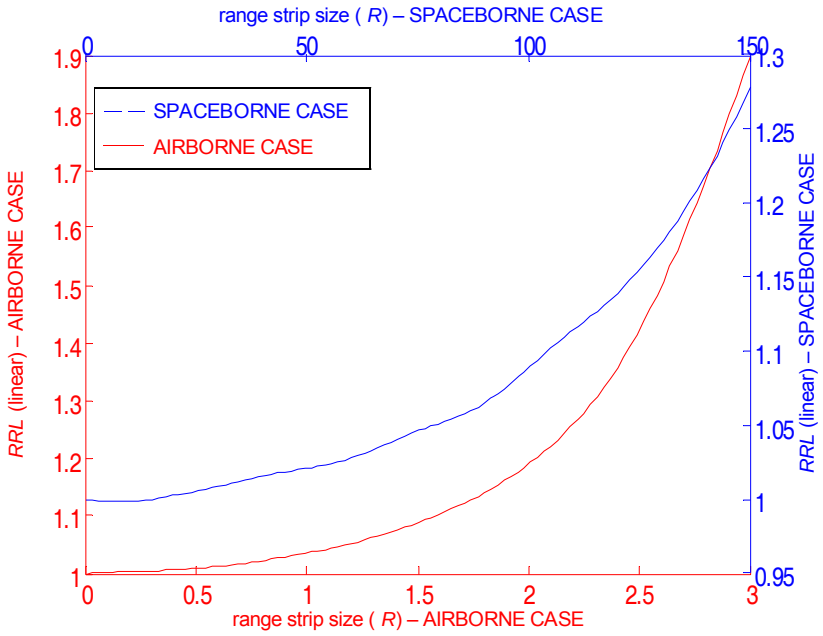

Figure II-35 Range Resolution Loss (*RRL*) versus range strip size (*R*)

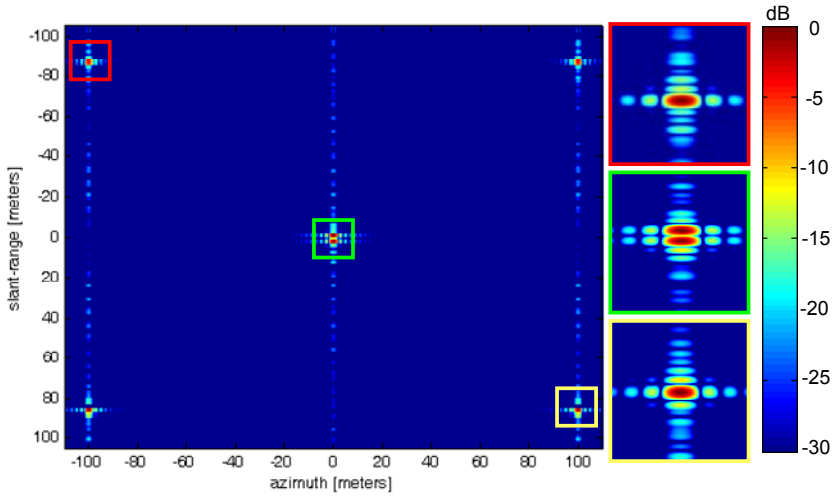

Figure II-36 Focused image with improved range resolution; airborne case, optimum decentralized technique

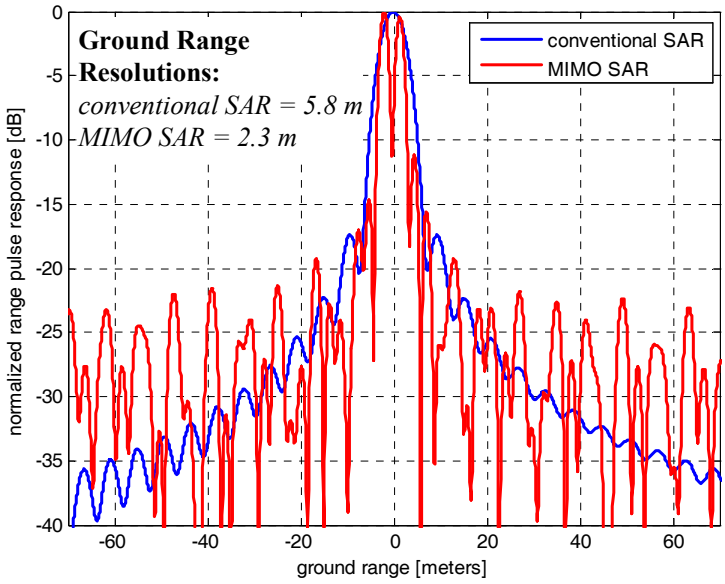

Figure II-37 Range section at azimuth = 0; airborne case, optimum decentralized technique

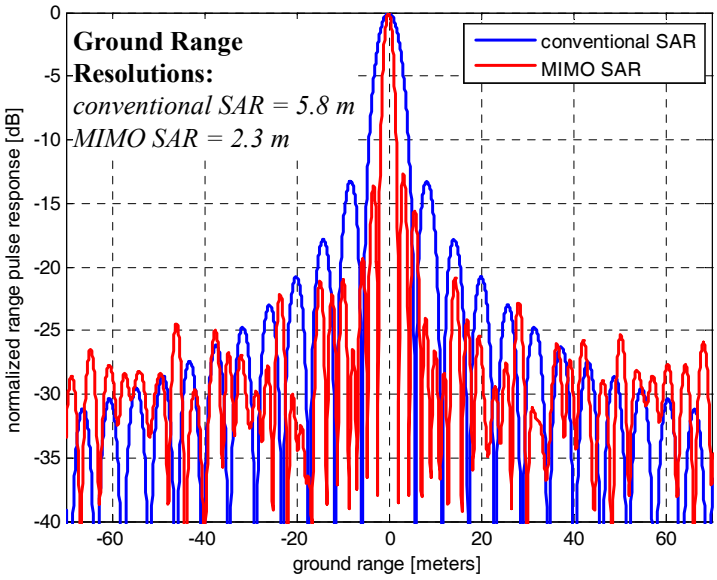

Figure II-38 Range section at azimuth = 100; airborne case, optimum decentralized technique

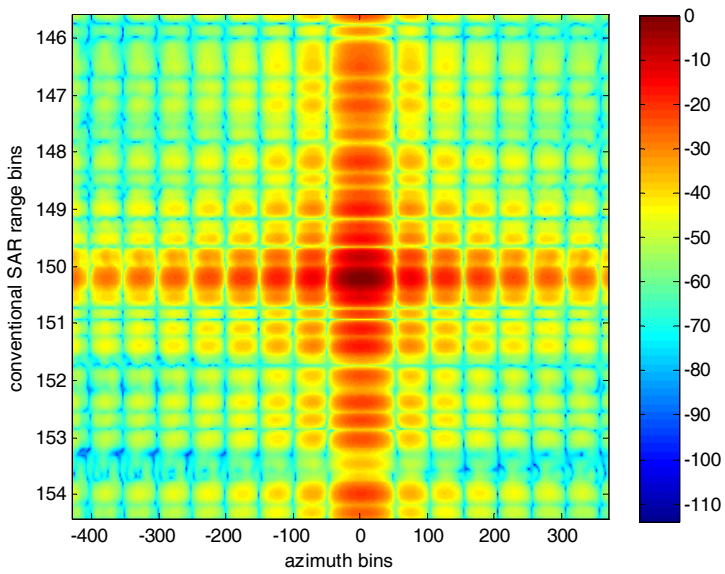

Figure II-39 Two dimensional pulse response for MIMO sub-optimal decentralized technique in the spaceborne worst case [dB]

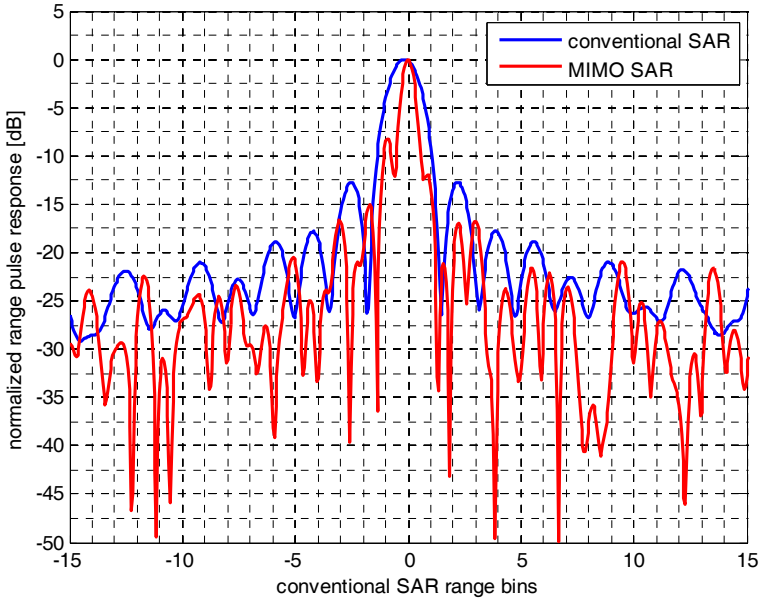

Figure II-40 Range pulse response for MIMO sub-optimal decentralized technique in the spaceborne worst case

II.5 *Tables*

Carrier frequency	9.6 GHz
Chirp Bandwidth	200 MHz
System Noise figure	7 dB
PRF Tx	1200 ÷ 2600 Hz (EI-S)[6] Uniform PRF (EI-R) 1400 ÷ 3000 Hz (EI-T)
Pointing direction	Right and Left looking
Incidence angle	37.78°
Integration time	0.67 s (EI-S) 0.58 ÷1.16 s (EI-R) 0.58 ÷1.16 s (EI-T)
Orbit height	619 km
Sensor velocity	7547 m/s
Power peak	5 KW
Pulse length	40 μsec

Tab. II-1 System parameters used for EI simulations

[6] Within this interval of PRF values, the $PRF = \frac{k \cdot c}{2 \cdot H}$, with k integer, will be highlighted in the following. These PRF values are important because they allow to avoid nadir returns.

Inter-element distance [cm]	2.33
Number of radiating elements	120
4 dB beamwidth [°]	0.78
Phase centers displacement [m]	3.36
RX-antenna gain loss [dB]	2

Tab. II-2 Single sub-aperture features for COSMO5x8 SPAN2b (azimuth only)

Inter-element distance [cm]	2.33
Number of radiating elements	144
3 dB beamwidth [°]	0.52
Phase centers displacement [m]	3.36
RX-antenna gain loss [dB]	0

Tab. II-3 Single sub-aperture features for COSMO6x8 SPAN2c (azimuth only)

Inter-element distance [cm]	2.33
Number of radiating elements	96
3 dB beamwidth [°]	0.78
Phase centers displacement [m]	4.48
RX-antenna gain loss [dB]	3.5

Tab. II-4 Single sub-aperture features for COSMO6x8 SPAN2b (azimuth only)

	Azimuth resolution [m]
COSMO6x8 SPAN2c	1.84
COSMO5x8 SPAN2b	1.60
COSMO6x8 SPAN2b	2.25

Tab. II-5 Achievable azimuth resolutions with AAR<-25 dB

	EI-S	EI-R	EI-T
AAR [dB]	-25 dB	-25 dB	-25 dB

Tab. II-6 AAR constraint for the three EI

	EI-S	EI-R	EI-T
NESZ [dB]	6÷8 dB	0÷2 dB	0 ÷ 8 dB

Tab. II-7 NESZ loss for the three EI

	Swath Improvement
COSMO5x8 SPAN2b	1.65
COSMO6x8 SPAN2c	1.65
COSMO6x8 SPAN2b	2.20

Tab. II-8 Swath Improvement in EI-S for the considered antenna configurations

	Resolution Improvement
COSMO5x8 SPAN2b	1.75
COSMO6x8 SPAN2c	1.52
COSMO6x8 SPAN2b	1.24

Tab. II-9 Resolution Improvement in EI-R for the considered antenna configurations

	Information Gain
COSMO5x8 SPAN2b	1.9
COSMO6x8 SPAN2c	1.9
COSMO6x8 SPAN2b	1.95

Tab. II-10 Information Gain in EI-T for the considered antenna configurations

Carrier Frequency [GHz]	9.5
Number of Radiating Elements (Azimuth)	300
Number of Radiating Elements (Elevation)	64
Azimuth Length [m]	7.50
Elevation Length [m]	1.28
Azimuth Beamwidth [°]	0.24
Elevation Beamwidth [°]	1.41
Phase Centers Displacement [m]	3.75
Maximum Sub-Aperture Gain [dB]	39.82

Tab. II-11 Main Antenna Parameters

	A	AB	ABC	ABCD	ABCDE
Phase Centers Displacement [m]	4.00	4.25	4.50	4.75	5.00
Maximum Sub-Aperture Gain [dB]	39.52	39.20	38.85	38.47	38.06
Azimuth Sub-Aperture Beamwidth [°]	0.52	0.56	0.60	0.66	0.72
Elevation Sub-Aperture Beamwidth [°]	1.41	1.41	1.41	1.41	1.41

Tab. II-12 Main Antenna Configurations Characteristics

Carrier Frequency [GHz]	9.5
PRF on Transmit [Hz]	1000 ÷ 2000
Incidence Angle [°]	37.78
Orbit Height [km]	630
Sensor Velocity [m/s]	7500

Tab. II-13 Main System Parameters

	A	AB	ABC	ABCD	ABCDE
AAR [dB]	-67.8	-66.8	-64.7	-62.8	-64.0
Azimuth Resolution [m]	3.49	3.22	2.98	2.79	2.65
Uniform PRF [Hz]	1875	1764	1666	1578	1500
Azimuth Resolution Improvement [%]	7.21	16.4	25.8	34.1	41.2
Range Swath Dimension Improvement [%]	6.70	13.4	20.0	26.6	33.3

Tab. II-14 Simulation Results

N	S	Bound: N (N+1)/2	Sequence of angular spacings	S/N	1-S/Bound
2	3	3	2	1.5	0,000
3	5	6	2,2	1.6667	0,167
4	9	10	2,4,2	2.2500	0,100
5	13	15	2,4,4,2	2.6000	0,133
6	17	21	2,4,4,4,2	2.8333	0,190
7	21	28	2,4,4,4,4,2 2,2,6,6,2,2	3.0000	0,250
8	27	36	2,2,6,6,6,2,2 2,4,2,10,2,4,2	3.3750	0,250
9	33	45	2,2,6,6,6,6,2,2	3.6667	0,267
10	41	55	2,4,2,10,4,10,2,4,2	4.1000	0,255
11	45	66	2,2,2,8,8,8,8,2,2,2 2,2,6,4,8,8,4,6,2,2 2,2,6,6,6,6,6,6,2,2 2,4,2,10,4,4,10,2,4,2	4.0909	0,318
12	55	78	2,4,4,2,14,2,14,2,4,4,2 2,4,2,10,4,10,4,10,2,4,2	4.5833	0,295
13	65	91	2,4,2,10,4,10,10,4,10,2,4,2	5.0000	0,286
14	73	105	2,4,2,10,4,10,8,10,4,10,2,4,2	5.2143	0,305

Tab. II-15 Optimized MIMO configurations

carrier frequency	9.6 GHz
sensor height	6500 m
platform velocity	120 m/s
transmitted chirp bandwidth	30 MHz
θ_0 (mean incident angle)	60°
Conventional SAR slant range resolution	5 m

Tab. II-16 Main system parameters

III MULTI-CHANNEL SAR FOR JAMMER REJECTION

III.1 *Introduction*

The imaging capability of a Synthetic Aperture Radar (SAR) could be seriously limited or denied by an electromagnetic interference signal impinging on the antenna array during the synthetic aperture. Such interference could be both intentional (i.e. Jamming) or due to a spurious transmission in the same frequency band in which the SAR operates (i.e. RFI, Radio Frequency Interference). Moreover, the SAR pulse transmitted power is penalized by 2-way propagation losses, while interference power has only 1-way propagation losses. Thus, even if the interference transmitted power is not high and it is received by the side-lobes of the SAR antenna, the SAR imaging capabilities can be denied. For imaging radars, the effect of a wideband noise-like interference is to mask the scene visible in the imaged area with a high uniform noise level [4], [30].

It is well known that the protection of a multi-channel radar from high duty cycle e.m. interferences can be achieved on the basis of antenna nulling. This is usually obtained by adaptively combining the signals received by multiple auxiliary channels, together with the main channel, in order to synthesize an equivalent pattern with a null (or at least a strong depression) in the Direction Of Arrival (DOA) of the interfering signal.

If the SAR is required to perform surveillance on a wide area, and the jamming source location is not known by the radar, there is no restriction on the possible DOA of the jammer both in azimuth and in elevation. To give a coarse estimation of the range of possible DOAs, we refer to a spaceborne scenario

where a SAR is mounted on a Low Earth Orbit (LEO) platform at an height above the Earth surface (H) of about 500 km, as shown in **Figure III-1**. Indicating with R_e the Earth radius, the maximum angle of arrival for the interference signal (α), both in azimuth and in elevation, can be simply obtained as:

$$\alpha = \sin^{-1}\left(\frac{R_e}{R_e + H}\right) \cong 68° \qquad \text{Eq. III-1}$$

The SAR operational scenario, characterized by a relative motion between the sensor and the jammer, determines the interference DOA to vary during the acquisition. This has two main impacts on the antenna nulling technique to be implemented. First of all, the antenna nulling has to adaptively counteract to the time-varying jammer DOA, thus achieving the required interference power attenuation for each slow-time instant of the acquisition. In addition, the slow-time variation of the synthesized pattern has not to affect the SAR pulse response, thus also allowing to achieve an adequate image quality level.

In the definition of an antenna-based ECCM two major key points arise: the weights update frequency and the weights selection strategy. It is clear that a low updating frequency determines the need to synthesize an adapted pattern with a wide angular depression to include the jammer DOA variation between subsequent updates. On the other hand, a higher update frequency results in a reduced jammer DOA variation allowing to synthesize a deeper depression in the adapted pattern. From a performance point of view the updating frequency has an impact on the computational burden for the weights evaluation, but also on the quality of the resulting SAR image, since a narrower depression in the adapted pattern is expected to less affect the pulse response when the jammer DOA comes close to the SAR antenna steering direction. The two borderline cases are represented by a pulse-to-pulse update and by the use of a fixed adapted pattern for the whole acquisition time.

Regarding the weight selection strategy, the following possibilities arise:

a) weight determination exclusively on the basis of an a priori knowledge of the jammer DOA (with a given level of accuracy σ);

b) weight determination from a jammer DOA estimation made on the data received by the sensor;

c) weight determination from an interference covariance matrix estimation made on data received from auxiliary beams (full adaptivity);

d) weight determination from the joint use of a priori jammer DOA knowledge and of interference covariance matrix estimation (partial adaptivity);

e) weight determination from the joint use of jammer DOA estimation from received data and of interference covariance matrix estimation (partial adaptivity).

Assuming the main SAR antenna to be constituted by a phased array in which it is possible to control (phase and amplitude) each group of elements (i.e. T/R module), the previous strategies pose the following constraints on the receiving channels:

a) no auxiliary antenna beams are needed, thus a single channel can be used. Attenuators and phase shifters controlling the T/R modules have to be modified to synthesize a received pattern with a strong depression in the jammer DOA;

b) at least three parallel receiving channels are required for the jammer DOA estimation. Once the jammer DOA has been estimated, a single channel SAR acquisition can be performed, using the attenuators and phase shifters to synthesize the adapted pattern. If more than one jammer is present, the actual number of interfering sources has to be estimated;

c,d) the number of required parallel receiving channels (number of Degrees Of Freedom, DOF) is given by the number of jammers plus one. The weight determination is performed without a jammer DOA estimation;

e) a complex antenna structure is required to take into account the needs of c) and b). It has to be noticed that an adequate choice of the auxiliary beams for the jammer DOA estimation might not be a proper choice for the jammer cancellation.

III.2 *Scenario Definition*

In this paper two different SAR operational scenarios will be presented to describe the different ECCM techniques: a spaceborne (Low Earth Orbit) and an airborne scenario (main system and phased antenna parameters are reported in **Tab. III-1** and **Tab. III-2**, respectively). It is worth noticing that phased array antennas are here considered both for the airborne and for the spaceborne case, with a parallel independent receiving channel connected to each antenna element. Even if this is not a realistic case, especially for a spaceborne system, it is interesting to investigate this case since it constitues a best case situation with the maximum allowable number of DOFs, for a given phisical antenna structure.

For each of these SAR scenarios, two different interference configurations are considered, namely a Low-Tech (LT) and a High-Tech (HT) scenarios characterized by two different values of Equivalent Isotropically Radiated Power (EIRP), depending on the jammer's available technologies. We consider a ground based barrage jammer located within the SAR access area both for the spaceborne and for the airborne scenario, as shown in **Tab. III-3**. The ECCM techniques will be considered applied at element level (namely one DOF for each phased array antenna element), thus leading to an optimal antenna nulling configuration. Moreover, all the analysis will be conducted with reference to the scenario where useful radar signal and interference band are matched and the noise-like interference is always present during SAR acquisition. Finally, the jamming source is considered narrowband, which is a reasonable hypothesis for medium/high resolution SAR at X-band. The effects of wide-band noise-like interference has been considered in past literature [41]; a work of the author, [42], has dealt with the imaging effect on SAR range pulse response due to wideband antenna nulling and its integration with focusing algorithms.

III.3 *ECCM with a priori knowledge of the jammer DOA*

We first refer to the simple case where the jammer DOA is known, so that an optimal set of complex weights can be calculated and applied in reception to each single radiating element to cancel the interfering signal. The *a priori* knowledge of the jammer DOA allows to implement an antenna nulling scheme even working with a single channel SAR system. If the available DOA estimation is correct (i.e. no estimation errors are experienced) this yields to optimal cancellation performance. To describe this reference situation, several performance parameters will be considered.

III.3.1 Single pulse jammer cancellation

First of all the cancellation capabilities will be shown in terms of Signal to Interference plus Noise Ratio (SINR) achievable on the single slow-time instant varying the jammer's DOA in the azimuth/elevation plane. In a second case a grid of point-like targets is considered within the SAR access area. For each position of the grid the SINR is evaluated after signal focusing together with the SAR pulse response quality parameters (i.e. resolution and SideLobe Ratio, SLR). Finally a simulated SAR image is computed adding to the useful point-like signal returns both thermal noise and jammer samples; the ECCM noise-masking removal will be shown with comparison to the no-ECCM case.

SINR versus jammer DOA

To show the effectiveness of the jammer cancellation using all the possible Degrees Of Freedom (DOF) we first consider the achievable Signal to Interference plus Noise Ratio (SINR) on the single slow-time instant. In particular, SINR is evaluated fixing the antenna steering in a broadside direction, which is also the useful signal DOA, and varying the jammer DOA in the azimuth/elevation plane. It is

worth to notice that no evaluation on the slow-time variation of the cancellation capability is conducted in this analysis, hence the impact on the SAR imaging capability cannot be observed here. Results are shown in **Figure III-2** and **Figure III-3** for the spaceborne-LT and spaceborne-HT scenarios, respectively. As apparent, the high number of DOFs allows to achieve top performance[7] for all the possible DOAs out of the antenna main-beam. **Figure III-4** and **Figure III-5** show similar performance for the airborne-LT and airborne-HT scenarios, respectively. The widths of SINR degradations in azimuth/elevation directions correspond to the antenna beamwidths in azimuth/elevation, respectively. This simply means that the system is not able to reject jammer impinging on the antenna main beam.

[7] For the single-pulse SINR, top cancellation performance corresponds to the maximum receiving antenna gain since a normalization on the thermal noise has been considered for simplicity. When the SINR is evaluated after SAR focusing (see paragraph III.4.1), top cancellation performance are represented by the corresponding SNR achievable when no-jammer is present, since, in this second case, a link budget is considered.

III.4 *Pulse-to-pulse nulling weights update*

The following analysis included in this paragraph, takes into account a pulse-to-pulse antenna nulling weights update. In fact, due to the platform motion during acquisition, the jammer DOA changes every Pulse Repetition Time (PRT). Theoretically, this requires the nulling weights to be updated every PRT. Obviously, at the expense of a cancellation performance degradation, it is possible to reduce the update frequency maintaining the same set of nulling weights for several subsequent PRTs. This can be an interesting approach to reduce the computational burden for nulling weights calculation, or it can be a compelled solution if the jammer DOA information is not available every PRT. We first consider the optimal case of a pulse-to-pulse update strategy, investigating sub-optimal solutions later on in this work.

III.4.1 Map of SINR after SAR focusing over a grid of scatterers

In this section we aim to determine the vulnerability of a SAR sensor to a noise-like interference signal transmitted from the ground. The vulnerability measure of a SAR is defined as the imaged area on the ground where the achievable SINR after focusing is too low to ensure a proper SAR operability. In [4] two different SINR thresholds are defined to quantify the proper operability of a radar working in a jamming environment. The first threshold (SINR<10 dB) defines the SINR values that do not allow to acquire a new target, while the second threshold (SINR<3 dB) defines the SINR values that do not even allow to confirm the presence of an already acquired target. The scope of our analysis is to evaluate, over the SAR access area, the regions where the SINR after focusing is below these thresholds, considering a SAR working in stripmap acquisition mode. The SAR operability improvement due to ECCM can be measured by means of reduced dimension of the area where information acquisition is

denied. The interference scenario considered for this analysis is sketched in **Figure III-6** for the spaceborne case, where the red mark symbolizes ground interference source, green and red arrows indicate 2-way and 1-way propagation paths of radar and interference signals, respectively.

Figure III-7 shows the SNR (Signal to Noise Ratio) obtained when no interference is present during imaging. In this case, the SNR degrades for increasing incident angles due to increasing SAR-terget distance (i.e. increasing propagation losses). The achievable Signal to Interference plus Noise Ratio behaviour is quite different when a single interfering jammer is present within the SAR access area. In this case, the maximum achievable SINR degrades significantly in the sorroundings of the jammer location (namely azimuth = 0 km, incident angle = 40°) if no ECCM is applied. This situation is depicted in **Figure III-8** and **Figure III-9**, for the spaceborne LT and HT scenarios, respectively. As apparent, the masking effect is more significant for an HT jamming environment. To give a measure of the area where the SAR imaging capability is denied, the 10 dB and 3 dB thresholds proposed in [4] can be applied to these SINR maps. This will give a coarse estimation of the dimension of the regions within the SAR access area where SAR imaging capabilities are affected. By applying these two threshols to SINR maps in **Figure III-8** and **Figure III-9**, the maps of denied areas depicted in **Figure III-10** and **Figure III-11** can be obtained. In particular, areas that have a SINR less than 10 dB are yellow colored indicating that new target acquisition capability is denied. Red colored areas have SINR less than 3 dB; in these regions even confirmation of an already acquired target is denied. Results show how a jammer located inside the access area can limit the image capability of a spaceborne SAR for most of the range access area and for a long azimuth area. To overcome this limitations, an antenna based ECCM technique can be applied, thus leading to the maps of SINR reported in **Figure III-12** and **Figure III-13**. Moreover, in **Figure III-14** and in **Figure III-15** the two thresholds have been applied to these maps. The reduction of the red and yellow areas due to ECCM application is evident. As

already mentioned in the previous paragraph, the huge number of DOFs yields to top performance all over the grid except for the point where the jammer is located. The effect of a limited number of DOFs (or, equivalently, of few directive auxiliary patterns to counteract the presence of the jammer) has been deeply analysed in [31], whereas in [32], [33], and [34] a reduced order jammer cancellation scheme is proposed to keep limited the number of adaptive DOFs required to synthesize nulls in the antenna pattern.

Moreover, in addition to the cancellation performance analysis, it is interesting to evaluate the impact on the SAR pulse response. The scope of our analysis is to evaluate the potential amplitude modulation on the SAR data envelope in the azimuth domain due to the pulse-to-pulse antenna nulling. To this end, maps of achievable azimuth imaging performance (namely resolution and SLR) have been derived for the same aforementioned case studies. **Figure III-16**-**Figure III-17** and **Figure III-18**-**Figure III-19** show the measured azimuth resolution and azimuth SLR for the spaceborne-LT and for the spaceborne-HT scenarios, respectively. As apparent, the measured pulse response performance parameters are slightly different from their theoretical counterparts. This effect is intrinsic to real SAR systems operating in stripmap mode, since it is due to the antenna gain variation during the synthetic aperture. The azimuth pulse response degradations due to pulse-to-pulse antenna nulling, both in terms of resolution and SLR, are experienced only for target positions close to the jammer source. However, this does not constitute a further performance degradation over the SAR access area, since these positions correspond to yellow/red areas on the maps of denied areas (see **Figure III-14** and in **Figure III-15** for comparison).

III.4.2 Simulated SAR image with jammer

In this section a third analysis is presented to show the effectiveness of ECCM techniques for a SAR system working in a jamming environment. In this case a simulated focused image is presented

containing three point-like targets. Jammer and thermal noise samples are injected on the received raw signals to simulate the presence of an interference located close to the imaged area. Acquisition geometry is sketched in **Figure III-20** for the airborne-LT case. The image scene dimension is 200 m × 200 m (along track × ground range), and the three targets are placed in top-left, central, and bottom-right positions. The jammer is displaced in along track on the scene center range bin, impinging on the first azimuth sidelobe of the antenna during SAR acquisition. Main system parameters are reported in **Tab. III-4**. In **Figure III-21** is reported the obtained focused image adding to the useful received data only thermal noise samples, not applying any antenna nulling technique to counteract the interference. The image (reported in dB) has been normalized to the targets peak value, to highlight the achieved SNR. For each target, a zoom is reported on the right-end side of the image. The SNR is measured averaging the noise floor (i.e. averaging the focused image where no useful signal contributions are present). Given that no jammer samples have been added to this image, the SNR achieved in this case represents the maximum achievable SINR in presence of noise and jammer samples applying an ECCM technique. In **Figure III-22** is reported a similar focused image adding to the useful target returns both thermal noise and jammer samples. As apparent, the SINR level is degraded not making visible any of the three point-like targets. In **Figure III-23** the same simulated SAR image has been focused again, applying the pulse-to-pulse antenna nulling. The three point-like targets are again visible, and the achievable SINR is almost equal to the SNR measured in **Figure III-21**. In **Tab. III-5**, also the measured target detection parameter (namely the SINR on focused image) is reported. These values are obtained by means of averaging over the three point-like targets present in the image. Slight deviations from theoretical values are due to intrinsic SAR operation in stripmap mode, and are experienced even with no ECCM implementation. On the other hand, it is interesting to notice that, adding both jammer noise samples and ECCM countermeasures, only limited further degradations appear. Similar results can be derived for the airborne-HT scenario as well as for the spaceborne case.

As a result of the analysis conducted in Sections III.4.1 and III.4.2 , is evident that the implementation of a pulse-to-pulse antenna nulling allows to guarantee a proper SAR operability in a jamming environment both in terms of acceptable interference rejection and of pulse response quality parameters. It is worth to notice that these analysis have been conducted under the ideal hypothesis of a complete knowledge of the jammer DOA. This makes possible an error free derivation of the nulling weights to be used for disturbance cancellation. Actual achievable performance will deteriorate from these depending on the available accuracy level of the knowledge jammer DOA, as described in the following sections.

III.4.3 Evaluation of the computational cost

The importance of a computational cost evaluation is related to the possibility of a real-time on-board implementation of the antenna nulling technique here proposed. Given the pulsed characteristic of a SAR system, a real-time on-board application is possible only if the required computational load can be executed during the single PRT with available cots.

In general, the antenna nulling implementation requires two different steps: the nulling weights evaluation and the nulling weights application. The computational cost of the first step highly depends on the considered nulling technique and on the available information on the jamming environment. The application of nulling weigths to received data samples to perform interference rejection has no additional computational load since the required complex products can be realized using attenuators and phase shifters connected to the receiving radiating elements. In both cases, the overall computational burden is related to the available number of DOF as well as the selected weights update frequency. In the case under exam (error-free *a priori* knowledge of the jammer DOA) the traditional steps for nulling weights evaluation are reported in **Figure III-24**. In particular, the jammer steering vector **V** and the pointing steering vector **s** have dimensions $1 \times N_{ELEM}$, while the covariance matrix **M** has dimensions

$N_{ELEM} \times N_{ELEM}$, where N_{ELEM} is the number of radiating elements constituting the SAR phased array antenna. It is well known that, for the simple case of a single jammer interference scenario and by recalling the Shermann-Morrison-Woodbury lemma in [37], nulling weigth vector **w** can be derived without any explicit covariance matrix inversion. In addition, it will be shown that **w** can be calculated only through vectors manipulation, not creating any big matrix structure. This allows a huge reduction of the computational cost. To show this, let us recall the expression for the inverse disturbance covariance matrix given by the Shermann-Morrison-Woodbury lemma:

$$\mathbf{M}^{-1} = \frac{1}{\sigma_n^2}\left[\mathbf{I} - \frac{\mathbf{V}(\varphi_J,\theta_J)\cdot\mathbf{V}^H(\varphi_J,\theta_J)}{\frac{\sigma_n^2}{\sigma_J^2} + \mathbf{V}^H(\varphi_J,\theta_J)\cdot\mathbf{V}(\varphi_J,\theta_J)}\right]. \qquad \text{Eq. III-2}$$

The weight vector **w** can be then derived directly as:

$$\mathbf{w} = \mathbf{M}^{-1}(\varphi_J,\theta_J)\cdot\mathbf{s}. \qquad \text{Eq. III-3}$$

Substituting Eq. III-2 in Eq. III-3 and neglecting the dependency on the jammer DOA for simplicity, we have:

$$\mathbf{w} = \frac{1}{\sigma_n^2}\mathbf{I}\cdot\mathbf{s} - \frac{\mathbf{V}\cdot\mathbf{V}^H\cdot\mathbf{s}}{\frac{\sigma_n^2}{\sigma_J^2} + \mathbf{V}^H\cdot\mathbf{V}}, \qquad \text{Eq. III-4}$$

where **I** is the identity matrix of size $N_{ELEM} \times N_{ELEM}$. First of all, we notice that the product $\mathbf{I}\cdot\mathbf{s}$ is simply equal to **s** and doest not require any $N_{ELEM} \times N_{ELEM}$ matrix storage.

Starting from **V** and **s**, **w** can be derived following some simple matrix manipulations, resulting in an associated computational cost of $5N_{ELEM}$ complex products. It is worth to notice that, involving any $N_{ELEM} \times N_{ELEM}$ matrix manipulation in the derivation of **w**, the computational cost would be at least $O(N_{ELEM}^2)$ complex products.

III.5 *Uncertainty in the a priori knowledge of the jammer DOA*

The analysis conducted up to now can be considered as a good ideal reference situation, but the jammer DOA knowledge cannot be error-free in a realistic scenario. Therefore, in this section we introduce an estimation error in the jammer DOA knowledge both in the azimuth and in the elevation plane. The achievable cancellation performance will deteriorate from the ideal case of an error-free jammer DOA knowledge (analysis conducted in the previous paragraphs) as the level of estimation accuracy gets worse. We consider two possible models of the estimation error. In the first case we refer to a uniformly distributed error within a bounded interval, while in the second case we refer to a zero mean Gaussian distributed error. Performing the following substitutions:

$$\begin{aligned} u_J &= \cos\varphi_J \cos\theta_J \\ v_J &= \sin\theta_J \end{aligned} \qquad \text{Eq. III-5}$$

and indicating with apex 0 the error-free DOA estimation, the two models yield to the following estimation error probability density functions:

$$p_{u_J,v_J}(u_J,v_J) = \frac{1}{\Delta u_J}\frac{1}{\Delta v_J} rect_{\Delta u_J}\left(u_J - u_J^0\right) rect_{\Delta v_J}\left(v_J - v_J^0\right) \qquad \text{Eq. III-6}$$

for the uniform distribution, and

$$p_{u_J,v_J}(u_J,v_J) = \frac{1}{2\pi\sigma_{u_J}\sigma_{v_J}} \exp\left\{-\frac{\left(u_J - u_J^0\right)^2}{2\sigma_{u_J}^2}\right\} \exp\left\{-\frac{\left(v_J - v_J^0\right)^2}{2\sigma_{v_J}^2}\right\} \qquad \text{Eq. III-7}$$

for the normal distribution. Δu_J and Δv_J define the bounded interval in the (u_J, v_J) plane for the uniform distribution, while $\sigma_{u_J}^2$ and $\sigma_{v_J}^2$ indicate the variances of u_J and v_J, respectively. It is worth to notice that, supposing uniform the distribution error of ϕ_J and θ_J, the assumption of an analogous

distribution for u_J and v_J is not be correct in general. However, this assumption will be considered anyway in the following, given that a small entity of the estimation error is expected. Obviously, for the uniform distribution case, the following relations hold:

$$\begin{aligned}\sigma_{u_J} &= \frac{\Delta u_J}{\sqrt{12}} \\ \sigma_{v_J} &= \frac{\Delta v_J}{\sqrt{12}}\end{aligned} . \qquad \text{Eq. III-8}$$

To make possible a comparison between the normal and the Gaussian distribution, the performance evaluation analysis will be conducted varying the standard deviation of the estimation error, using the relations in Eq. III-8.

A viable solution to make the system robust to jammer DOA uncertainty, is to syntesize an adapted pattern with a "wide" depression around the available estimation. This should take into account for jammer DOA estimation errors. Obviously, the required width of the depression depends on the estimation accuracy level. In the following sections, three different approaches will be proposed for synthesis of patterns with wide depressions. The two first approaches aim to define a set of nulling weights able to reject a jammer impinging not from a specific DOA, but from an "interval of jammer DOAs". This is obtained integrating the disturbance covariance matrix or its inverse over "significant interval of DOAs". The third approach aims to syntesize a wide depression in the adapted pattern simply putting adjacent null constraints nearby the estimated jammer DOA.

III.5.1 Integral nulling strategies

As well known [36], the overall covariance matrix can be expressed as the sum of a thermal noise term and of a jammer term which depends on the jammer steering vector $\mathbf{V}(u_J, v_J)$:

$$\mathbf{M} = \sigma_n^2 I + \mathbf{M}^J(u_J, v_J) = \sigma_n^2 \mathbf{I} + \sigma_J^2 \cdot \mathbf{V}(u_J, v_J)\mathbf{V}^H(u_J, v_J) \qquad \text{Eq. III-9}$$

where σ_n^2 and σ_J^2 indicate the thermal noise and the jammer powers, respectively. Starting from **M**, the optimal nulling weights for interference rejection can be simply obtained inverting the covariance matrix **M** and then multiplying for the pointing steering vector. Both the strategies here considered are based on the idea that the probability density functions in Eq. III-6 and in Eq. III-7 define a "significant jammer DOA interval" to be considered for the antenna nulling weights determination. The first idea [36] is to average the jammer term ($\mathbf{M}^J$) over this "significant jammer DOA interval", yielding to the following expression for the mean jammer term:

$$\overline{\mathbf{M}}^J = \iint_{(u,v)\in\Omega} \mathbf{M}^J(u_J, v_J) p_{u_J,v_J}(u_J, v_J) du_J dv_J \,. \qquad \text{Eq. III-10}$$

The resulting overall covariance matrix to be inverted for optimum weights determination is then:

$$\overline{\mathbf{M}} = \sigma_n^2 I + \overline{\mathbf{M}}^J \qquad \text{Eq. III-11}$$

This nulling weights determination strategy will be referred to as "integral over *M*" in the following.

The second strategy is derived averaging the inverse of the covariance matrix (i.e. $\mathbf{M}^{-1}$) instead of averaging the covariance matrix **M** itself, resulting in the derivation of a "mean optimum filter". Using the Shermann-Morrison-Woodbury lemma, [37], the mean inverse covariance matrix can be expressed as:

$$\overline{\mathbf{M}^{-1}} = \iint_{(u,v)\in\Omega} \frac{1}{\sigma_n^2}\left[\mathbf{I} - \frac{\mathbf{V}(u_J, v_J)\cdot\mathbf{V}^H(u_J, v_J)}{\frac{\sigma_n^2}{\sigma_J^2} + \mathbf{V}^H(u_J, v_J)\cdot\mathbf{V}(u_J, v_J)}\right]\cdot p_{u_J,v_J}(u_J, v_J) du_J dv_J = \qquad \text{Eq. III-12}$$

$$= \frac{1}{\sigma_n^2}\mathbf{I}\underbrace{\iint_{(u,v)\in\Omega} p_{u_J,v_J}(u_J, v_J) du_J dv_J}_{=1} - \frac{1/\sigma_n^2}{\frac{\sigma_n^2}{\sigma_J^2} + \mathbf{V}^H\cdot\mathbf{V}} \iint_{(u,v)\in\Omega} \mathbf{V}(u_J, v_J)\cdot\mathbf{V}^H(u_J, v_J)\cdot p_{u_J,v_J}(u_J, v_J) du_J dv_J$$

This second weights determination strategy will be referred to as "integral over M^{-1}" in the following analysis.

Single-pulse SINR varying the estimation accuracy

In the following, the "integral over *M*" and the "integral over M^{-1}" strategies will be analysed in terms of achievable single-pulse SINR for the airborne-LT and for the airborne-HT scenarios varying the standard deviation σ_{u_J}. The analysis will be conducted on the azimuth dimension only, since this is the direction more affected by jammer DOA variations in a SAR system. Recalling Eq. III-2 and Eq. III-8, the selected range of variation of σ_{u_J} corresponds to an estimation error of the jammer DOA ϕ_J from 0 to half of the azimuth antenna main beamwidth (i.e. $\Delta\varphi_{4dB}$). The analysis is first presented referring to the airborne-LT scenario. In particular, the uniform distribution error modelization is reported in **Figure III-25** and the Gaussian distribution error modelization in **Figure III-26** considering a jammer impinging on the first azimuth antenna sidelobe (jammer close to the steering direction). **Figure III-27** and **Figure III-28** show analogous curves considering a jammer impinging on the 20th azimuth antenna sibelobe (jammer far away from the steering direction). **Figure III-29** to **Figure III-32** show analogous curves for the airborne-HT scenario. As apparent, for the considered cases, a better performance of the "integral over *M*" strategy is experienced. It is worth to notice that, for a jammer DOA far away from the steering direction, all the considered approaches show a very similar behaviour.

Single-pulse SINR varying the jammer DOA

The same averaging strategies considered above (i.e. "integral over *M*" and "integral over M^{-1}"), are now compared in terms of single-pulse SINR versus jammer DOA (azimuth main cut only), for the airborne-HT scenario. In particular, the analysis has been conducted for two fixed values of the standard deviation of the jammer's DOA estimation error equal to a tenth and a half of the azimuth antenna main

beamwidth, respectively. These two standard deviation values should model two sample cases of fine and coarse jammer DOA estimate, respectively. **Figure III-33** and **Figure III-34** show the obtained results for the "fine estimate" case under the uniform error distribution assumption and under the Gaussian distribution error assumption. **Figure III-35** and **Figure III-36** show analogous comparison for the "coarse estimate" case. As apparent, as well as in the previous analysis, the "integral over M" strategy allows to achieve better performance. To investigate the reason of no acceptable cancellation level for the "integral over M^{-1}" strategy, an evaluation of the adapted patterns for a 1st azimuth sidelobe jammer in the "fine estimation" case has been conducted for the "integral over M" and for the "integral over M^{-1}" strategies. Obtained results are reported in **Figure III-37**. As apparent, the "integral over M^{-1}" strategy syntesizes a less deep depression in the neighborhood of the jammer DOA, which does not allow to completely cancel the disturbance.

III.5.2 Constrained antenna nulling

Given the high available number of DOFs, it is interesting to investigate the possibility to put several constraints to the adapted pattern. A comprehensive study on the constraints utilization in array processing can be found in [40]. An analysis of the possible utilization of constrained beamforming with a limited available number of DOFs (i.e. referring to a spaceborne based SAR) can be found in [38]. In general, constraints on the adapted antenna pattern can be used for two different reasons:

- jammer cancellation;
- mainbeam shape preservation.

The former are intended to guarantee an acceptable jammer rejection capability. To this end, null constraints can be put in the jammer DOA. The use of multiple null constraints in the neighbourhood of

the estimated jammer DOA allows to enlarge the depression in the adapted pattern making the system more robust against jammer's DOA variation and/or uncertainty.

The latter include directional as well as first and second derivative constraints which have the scope to preserve the mainbeam shape. In fact, an unconstrained pulse-to-pulse antenna nulling can affect the SAR azimuth pulse response, introducing an amplitude modulation in the useful received SAR data. In [38] it has been shown that this unwanted effect can be limited using proper sets of constraints applied to the antenna mainbeam.

In this paragraph we investigate the single-pulse SINR versus jammer DOA (azimuth main cut only) achievable putting a growing number of null constraints in the neighbourhood of the estimated jammer DOA, for a given jammer's DOA estimation accuracy (a tenth of the azimuth antenna main beamwidth), in the airborne-HT scenario. **Figure III-38** reports the obtained results for the cases of *L=1, 3, 5* nulls equally spaced in the jammer DOA interval of interest[8] in comparison with the "integral over *M*" strategy (uniform error distribution, estimation accuracy equal to a tenth of the azimuth antenna main beamwidth). It is worth to notice that the "5 null constraints" case yields to performance comparable with the "integral over *M*" strategy. As apparent from **Figure III-38**, as the number of null constraints increases, the SINR notch gets larger. This is the price to be paid for a system more robust to jammer's DOA variations.

To investigate the potential of a wide depression in the adapted pattern in presence of a given uncertainty in the jammer's DOA estimation the following analysis has been conducted. The effective level of achievable SINR in presence of an uncertainty in the jammer's DOA estimation has been evaluated, varying the estimation accuracy itself. Therefore, for each estimation accuracy value under

[8] The jammer DOA interval of interest is set by the estimation accuracy, in this particular case the estimation accuracy is equal to a tenth of the azimuth antenna beamwidth.

exam, a Monte Carlo simulation has been performed with 10^5 trials considering an airborne-HT scenario with a 1st azimuth sidelobe jammer. For each single trial, the nulling weights are evaluated on the basis of the DOA estimation and a SINR value can be calculated considering the real jammer DOA. These SINR values are then averaged to obtain the curves reported in **Figure III-39**. As apparent, enlarging the depression in the adapted pattern the system results more robust to DOA estimation errors. The "integral over *M*" strategy always allows to achieve higher performance w.r.t. the considered constraints configurations. Moreover, the "3 null constraints" case yields better performance with respect to the other null constraint configurations. **Figure III-40** shows a zoom of **Figure III-39** to highlight the behaviour of the three constrained nulling strategies with zero estimation error. The SINR values obtained in this case are the same as the SINR values readable for a 1st azimuth sidelobe jammer (ϕ_J=*88.66*°) in **Figure III-41**, which represents a performance upper bound, since no Monte Carlo simulation has been conducted in this case. As apparent, the upper bound of the "5 null constraints" case is much lower than the two other constrained nulling cases, thus resulting in a worse behaviour in the Monte Carlo simulation. On the other hand, the "1 null constraint" syntesizes an adapted pattern with a narrow null which it is not robust in presence of estimation errors.

Evaluation of the azimuth SAR pulse response

The nulling strategies "3 null constraints" and "integral over *M*", that yield better cancellation performance in the previous analysis, are analyzed in terms of achievable image quality. To this end, the airborne-HT scenario will be considered, with the jammer impinging on the 1st azimuth antenna sidelobe during the synthetic aperture and for the "fine estimate" jammer's DOA case. The two nulling stategies are compared with the theoretical SAR pulse response achieved not applying any nulling strategy and with the traditional nulling strategy applicable with an available error-free jammer DOA

estimation. Achieved SAR azimuth pulse responses are reported in **Figure III-42**. As apparent, the main effect on the pulse response is the increased SLR value experienced with the "3 null constraints" and "integral over *M*" strategies. This effect is due to amplitude modulation on azimuth data envelope caused by antenna gain variation in target direction during synthetic aperture, see **Figure III-43**. This effect introduces paired echoes in the resulting SAR pulse response, hence degrading the side lobe level. Even evaluating the azimuth SAR pulse response, the "integral over *M*" results the strategy able to achieve best overall performance when the jammer DOA is known with a non zero uncertainty.

Evaluation of the computational cost for weights determination

The evaluation of the computational cost for the constrained antenna nulling strategies will be derived considering the required number of complex products, as in Section III.4.3 . Even adopting the constrained antenna nulling strategies, the weights vector **w** can be derived without explicit inversion of $N_{ELEM} \times N_{ELEM}$ matrices, using the Shermann-Morrison-Woodbury lemma. In particular, as illustrated in [40], the weights vector can be derived as:

$$\mathbf{w} = \mathbf{M}^{-1}\mathbf{C} \cdot \left(\mathbf{C}^{H}\mathbf{M}^{-1}\mathbf{C}\right)^{-1}\mathbf{G}\,, \qquad \text{Eq. III-13}$$

where **C** is a $N_{ELEM} \times L$ matrix containing in each column the steering vector of the DOA where a constrained value is set, and **G** is a $L \times 1$ vector containing the constrained adapted antenna pattern values. Substituting the Eq. III-2 in Eq. III-13, we have

$$\mathbf{w} = \left(\frac{\mathbf{C}}{\sigma_n^2} - \frac{\mathbf{V}\mathbf{V}^{H}\mathbf{C}}{\frac{\sigma_n^2}{\sigma_J^2} + \mathbf{V}^{H}\mathbf{V}}\right) \cdot \left(\mathbf{C}^{H}\left(\frac{\mathbf{C}}{\sigma_n^2} - \frac{\mathbf{V}\mathbf{V}^{H}\mathbf{C}}{\frac{\sigma_n^2}{\sigma_J^2} + \mathbf{V}^{H}\mathbf{V}}\right)\right)^{-1}\mathbf{G}\,. \qquad \text{Eq. III-14}$$

As apparent, the above expression has the structure

$$\mathbf{w} = \mathbf{A} \cdot \left(\mathbf{C}^{H}\mathbf{A}\right)^{-1}\mathbf{G} \qquad \text{Eq. III-15}$$

where **A** is a $N_{ELEM} \times L$ matrix. Starting from **V** and **C**, **w** can be derived following some simple matrix manipulations, resulting in an associated computational cost of $2N_{ELEM} \cdot L^2 + 5N_{ELEM} \cdot L + N_{ELEM} + 2L^3/3$ complex products. It is worth to notice that, for the limited number of constraints here considered (i.e. $L \leq 5$), the resulting computational cost is $O(N_{ELEM} \cdot L)$.

III.6 *Nulling weights update every K slow-time pulses*

Up to now, a pulse-to-pulse antenna nulling weights update strategy has been considered for the analysis. It is interesting to evaluate the impact of maintaining the same set of nulling weights for several subsequent slow-time intervals. Both the effects on the cancellation performance and on the SAR pulse response will be investigated. Recalling the error models introduced in Section III.5 , a weights update every *K* pulses can be reconducted to an uncertainty in the jammer DOA knowledge. In particular, considering a linear variation of the azimuth jammer DOA (i.e. ϕ_J) during the acquisition and given an accuracy σ_{φ_J} in the jammer DOA knowledge, the weights update every *K* pulses leads to an equivalent accuracy $\sigma_{\varphi_J}^{eq}$ given by:

$$\sigma_{\varphi_J}^{eq} = (K-1)\frac{\Delta\varphi_{4dB}}{N_{az}} + \sigma_{\varphi_J}, \qquad \text{Eq. III-16}$$

where $\Delta\varphi_{4dB}$ is the azimuth antenna main beamwidth, and N_{az} is the number of processed PRTs.

In the following analysis, the single-pulse SINR versus the jammer's DOA is presented for the airborne-HT scenario. In particular, a jammer impinging on the first azimuth antenna sidelobe is considered and the SINR is evaluated only for the jammer's DOAs interested during a synthetic aperture. The analysis has been conducted for three different values of σ_{φ_J} (i.e. $\sigma_{\varphi_J} = 0, \frac{1}{10}\Delta\varphi_{4dB}, \frac{1}{2}\Delta\varphi_{4dB}$) and for four different frequency update values (i.e. *K=1, 5, 10, 15*) yielding to 12 different values of $\sigma_{\varphi_J}^{eq}$. For each single case, the "integral over *M*" and the "integral over M^{-1}" are considered. For comparison, both the SINR achievable following a pulse-to-pulse weights update strategy and the SINR achievable maintaining the same optimal set of nulling weights for *K* subsequent slow-time instants are

also reported. **Figure III-44** to **Figure III-58** show the obtained results under the uniform error distribution assumption. The black curve represents the "pulse-to-pulse" update strategy, which is here considered as an upper bound for performance evaluation. As apparent, the "integral over M^{-1}" strategy does not yield to acceptable performance level. It is interesting to notice that the performance of the "weights update every K pulses" strategy deteriorates for those pulses where the weights are not calculated, however this behavior is much less evident when the "integral over M" strategy is considered. In fact, the "integral over M" strategy is able to syntesize a wider depression in the adapted pattern able to counteract the jammer's DOA variation due to platform motion. The capability to synthesize a wider depression in the adapted pattern is paid in a less deep notch, which causes a slight SINR degradation w.r.t. the pulse-to-pulse update strategy. It can be shown that analogous results can be obtained under the Gaussian distribution error assumption.

III.7 *Fully adaptive ECCM*

We consider, as a "fully adaptive" system, a system with no a priori information regarding the position of the jammer, i.e. no knowledge of the disturbance environment is available to the system. Therefore, such a system should be able to collect information on the disturbance environment (i.e. the DOA and, potentially, the number of interfering sources) by itself. The collection of information on the disturbance (interference plus noise) is performed by means of covariance matrix estimation from secondary data (i.e. data containing only disturbance contribution). The secondary data collection allows the system to estimate the disturbance covariance matrix at a channel level. The estimated covariance matrix can be then inverted to determine the antenna nulling weights to be applied at channel level to syntesize an adapted pattern for jammer rejection. It is clear that a "fully adaptive" ECCM SAR system should have at least two parallel receiving channels to counteract a single jammer, since each available receiving channel results in an available Degree Of Freedom (DOF). One of the available receiving channel is connected to the main beam, while the other parallel receiving channels are connected to auxiliary beams. It is well known [31] that, using an antenna nulling scheme with a Multi-channel SAR (M-SAR), to achieve good cancellation performance in a specific DOA, at least one of the auxiliary beams must have in that specific DOA a gain somewhat higher than the main antenna beam. Therefore, to guarantee the desired protection from every possible interference DOA, the set of main and auxiliary antennas has to be properly designed.

Moreover, due to jammer's DOA variation during imaging, the disturbance covariance matrix estimation should be performed periodically.

Data samples free of radar echoes returns can be available, but this strongly depends on the PRF and on the SAR antenna elevation pattern (cross-track), see **Figure III-63**. Hence, two different cases will be investigated in the following. In the former, a pulse-to-pulse covariance matrix estimation can be performed. This can be due to an available temporal interval within the PRT, or due to ad hoc strategies for disturbance matrix estimation (e.g. sliding estimation, diagonal loading). In the latter, a sufficient number of secondary data cannot be collected every PRT, so that the estimation can be performed only periodically. It is worth to notice that the first approach is well suited for airborne M-SAR, given the relatively low PRF values used for those systems. On the other hand, a periodical estimation of the covariance matrix should be a compelled solution in a spaceborne M-SAR system, usually characterized by medium/high PRF values.

III.7.1 Pulse-to-pulse covariance matrix estimation

Airborne SAR usually work with PRF values much lower than spaceborne systems[9]. This makes easier the identification of an available time interval for secondary data collection every PRT. Moreover, since the number of DOFs is limited by the number of available receiving channels, the amount of secondary data to be collected following the "RMB rule" [35] is quite low, allowing a good covariance matrix estimation with limited adaptivity losses.

In a spaceborne scenario, it is possible that only a very limited number of secondary data are available every PRT. In this case, a sliding covariance matrix estimation can be performed, as described below. Indicating with N_S the overall number of required secondary data for covariance matrix estimation (at least twice the number of DOFs, according to the "RMB rule"), we suppose available every PRT only $N_S'=N_S/T$ secondary data samples. Every PRT the covariance matrix is estimated on the latest N_S data

[9] Comparing SAR systems working with analogous carrier frequencies.

samples, thus adding the newest N_S' samples and discarding the oldest N_S'. It is worth to notice that, if no more than N_S' data samples are available every PRT, the only alternative strategy is to perform a covariance matrix estimation every T PRT, maintaining the same estimated covariance matrix for the following T pulses ("batch estimation" approach). We expect that a "sliding" approach would lead to better matrix estimation accuracy than a "batch" strategy, since the information on the disturbance environment is somewhat updated on a pulse-to-pulse basis. Before conducting an analysis on the "sliding" approach effectiveness, we have evaluated the achievable cancellation performance estimating the covariance matrix on a pulse-to-pulse basis with a growing number of secondary data. The aim of this analysis is to identify a favourable value for N_S able to limit the adaptivity losses below 1 dB. **Figure III-59** reports obtained SINR values for a 5 channel spaceborne SAR with a 1st azimuth sidelobe jammer impinging on the antenna. In particular, we have considered $N_S=10, 30, 50$ in comparison with the know disturbance covariance matrix case. As apparent, $N_S=10$, corresponding to the "RMB rule", does not allow to limit the adaptivity losses within 1 dB, whereas this constraint is accomplished increasing N_S up to *30*. Therefore, the value $N_S=30$ will be considered for the following analysis. Once a favourable value of N_S has been selected, referring to the same spaceborne M-SAR system, we have evaluated the single pulse SINR versus the jammer's DOA during a synthetic aperture achievable using a "sliding estimation" approach for $N_S'=1, 5, 10$. In **Figure III-60**, **Figure III-61**, and **Figure III-62** obtained results with a "sliding" approach are shown in solid lines, in comparison with the "batch update" counterparts reported with dotted lines. As apparent, the "batch" strategy tends to the "sliding" strategy performance as N_S' increases. However, for small values of N_S' the pulse-to-pulse matrix estimation update (even if partial) leads higher cancellation performance, comparable with a complete pulse-to-pulse update strategy.

III.7.2 Covariance matrix estimation every T slow-time instants

In a spaceborne SAR sensor, data samples free of radar echoes can be available, but this strongly depends on the PRF and on the SAR antenna elevation pattern (cross-track), see **Figure III-63**. Both of these parameters have a major impact on the SAR system design. The PRF value should be selected to receive all echoes from the swath, correctly sample the instantaneous Doppler band, avoid nadir return and transmission/reception overlap. Moreover the SAR antenna elevation pattern should at least cover the whole range swath and is also often opportunely shaped to reduce range ambiguities. All these constraints can imply that no data samples free of radar returns are available at any range, especially when relatively high PRF values are used.

Strategies for covariance matrix estimation

In this section we propose to estimate the disturbance covariance matrix by avoiding the transmission of the radar pulse in a specific set of slow time instants during the synthetic aperture. In particular, the three following strategies are proposed: (i) Periodic skip of transmissions; (ii) Periodic skip of transmissions modified by pseudorandom shifts; (iii) Pseudorandom selection of the transmission skipping times with constraints.

Periodic skip

In the first proposed approach the selection of the pulse transmissions to skip is done on a periodic basis, namely we choose to avoid one pulse transmission every T ones, as sketched in Figure III-64. Thus, a total of N/T pulse transmissions will be skipped during a synthetic aperture, where N would be the total number of pulses transmitted with constant PRT if no transmission is skipped.

For the periodic skip approach, the collected SAR data $s(n)$ can be written as the difference of two signals $s_1(n)$ and $s_0(n)$, where the former contains all the transmitted pulses while the latter accounts for

the skipped ones. Without loss of generality, $s_1(n)$ and $s_0(n)$ are reported after azimuth phase compensation.

$$s(n) = s_1(n) - s_0(n) = \\ = \begin{cases} 1 - \sum_{m=0}^{N/T-1} \delta(n-(m+1)T-1), & n = 0,...,N-1 \\ 0, & \textit{elsewhere} \end{cases}$$ Eq. III-17

The Discrete Fourier Transform (DFT) of $s(n)$, $F(k)$, is the output of the azimuth focusing filter; note that those DFT are generically computed over P samples ($P \geq N$ Zero Padding).

$$F(k) = F_1(k) - F_0(k)$$ Eq. III-18

where

$$F_1(k) = \sum_{n=0}^{P-1} s_1(n) e^{-j2\pi kn/P} = \sum_{n=0}^{N-1} e^{-j2\pi kn/P}$$ Eq. III-19

$$|F_1(k)| = \sin(\pi k N/P)/\sin(\pi k/P)$$ Eq. III-20

$$F_0(k) = \sum_{n=0}^{P-1} s_0(n) e^{-j2\pi kn/P} = e^{-j2\pi k(T-1)/P} \sum_{m=0}^{N/T-1} e^{-j2\pi kmT/P}$$ Eq. III-21

$$|F_0(k)| = \sin(\pi k N/P)/\sin(\pi k T/P)$$ Eq. III-22

Eq. III-20 represents the SAR azimuth pulse response obtained after image focusing, while Eq. III-22 represents the paired echoes arising when N/T transmissions are skipped. These echoes are periodic of P/T samples and have a peak value of N/T, while N is the SAR response peak value when no transmissions are skipped. The focused image due to the skipped pulse transmissions every T ones shows a peak loss of N/T (out of N) and T paired echoes. To evaluate how much the paired echoes affect the SAR pulse response after focusing, we consider the Peak Paired Echoes Ratio (PPER), that is the

ratio between the focused image and the paired echoes peak values. If the peak value of $F_0(k)$ is higher than the side-lobes of $F_1(k)$, the PPER would be approximately:

$$PPER_{dB} \cong 20\log_{10}(T-1) \qquad \text{Eq. III-23}$$

Eq. III-23 can be used to choose the maximum value for the pulse transmission skipping period if a constraint on the Peak Side-Lobe Ratio (PSLR) of the SAR image is set. **Tab. III-6** shows the peak loss and PPER for several values of T.

Periodic skip with pseudorandom shift

The second proposed approach is similar to the previous one, but every T pulses the one to be kept off is randomly selected among a set of ΔT adjacent slow time instants. The objective of this random shift is to break the periodicity of the missed pulse train thus spreading the energy of the peak of the paired echoes. A sketch of this skipping approach is shown in **Figure III-65**.

Pseudorandom selection with constraints

In the third proposed approach, each transmitted pulse within the synthetic aperture is chosen to be skipped with probability equal to $1/T$. Moreover, to control the minimum and maximum disturbance covariance matrix update period two constraints are set. The first constraint forces a sequence of C_1 pulses to be transmitted after a missed one. The second constraint forces a pulse transmission to be skipped after C_2 subsequent transmitted pulses.

Impact on the SAR azimuth pulse response

In this section we analyze the impact of the three proposed approaches on the azimuth SAR pulse response. In particular, we consider a spaceborne-HT scenario with an overall number of $N=2000$ pulses. For the periodic skip approach we set the skipping period $T=20$, resulting in 100 skipped pulses in a synthetic aperture. The SAR pulse response in **Figure III-66** shows T paired echoes peaks (the

peak loss is due to one of these) and an achieved PPER of *25.57 dB*. For the periodic skip with pseudorandom shift we consider the same value of $T=20$ with a set of several values for ΔT. To select a favourable skipping sequence in terms of PPER a simulation of 10^3 trials has been done; **Tab. III-7** shows the obtained results. To get insight into the issues related with the missed pulse transmissions, we also consider the use of a Hamming taper applied to the useful signal envelope. This is suitable to achieve low SAR pulse response sidelobes. **Figure III-67** shows the improvement that a pseudo random shift of ± 5 allows on the azimuth pulse response. For the pseudorandom selection with constraints, the value of $T=20$ has been considered, resulting in a pulse skipping probability $p_0=0.05$, with a set of values for C_1 and C_2. The skipping sequence favourable in terms of PPER has been selected on 10^3 simulated trials. Results in **Tab. III-8** show a better PPER value achieved with respect to the periodic skip with pseudorandom shift approach, while in **Figure III-68** the normalized tapered SAR response is reported. This is mainly related to a lower number of skipped pulses, resulting in a lower peak loss. In contrast, also the first sidelobes of SAR pulse response have been affected by the missed transmissions. Moreover **Tab. III-9** shows the Integrated Side-Lobe Ratio (ISLR) values obtained for the three approaches. As apparent, the approach (ii), while spreading the energy of the peak of the paired echoes, does not allow an improvement in the ISLR w.r.t. the approach (i), due to the same number of missed transmissions. In contrast, since approach (iii) requires a lower number of skipped transmissions, it achieves a slightly better ISLR. Finally it is useful to notice that the skipping sequence design for the approach (iii) could be performed to achieve the ISLR minimization.

Impact on the interference cancellation capability

In this section we analyze the impact that the disturbance covariance matrix update frequency has on the interference cancellation capability. The analysis is performed in terms of the achievable SINR for a range of DOAs. Due to the random characteristic of the proposed approaches and to the general complexity of the cancellation performance evaluation, the impact will be evaluated with reference to a

spaceborne-HT interference (EIRP of 70 dBW). Moreover the multi-channel system is supposed to have three contemporaneous receiving channels connected to the main SAR antenna, a wide-beam auxiliary antenna and a directive auxiliary antenna. **Figure III-69** shows the SINR obtained with the proposed approaches respectively for a jammer impinging on the antenna from the 1st azimuth sidelobe during a SAR synthetic aperture. The achieved results are compared with the SINR obtained when the weights are computed and updated every PRT (black line). As apparent, better cancellation performance can be achieved when a periodic matrix update is available.

III.8 *Figures*

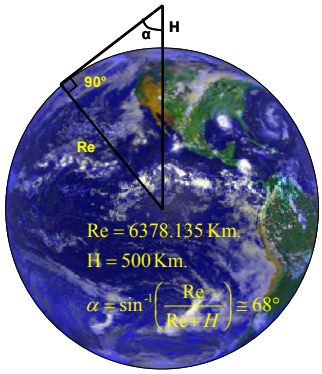

Figure III-1 Possible DOA of the disturbance for a LEO platform radar and a surface-based jamming source

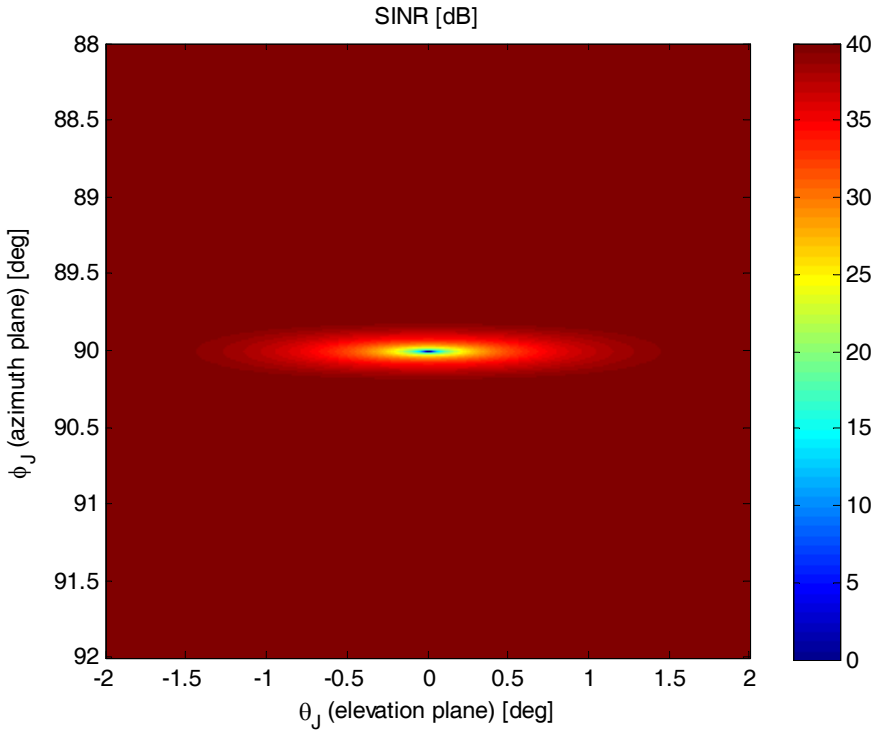

Figure III-2 SINR vs jammer DOA: spaceborne-LT scenario.

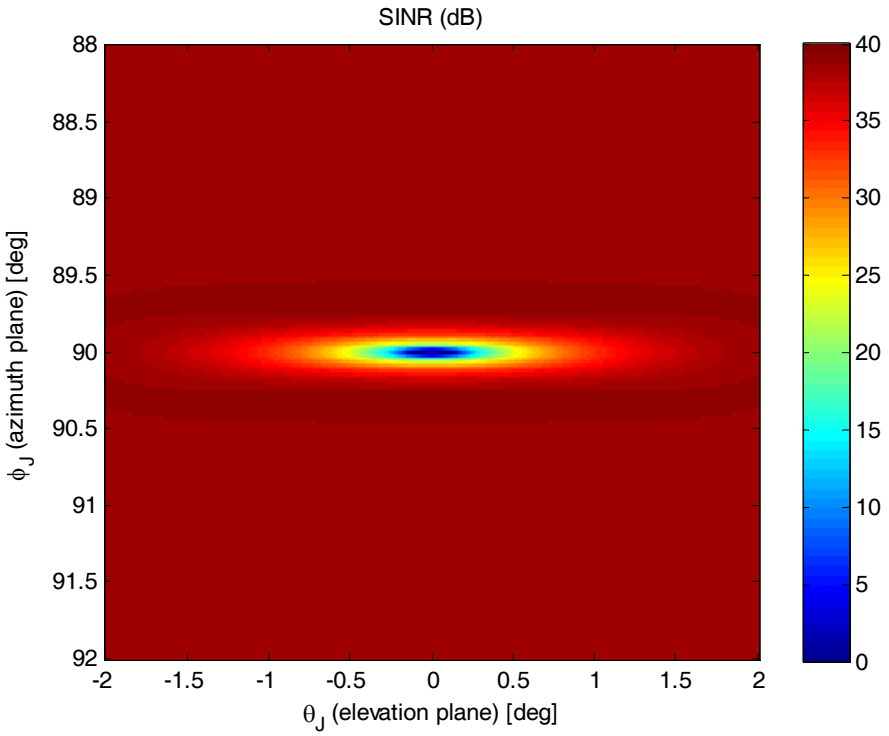

Figure III-3 SINR vs jammer DOA: spaceborne-HT scenario.

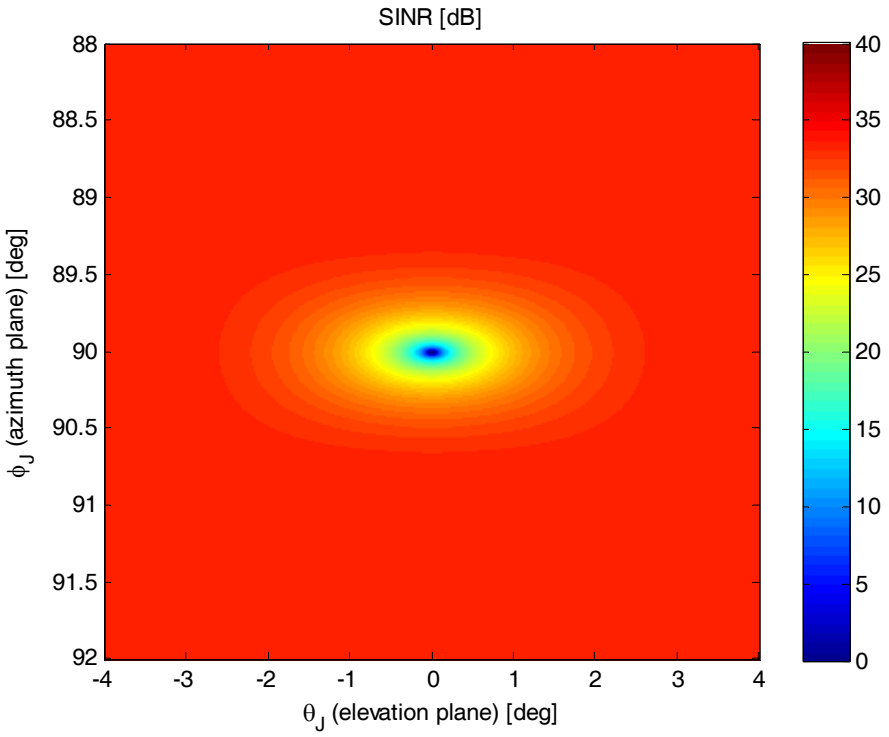

Figure III-4 SINR vs jammer DOA: airborne-LT scenario.

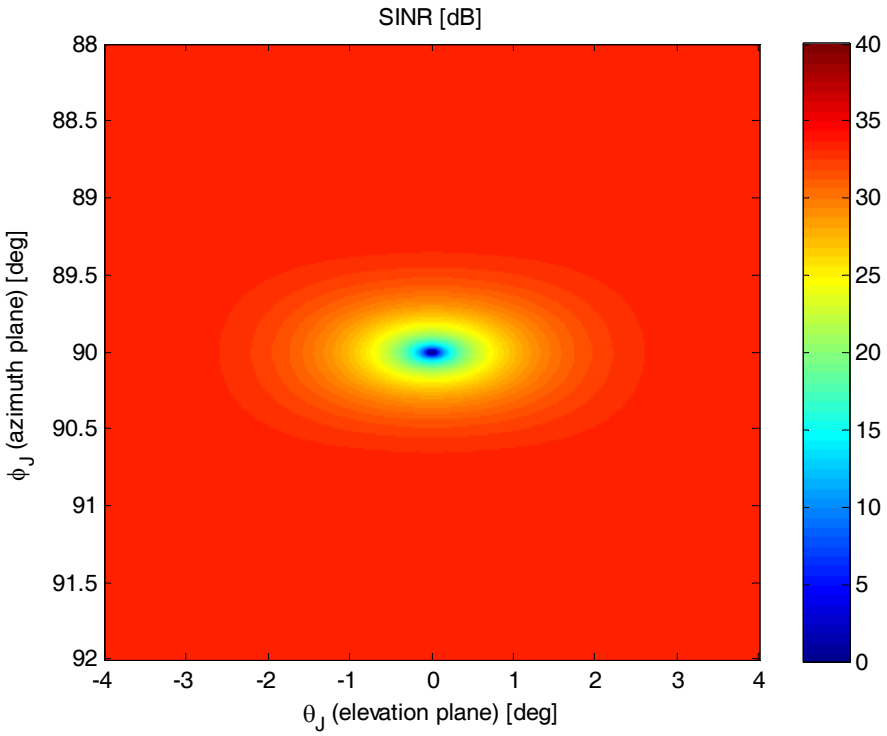

Figure III-5 SINR vs jammer DOA: airborne-HT scenario.

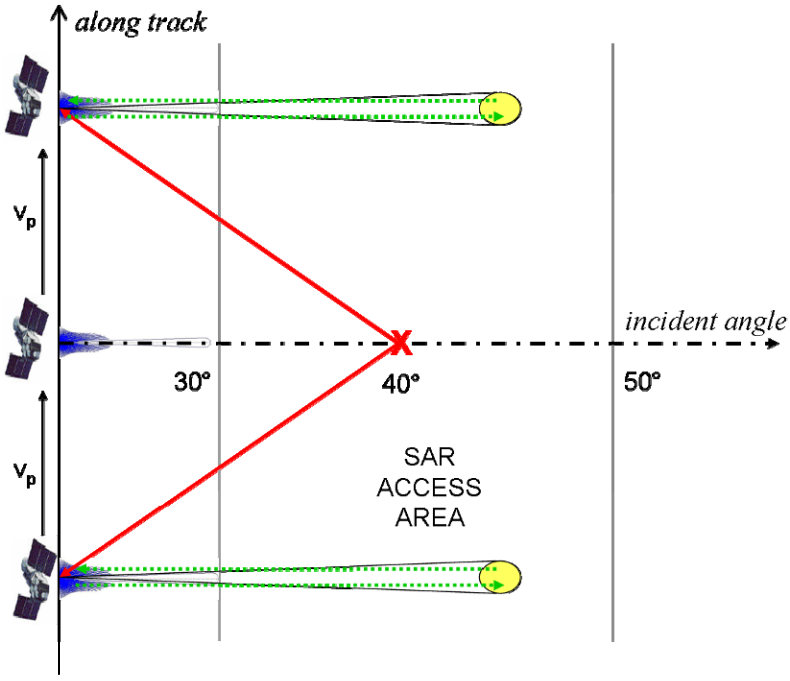

Figure III-6 Spaceborne stripmap interference scenario.

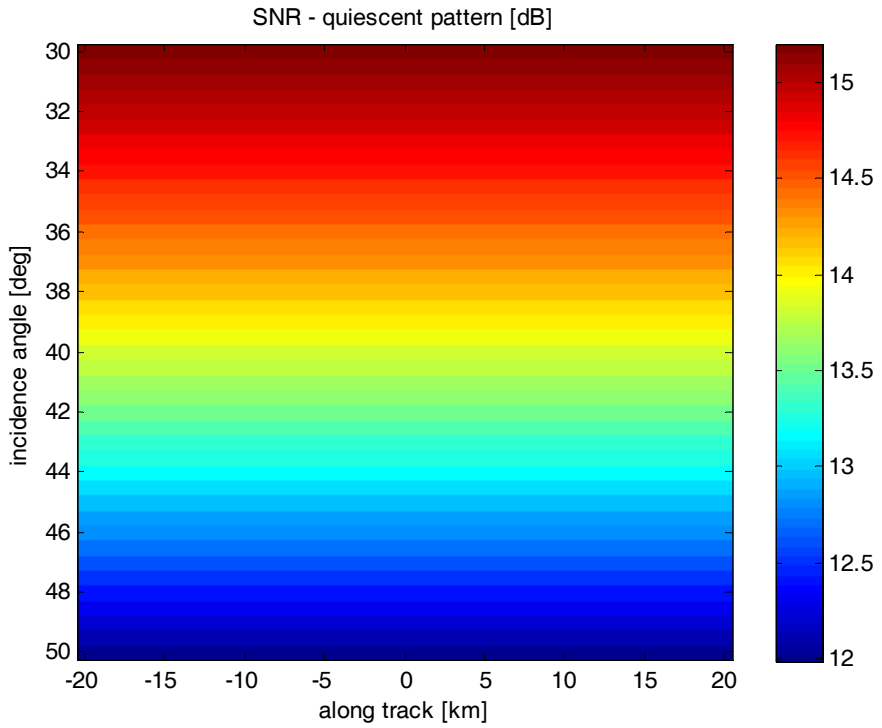

Figure III-7 Map of SNR for the spaceborne scenario (no interference is present)

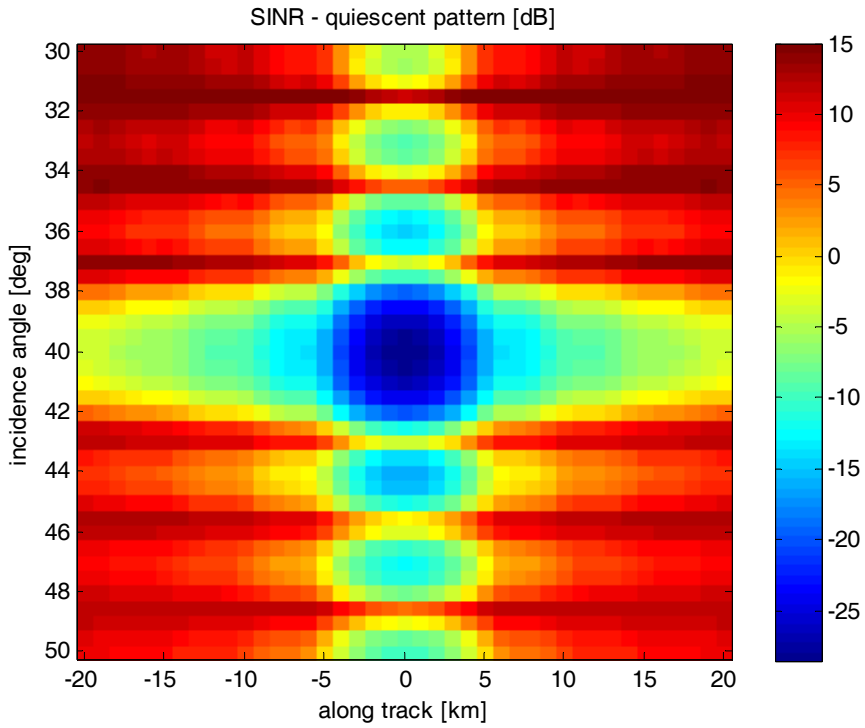

Figure III-8 Map of SINR for the spaceborne-LT scenario: no ECCM applied.

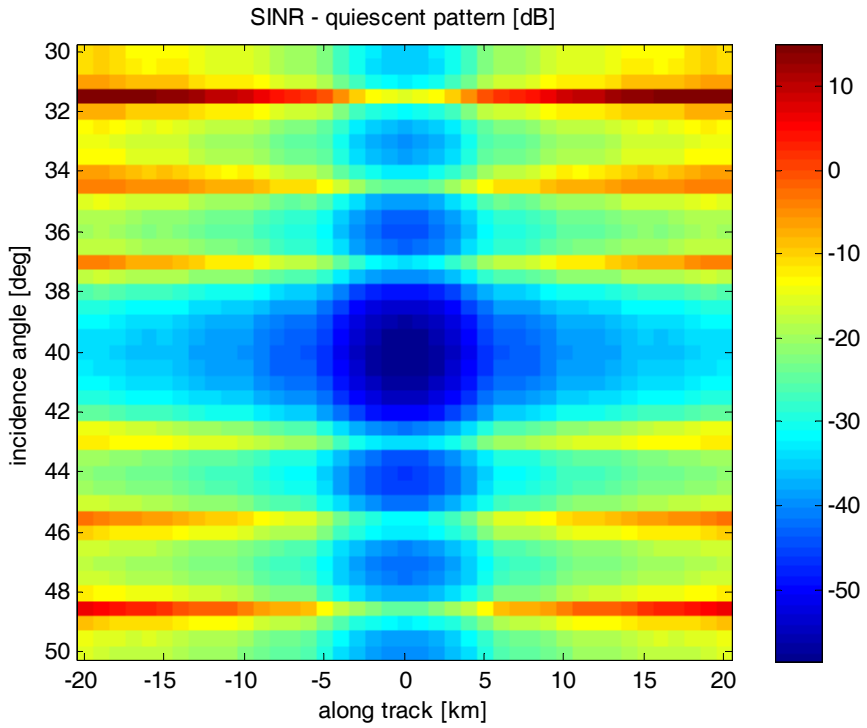

Figure III-9 Map of SINR for the spaceborne-HT scenario: no ECCM applied.

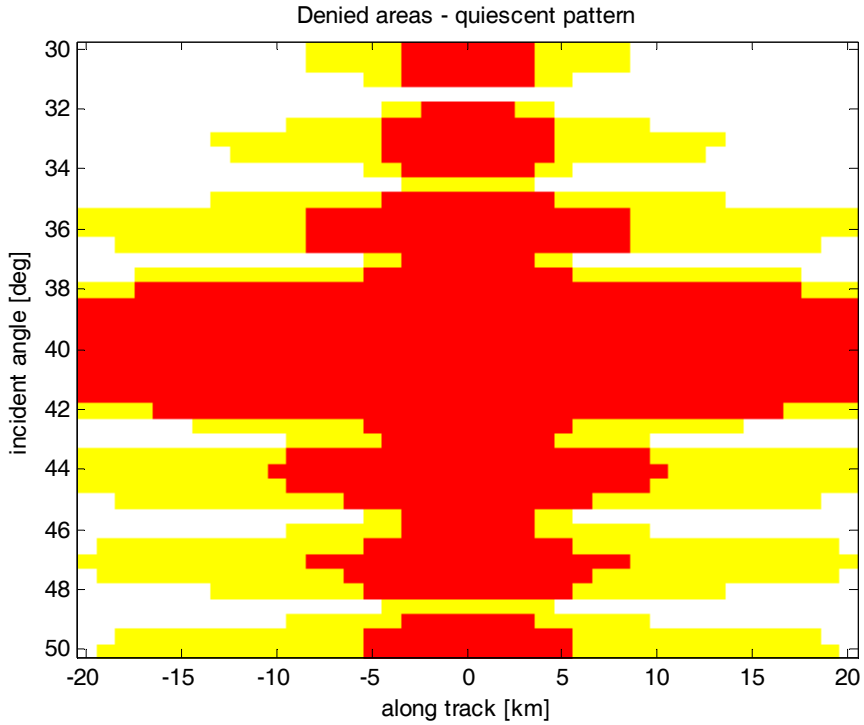

Figure III-10 Denied areas for the spaceborne-LT scenario: no ECCM applied.

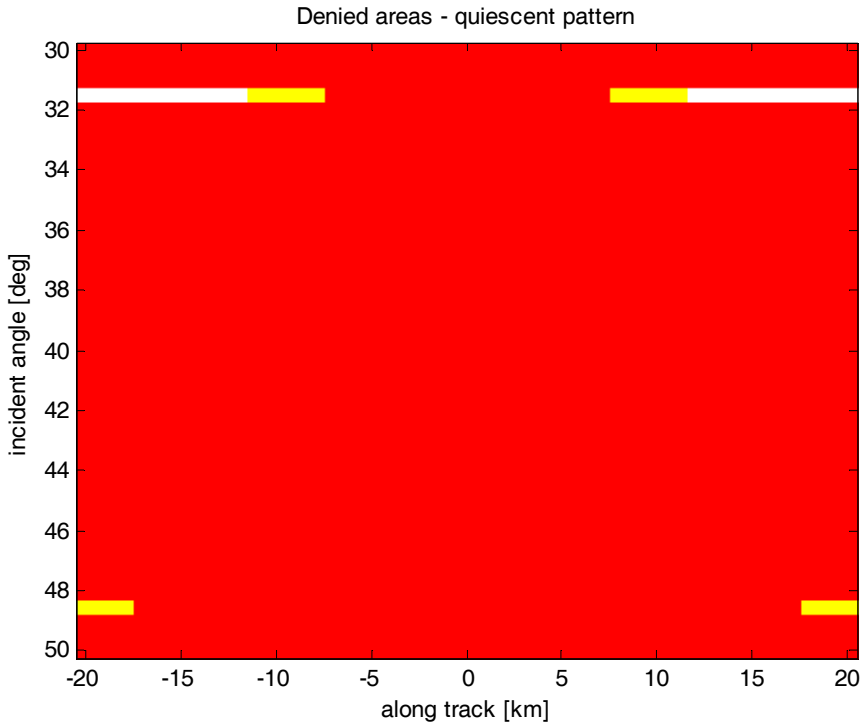

Figure III-11 Denied areas for the spaceborne-HT scenario: no ECCM applied

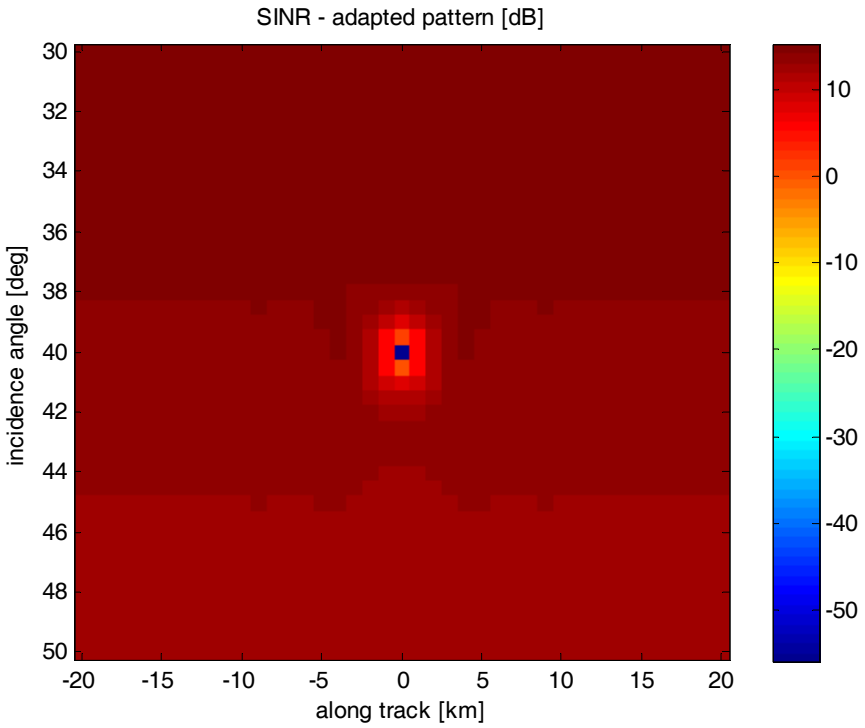

Figure III-12 Map of SINR for the spaceborne-LT scenario

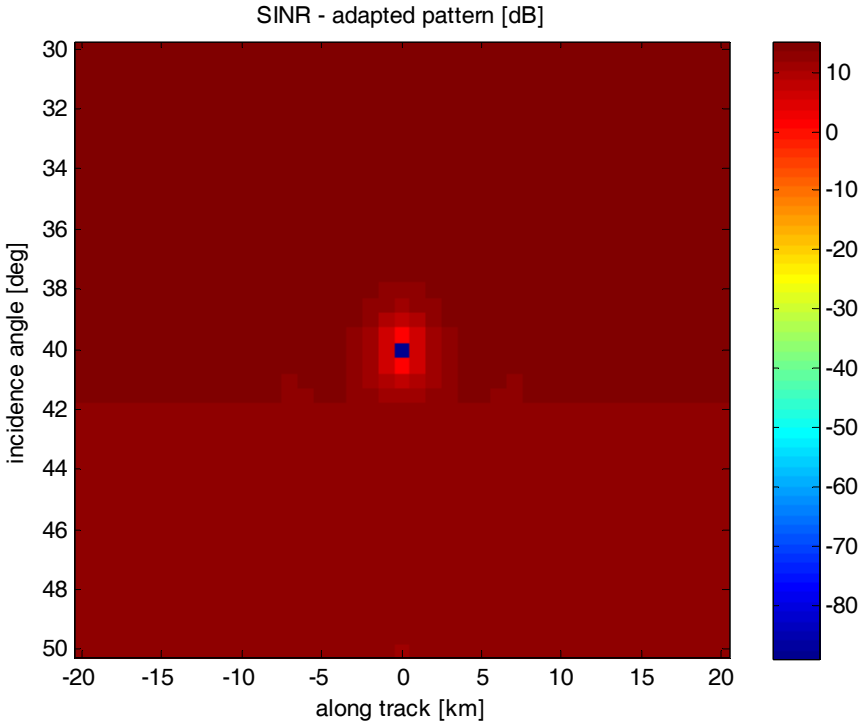

Figure III-13 Map of SINR for the spaceborne-HT scenario

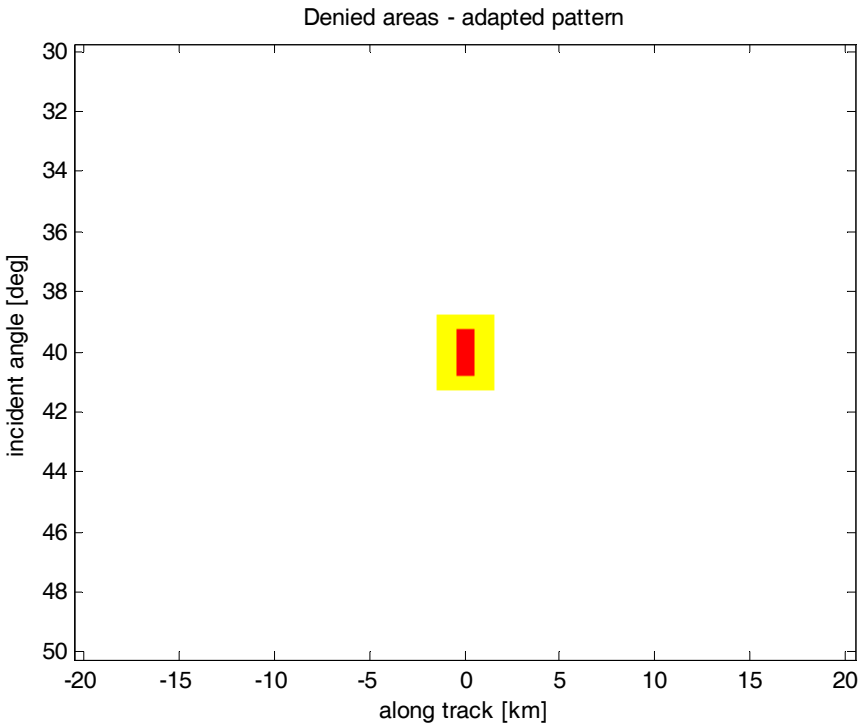

Figure III-14 Map of denied areas for the spaceborne-LT scenario

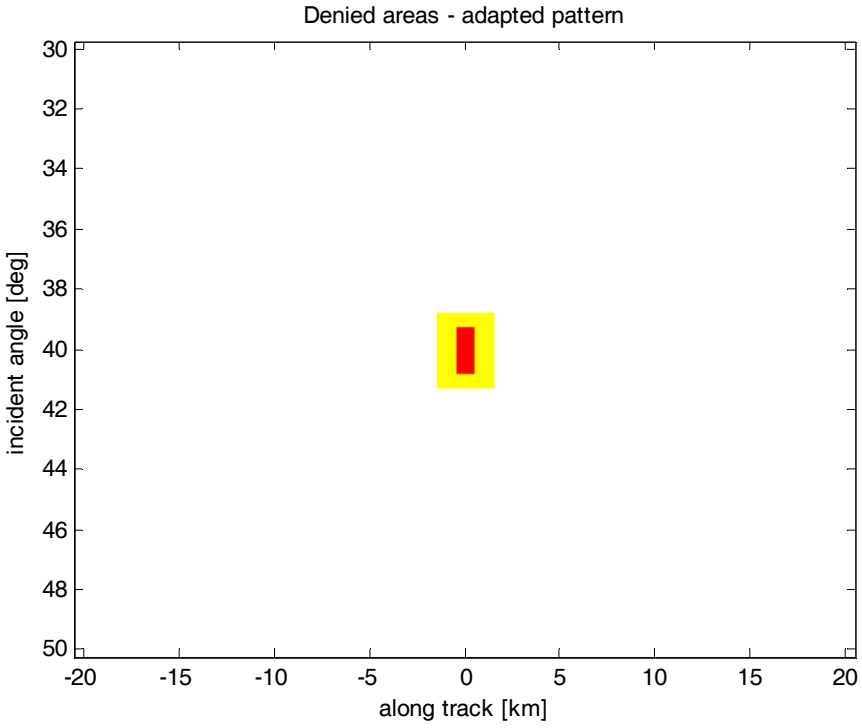

Figure III-15 Map of denied areas for the spaceborne-HT scenario

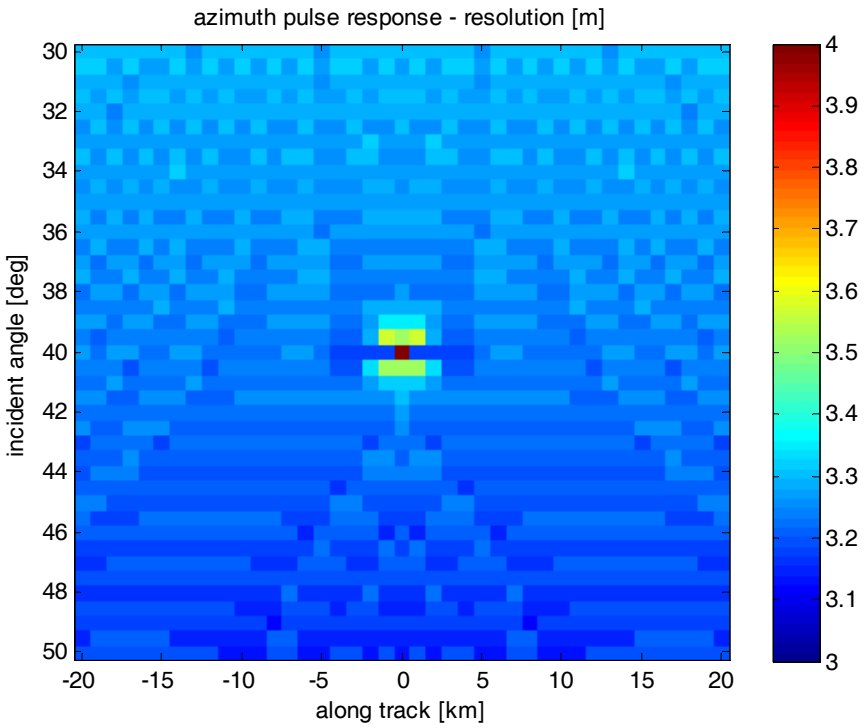

Figure III-16 Azimuth resolution over the grid of targets for the spaceborne-LT scenario

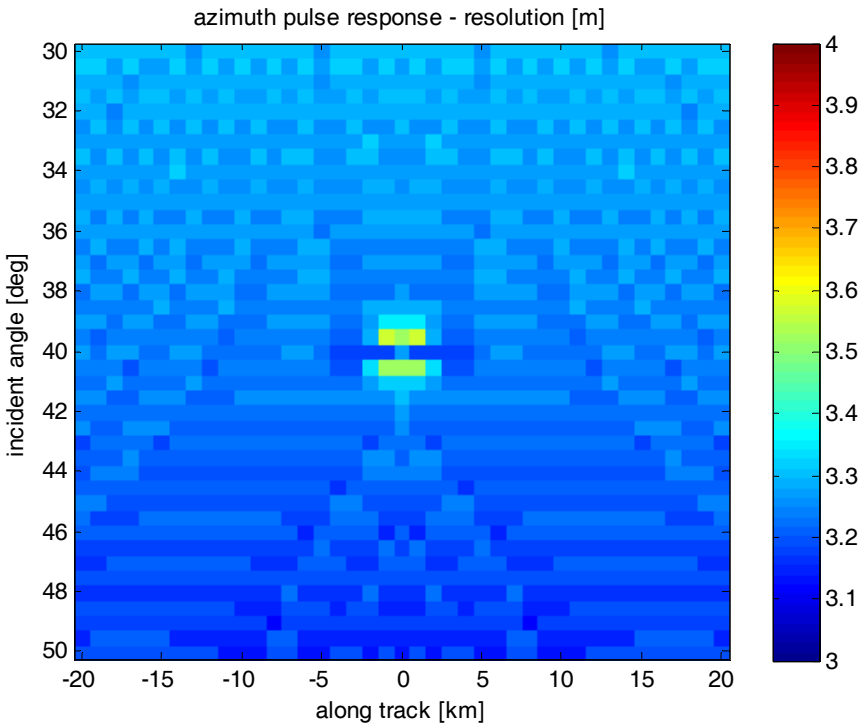

Figure III-17 Azimuth resolution over the grid of targets for the spaceborne -HT scenario

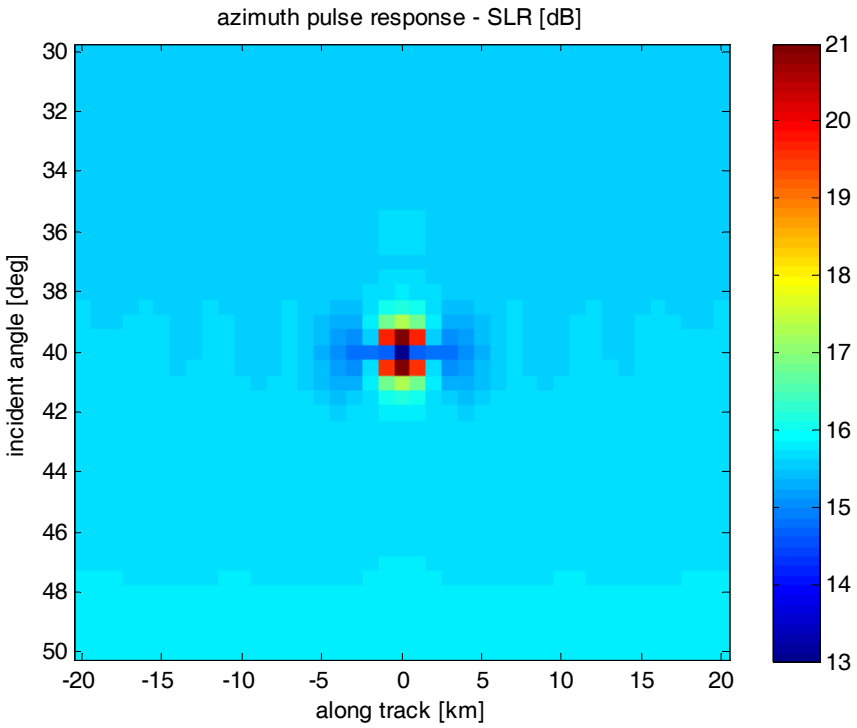

Figure III-18 Azimuth SLR over the grid of targets for the spaceborne-LT scenario

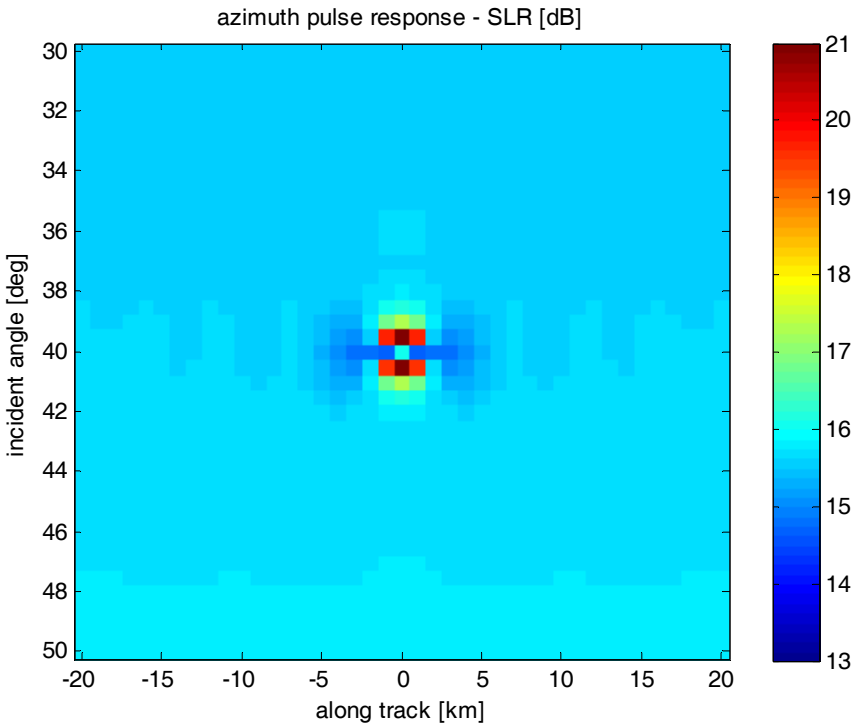

Figure III-19 Azimuth SLR over the grid of targets for the spaceborne-HT scenario

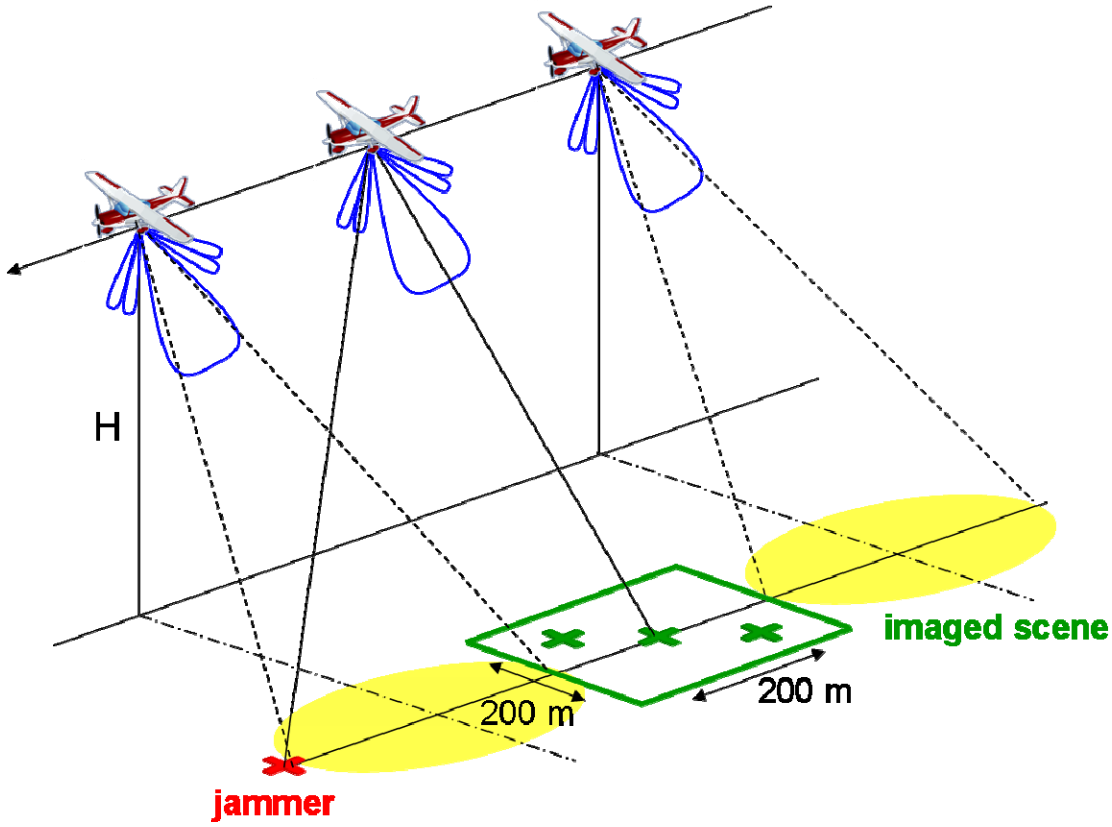

Figure III-20 Simulated SAR image: airborne scenario

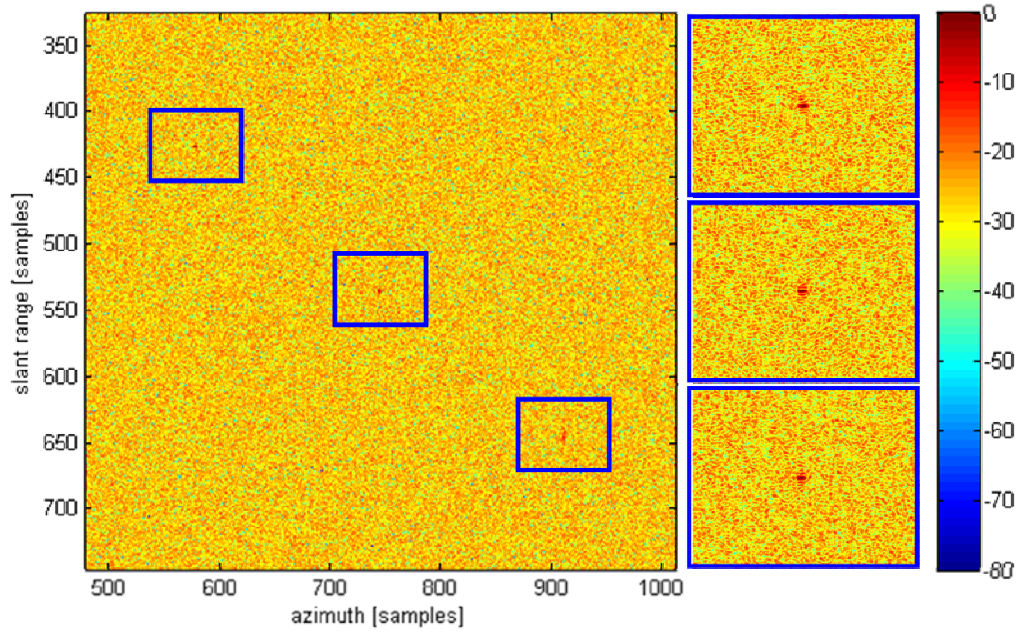

Figure III-21 Focused image (dB) for airborne-LT scenario: only thermal noise, no ECCM

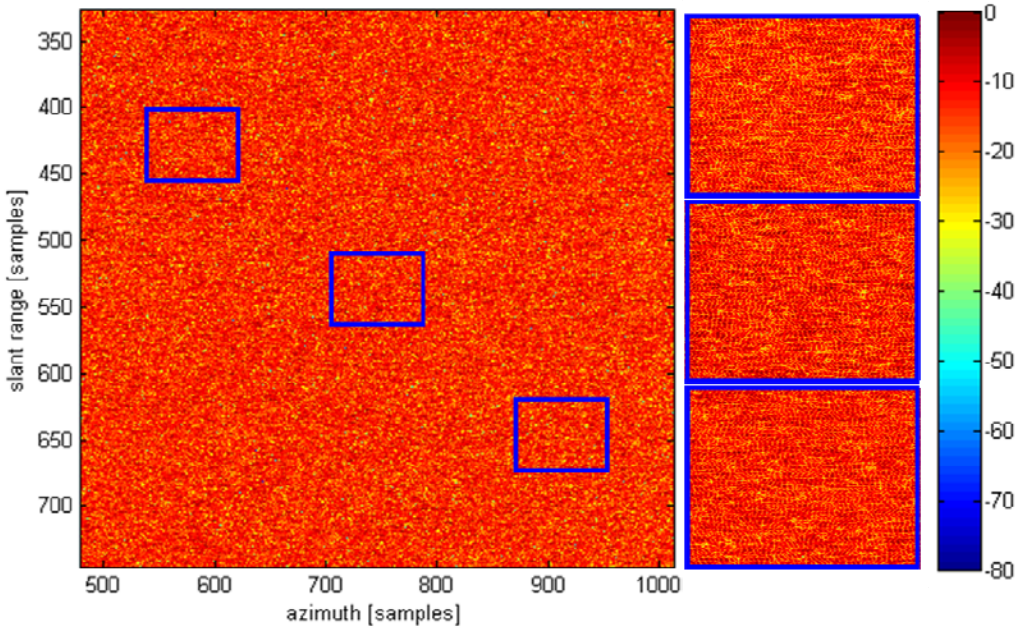

Figure III-22 Focused image (dB) for airborne-LT scenario: noise + jammer, no ECCM

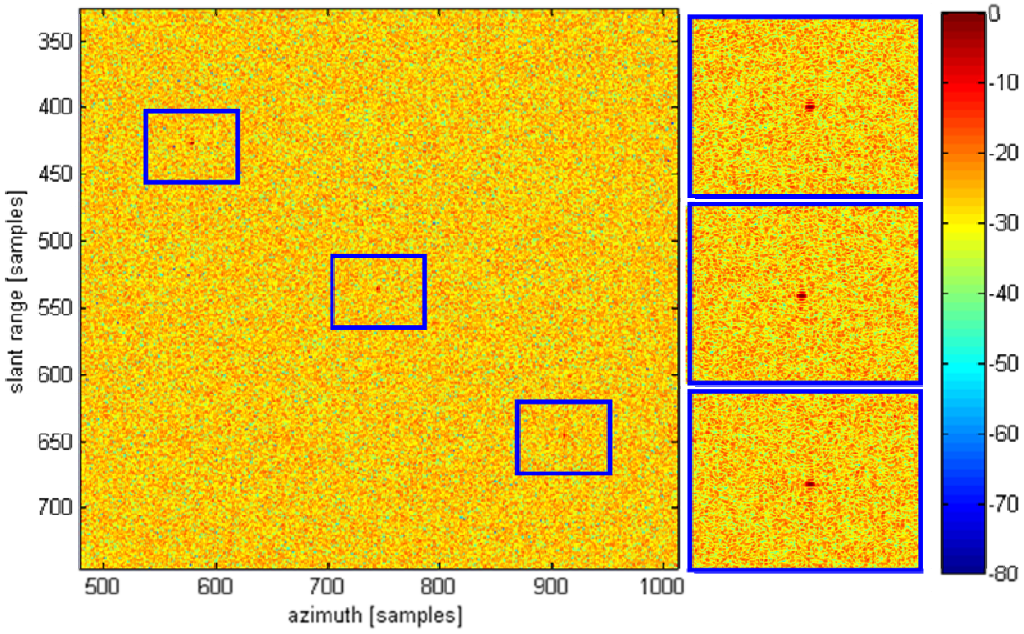

Figure III-23 Focused image (dB) for airborne-LT scenario: noise + jammer, ECCM applied

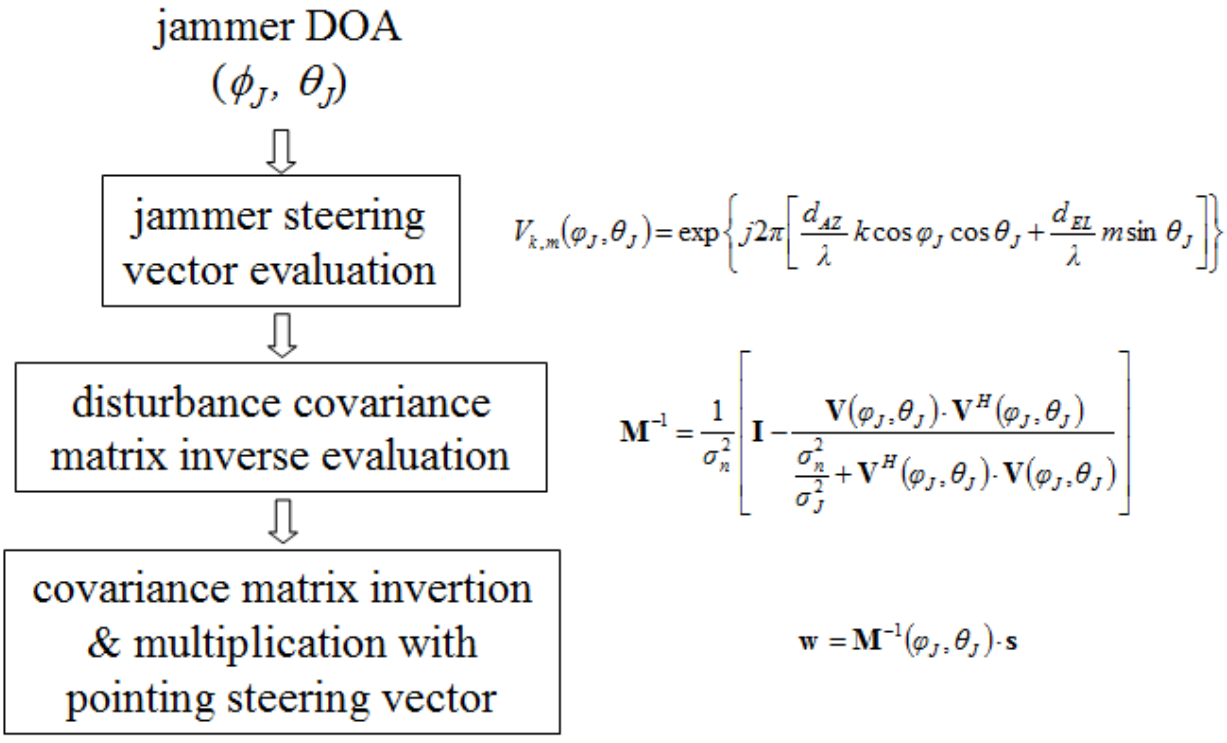

Figure III-24 Scheme for nulling weights evaluation with a priori jammer DOA knowledge

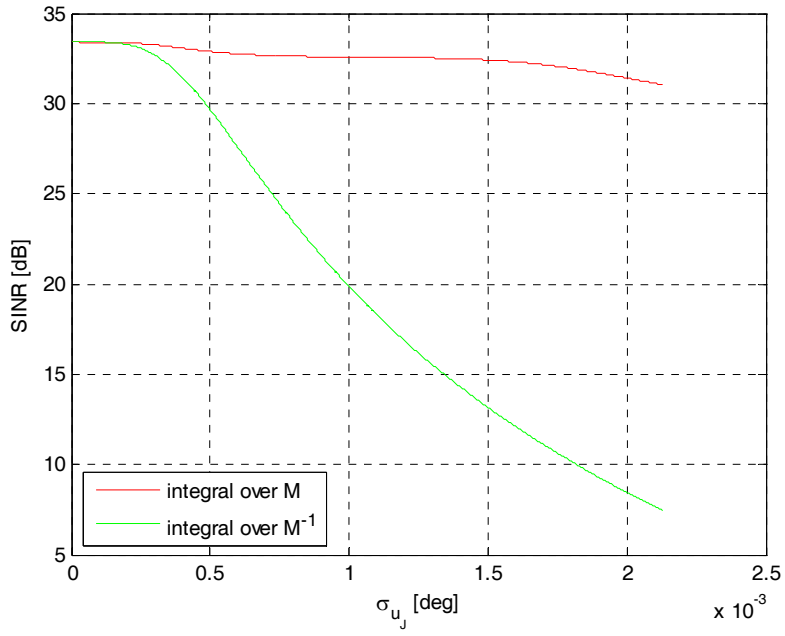

Figure III-25 SINR versus σ_{uJ} airborne-LT scenario: uniform error; 1st sidelobe jammer

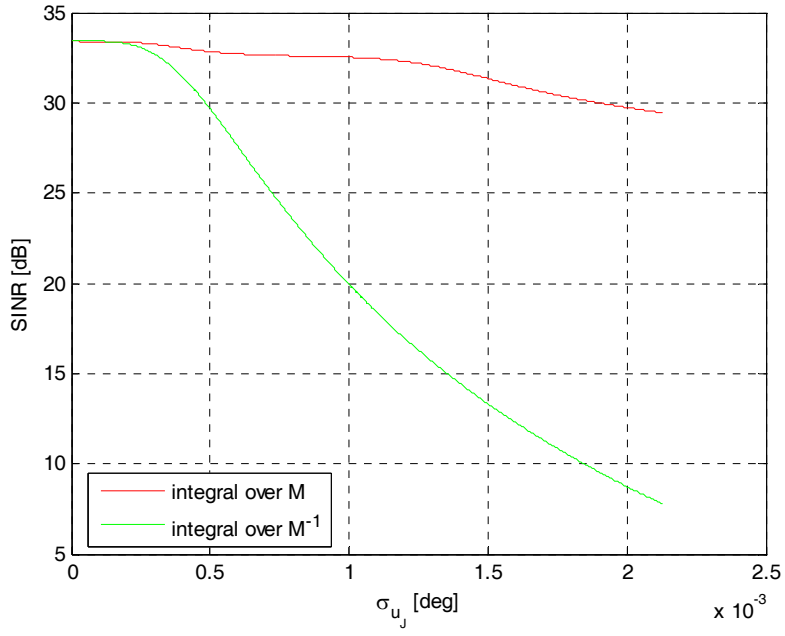

Figure III-26 SINR versus σ_{uJ} airborne-LT scenario: Gaussian error; 1st sidelobe jammer

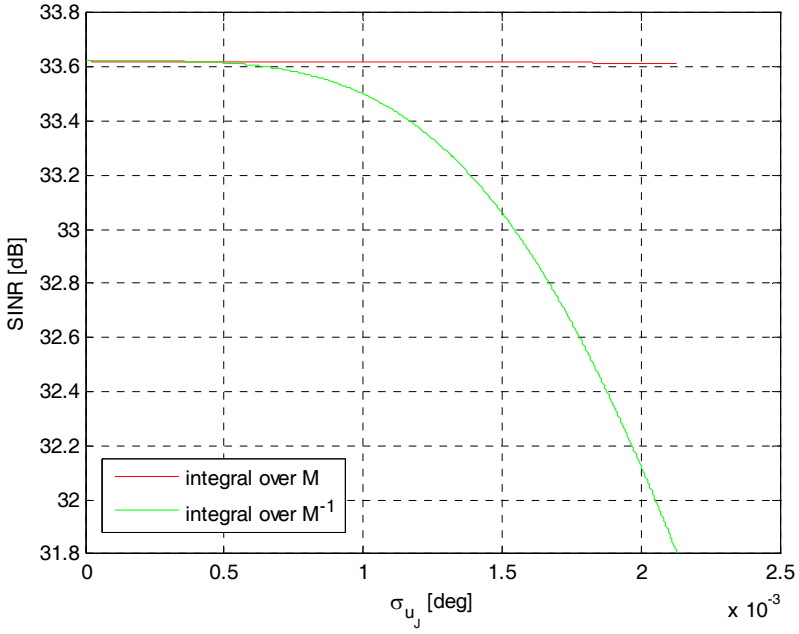

Figure III-27 SINR versus σ_{uJ} airborne-LT scenario: uniform error; 20th sidelobe jammer

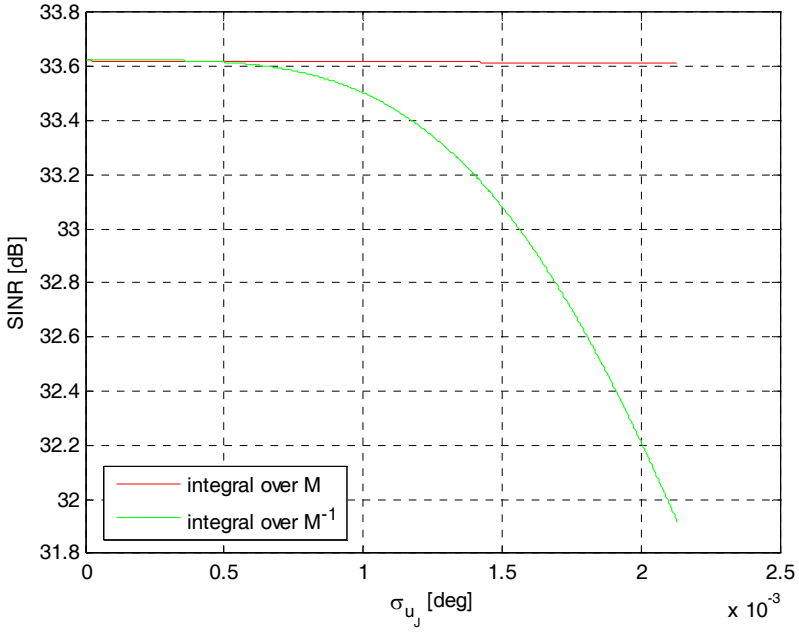

Figure III-28 SINR versus σ_{uJ} airborne-LT scenario: Gaussian error; 20th sidelobe jammer

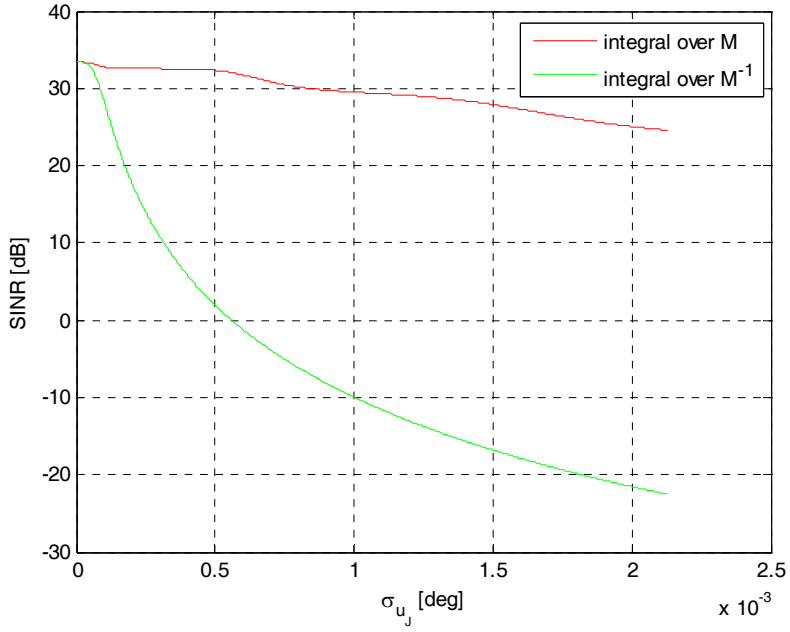

Figure III-29 SINR versus σ_{uJ} airborne-HT scenario: uniform error; 1st sidelobe jammer

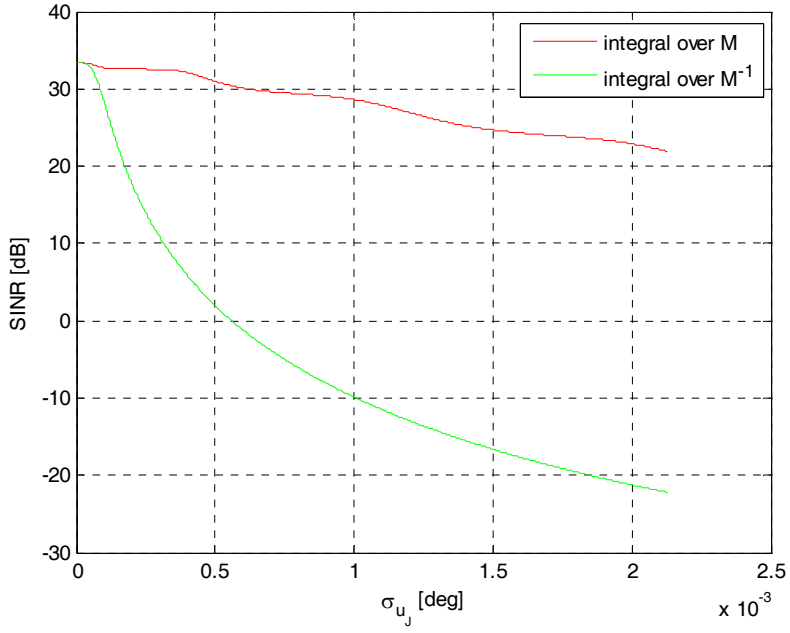

Figure III-30 SINR versus σ_{uJ} airborne-HT scenario: Gaussian error; 1st sidelobe jammer

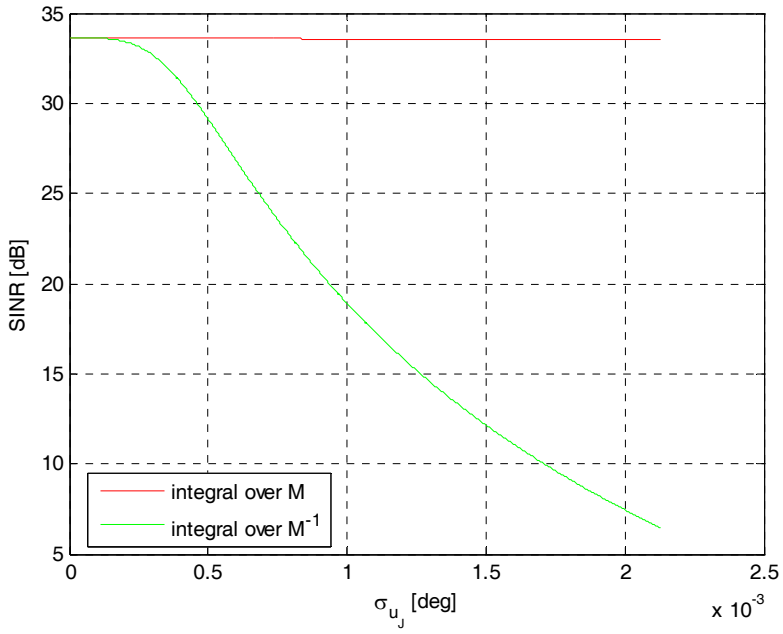

Figure III-31 SINR versus σ_{uJ} airborne-HT scenario: uniform error; 20th sidelobe jammer

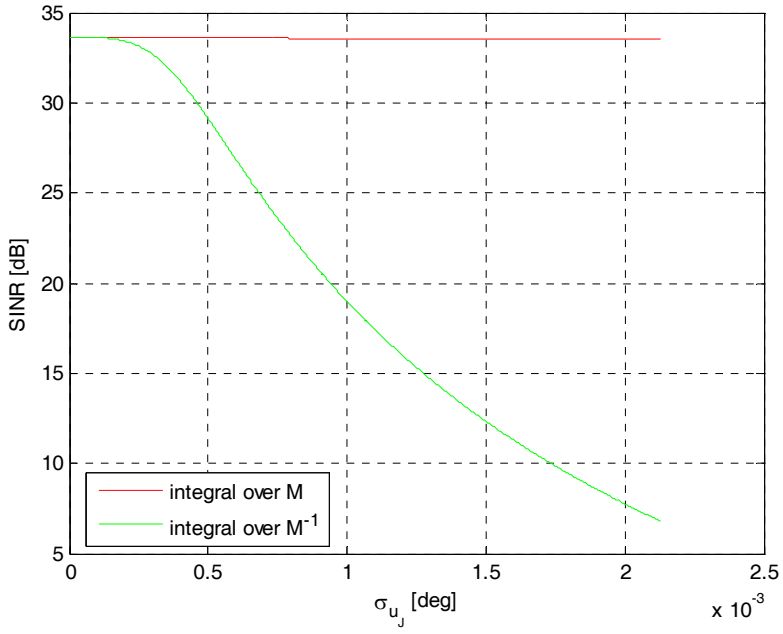

Figure III-32 SINR versus σ_{uJ} airborne-HT scenario: Gaussian error; 20th sidelobe jammer

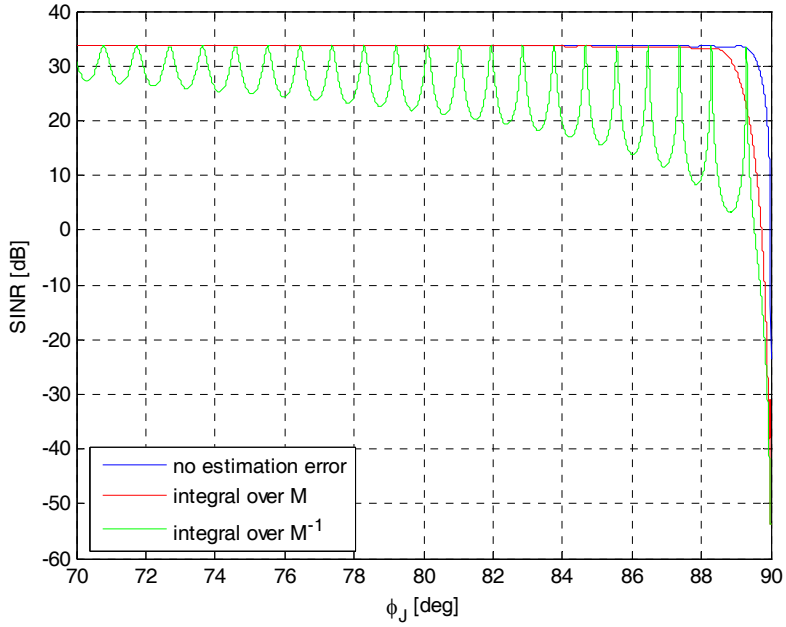

Figure III-33 SINR versus ϕ_J airborne-HT scenario: "fine estimation" case; uniform error

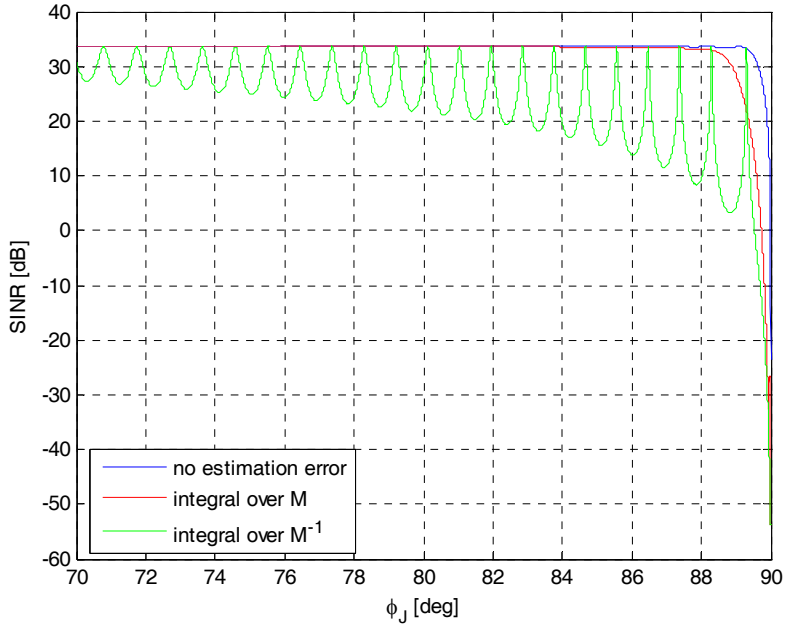

Figure III-34 SINR versus ϕ_J airborne-HT scenario: "fine estimation" case; Gaussian error

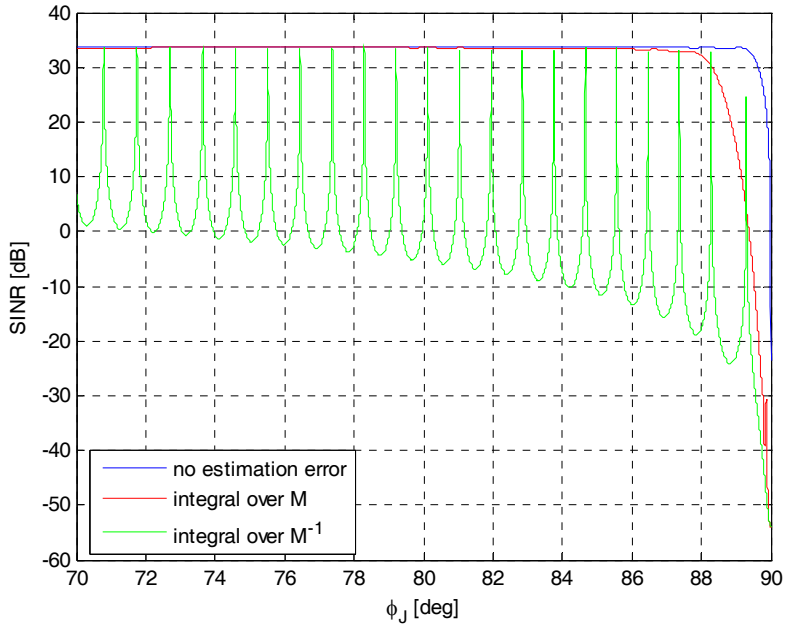

Figure III-35 SINR vs ϕ_J airborne-HT scenario: "coarse estimation" case; uniform error

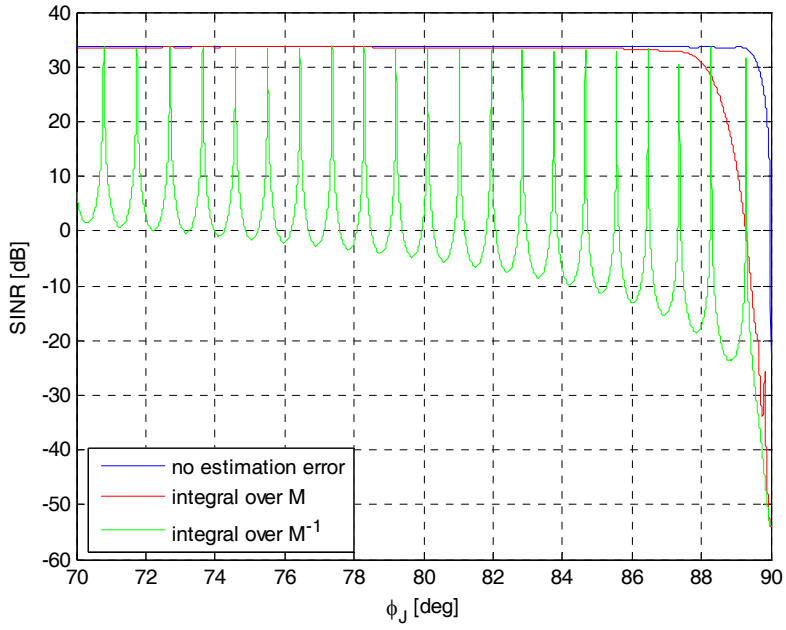

Figure III-36 SINR vs ϕ_J airborne-HT scenario: "coarse estimation" case; Gaussian error

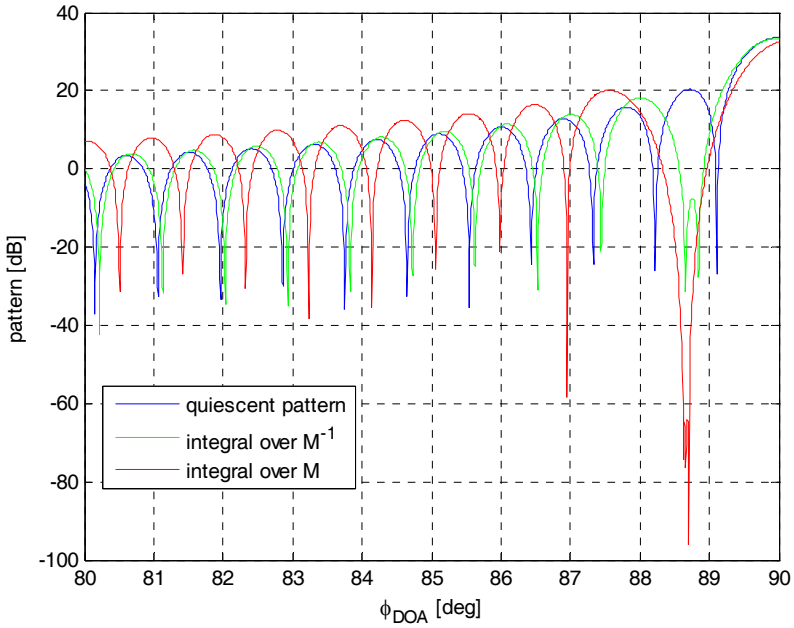

Figure III-37 Adapted patterns in airborne-HT scenario 1st sidelobe jammer: "fine estimation" case; uniform error

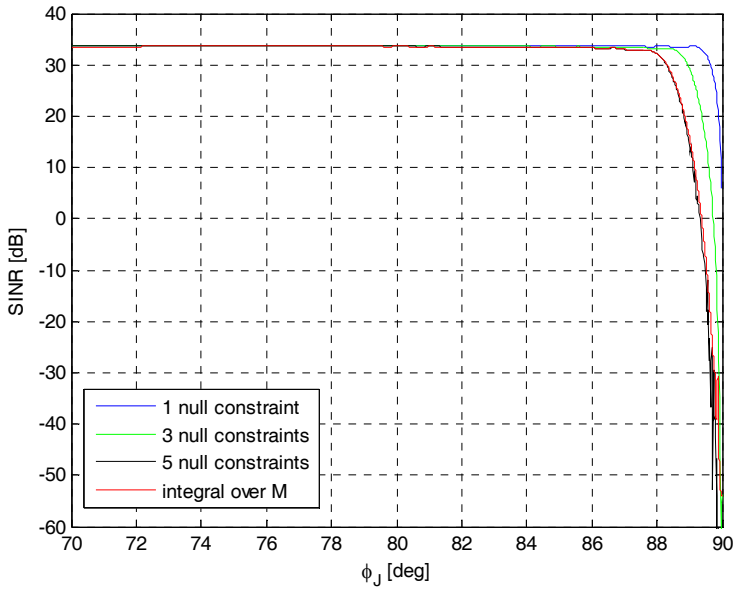

Figure III-38 SINR vs ϕ_J airborne-HT scenario: comparison between "null constraints" and "integral over M" strategies

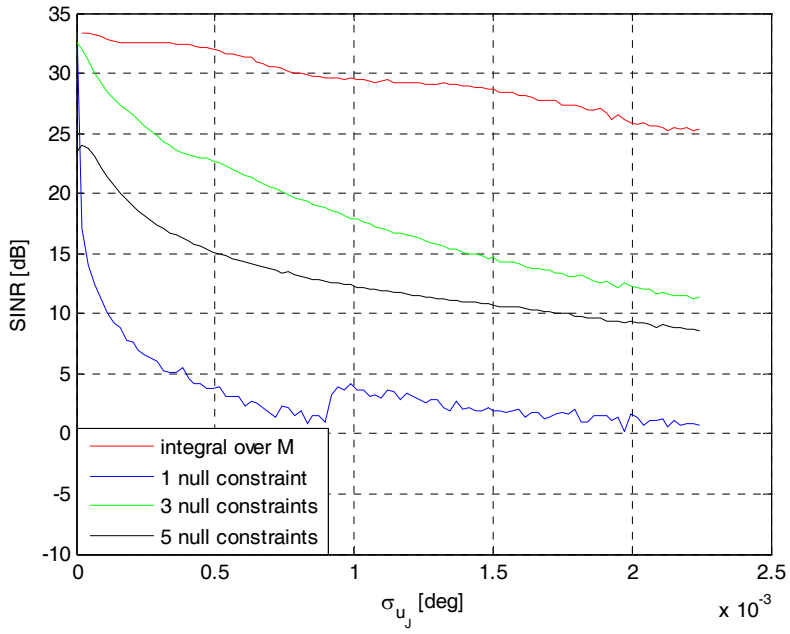

Figure III-39 SINR vs σ_{uJ} airborne-HT: "null constraints" (Monte Carlo simulation)

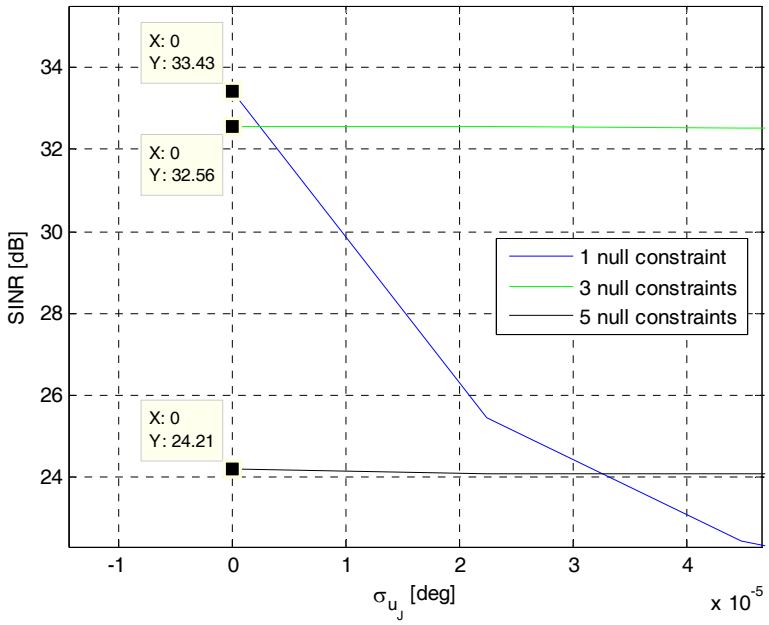

Figure III-40 SINR vs σ_{uJ} airborne-HT: "null constraints" (Monte Carlo simulation) - zoom

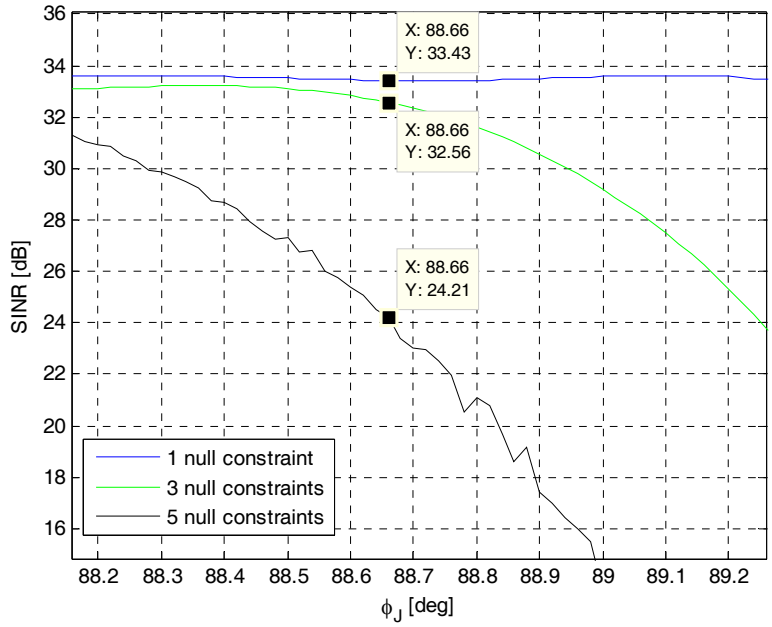

Figure III-41 SINR vs ϕ_J airborne-HT: "null constraints" - 1st azimuth sidelobe zoom

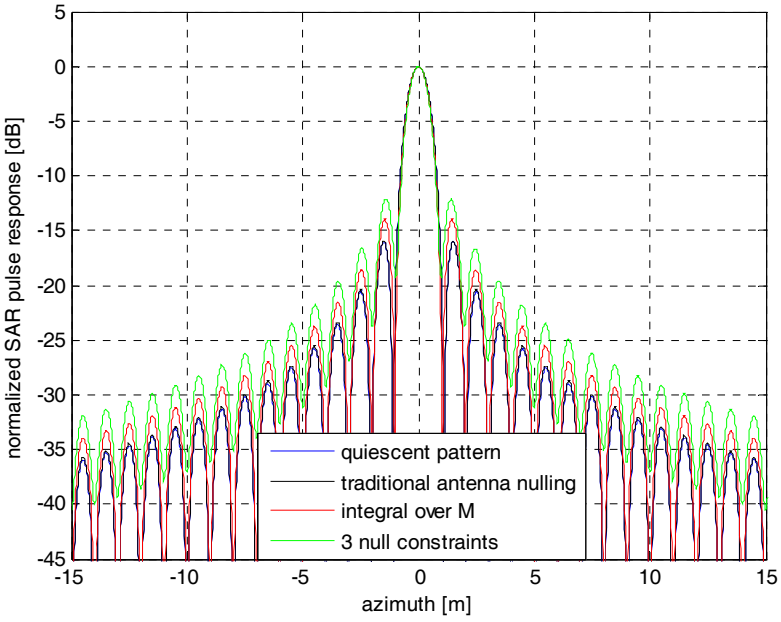

Figure III-42 SAR azimuth pulse responses in airborne-HT: 1st azimuth sidelobe jammer

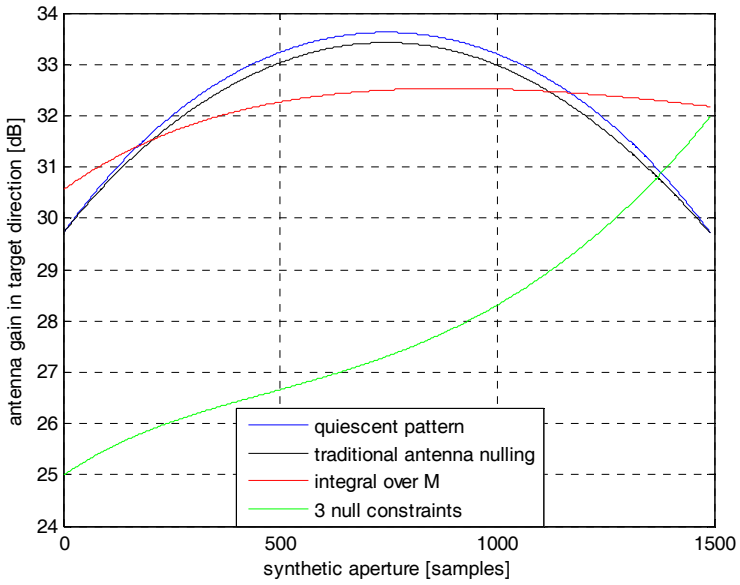

Figure III-43 Antenna gains in target DOA during synthetic aperture: airborne-HT 1st azimuth sidelobe jammer

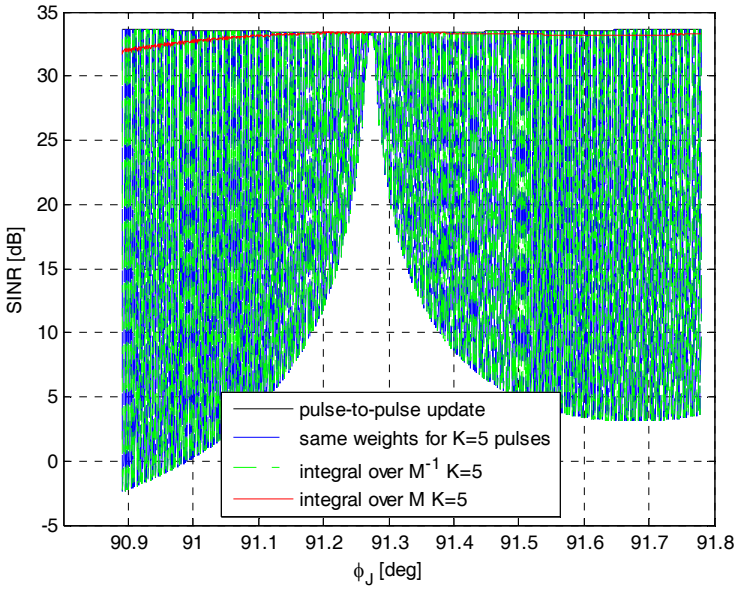

Figure III-44 SINR vs ϕ_J airborne-HT scenario: weights update K=5; σ_{φ_J} =0

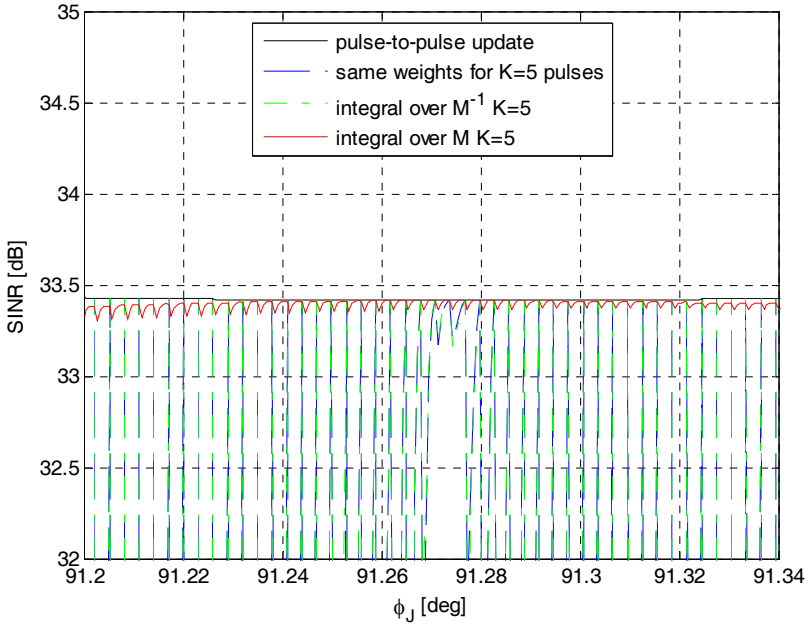

Figure III-45 SINR vs ϕ_J airborne-HT scenario: weights update K=5; σ_{φ_J} =0 - zoom

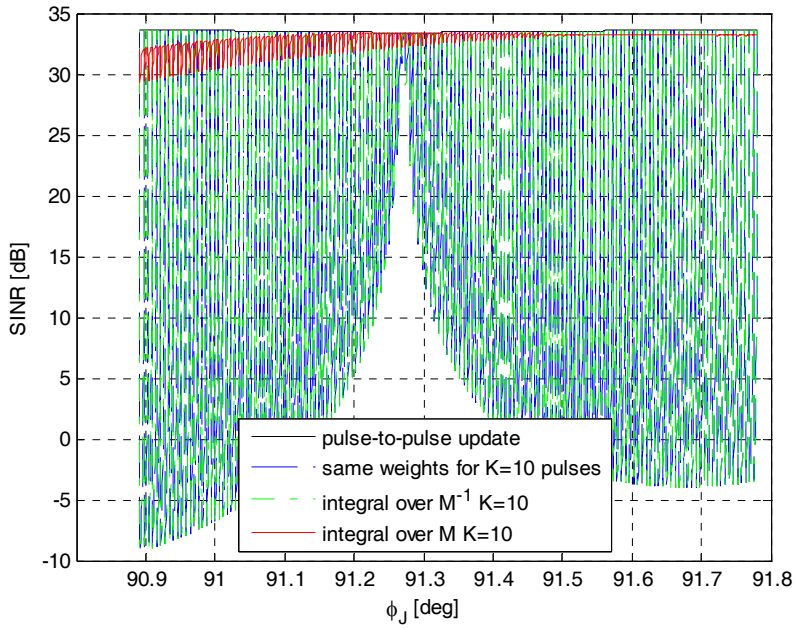

Figure III-46 SINR vs ϕ_J airborne-HT scenario: weights update K=10; σ_{φ_J} =0

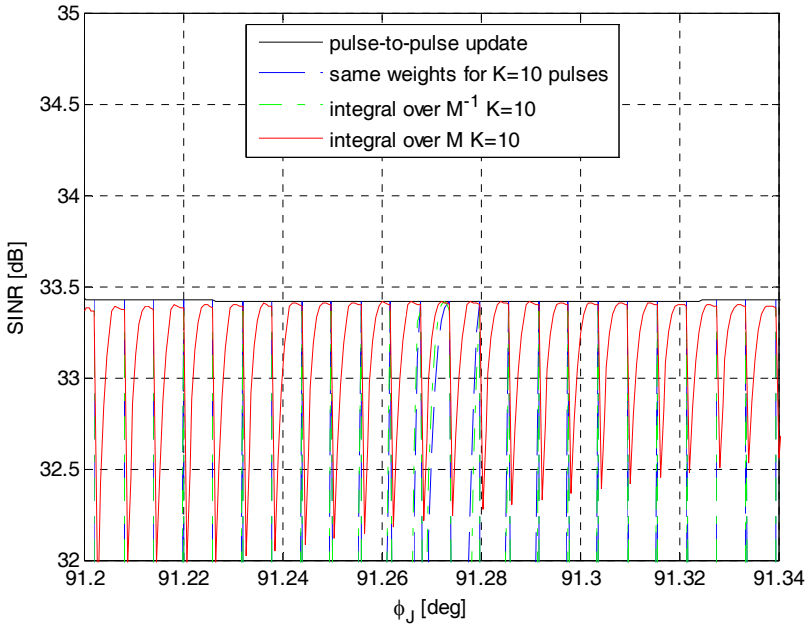

Figure III-47 SINR vs ϕ_J airborne-HT scenario: weights update K=10; σ_{φ_J} =0 - zoom

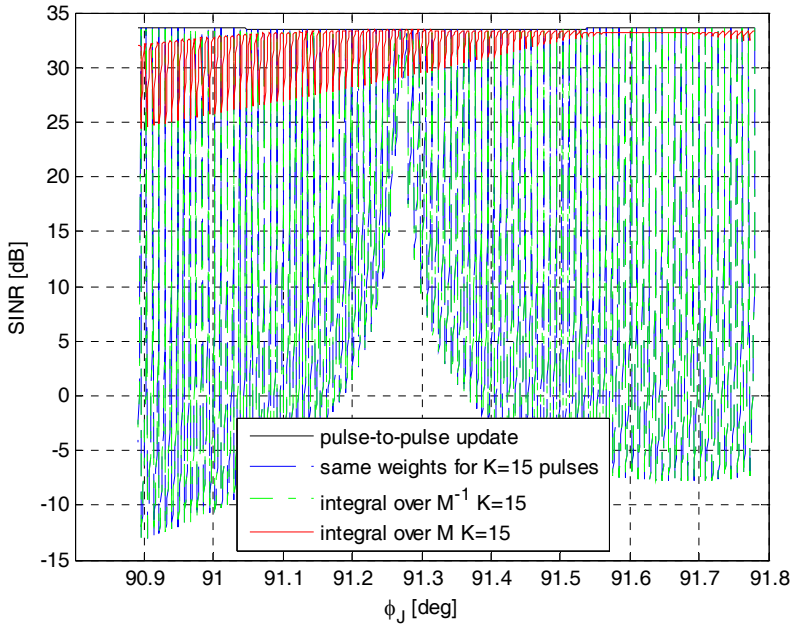

Figure III-48 SINR vs ϕ_J airborne-HT scenario: weights update K=15; σ_{φ_J} =0

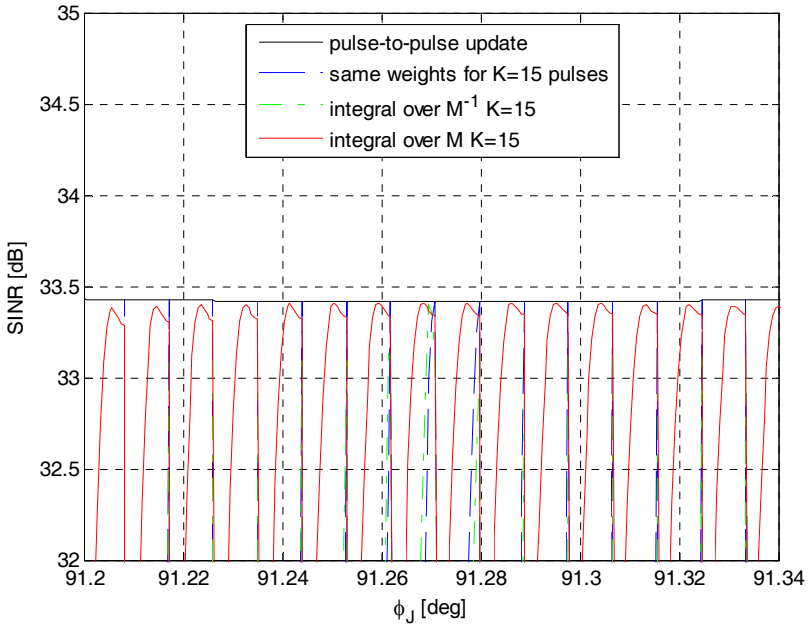

Figure III-49 SINR vs ϕ_J airborne-HT scenario: weights update K=15; σ_{φ_J} =0 - zoom

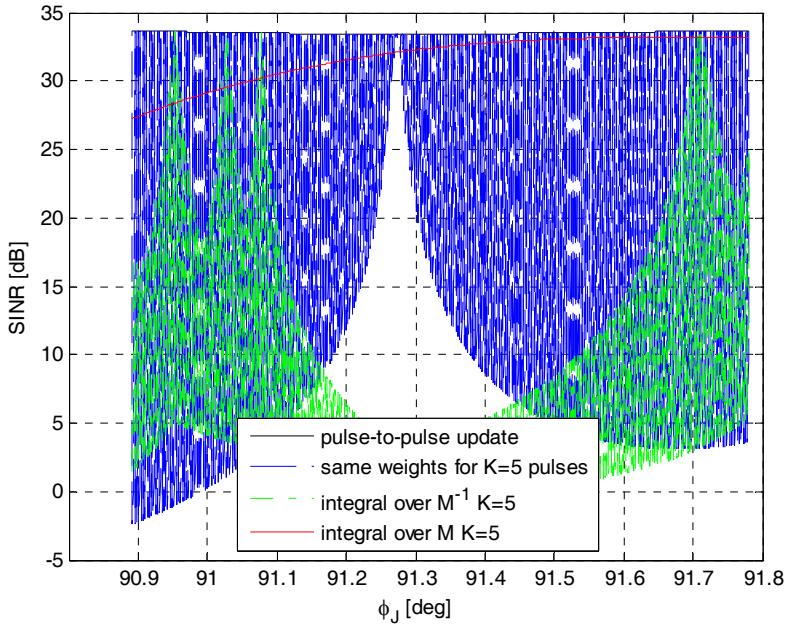

Figure III-50 SINR vs ϕ_J airborne-HT scenario: weights update K=5; $\sigma_{\varphi_J} = (1/10)\Delta\phi_{4dB}$

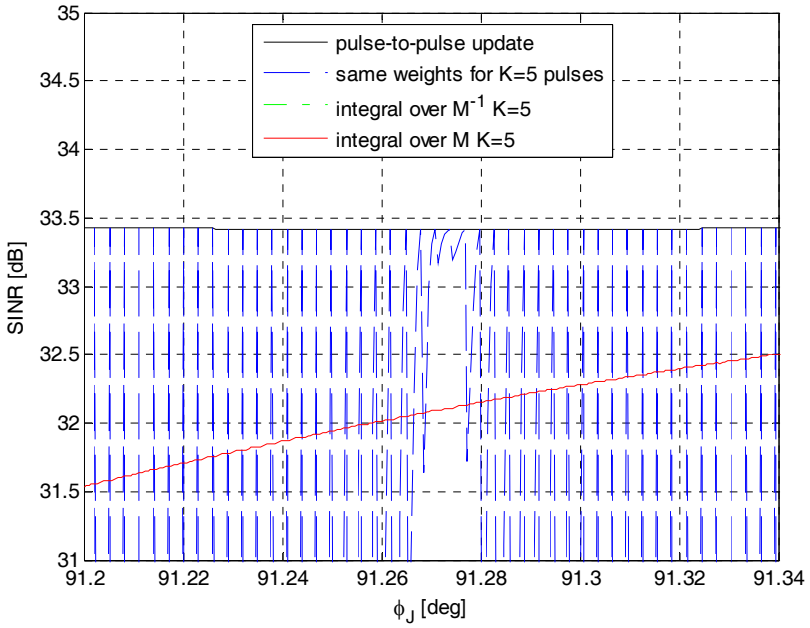

Figure III-51 SINR vs ϕ_J airborne-HT scenario: weights update K=5; $\sigma_{\varphi_J} = (1/10)\Delta\phi_{4dB}$ - zoom

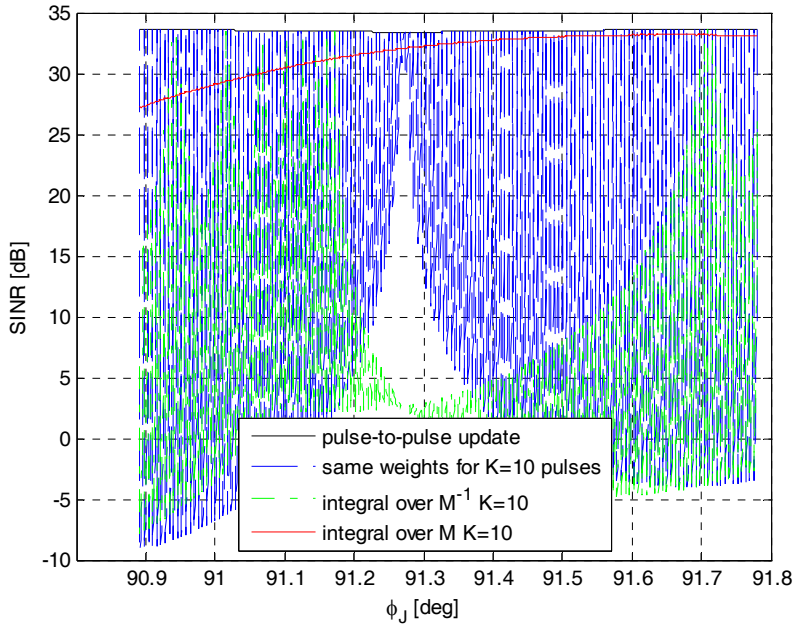

Figure III-52 SINR vs ϕ_J airborne-HT scenario: weights update K=10; $\sigma_{\varphi_J} = (1/10)\Delta\phi_{4dB}$

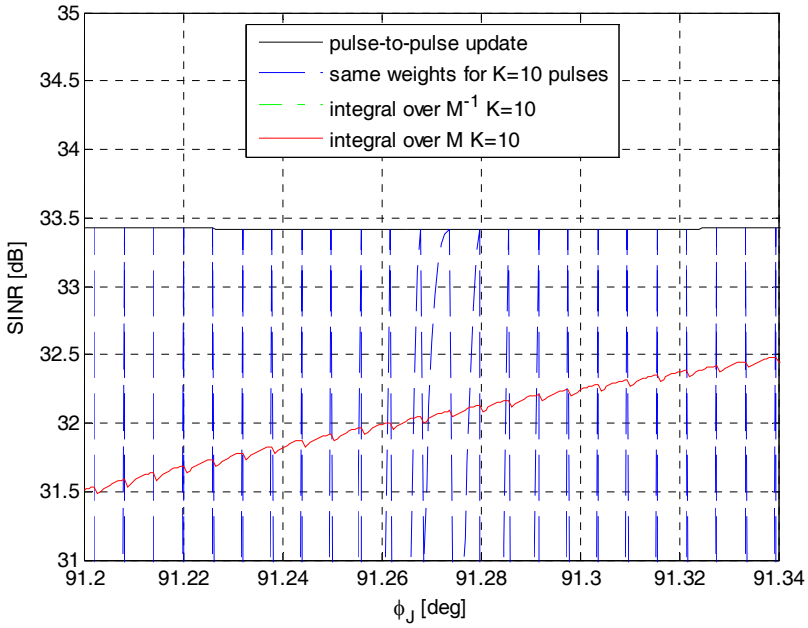

Figure III-53 SINR vs ϕ_J airborne-HT scenario: weights update K=10; $\sigma_{\varphi_J} = (1/10)\Delta\phi_{4dB}$ - zoom

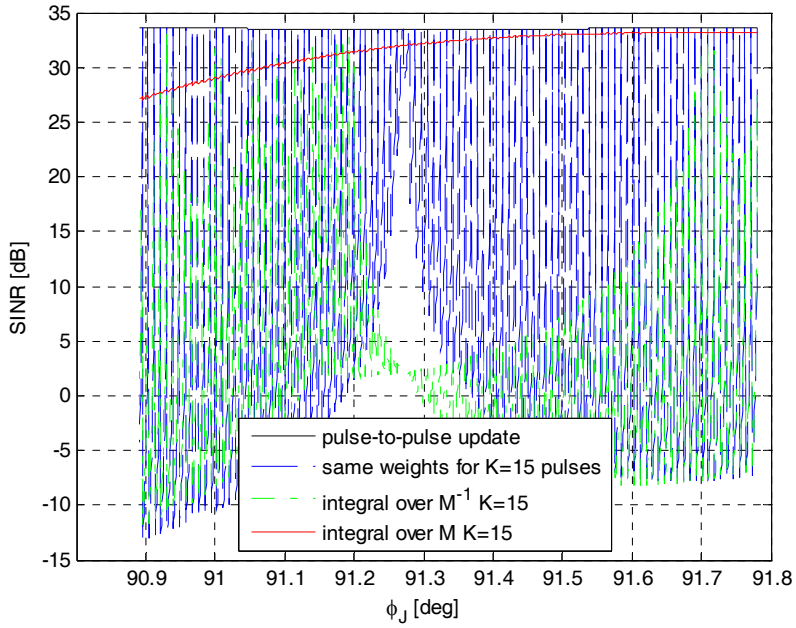

Figure III-54 SINR vs ϕ_J airborne-HT scenario: weights update K=15; $\sigma_{\varphi_J} = (1/10)\Delta\phi_{4dB}$

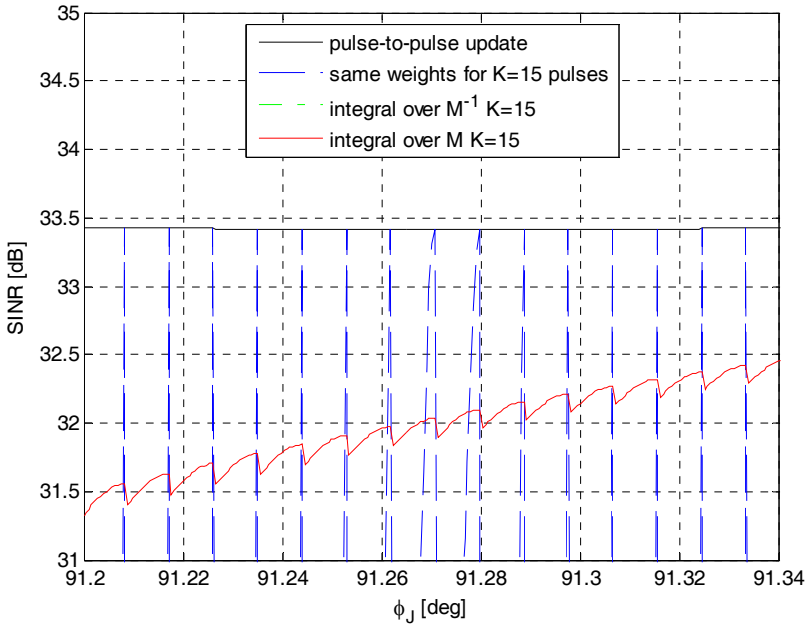

Figure III-55 SINR vs ϕ_J airborne-HT scenario: weights update K=15; $\sigma_{\varphi_J} = (1/10)\Delta\phi_{4dB}$ - zoom

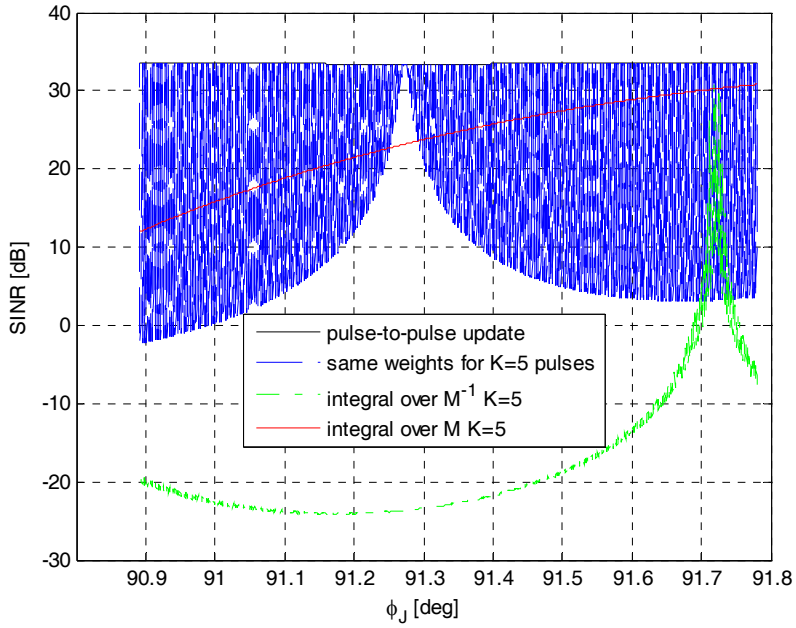

Figure III-56 SINR vs ϕ_J airborne-HT scenario: weights update K=5; $\sigma_{\varphi_J} = (1/2)\Delta\phi_{4dB}$

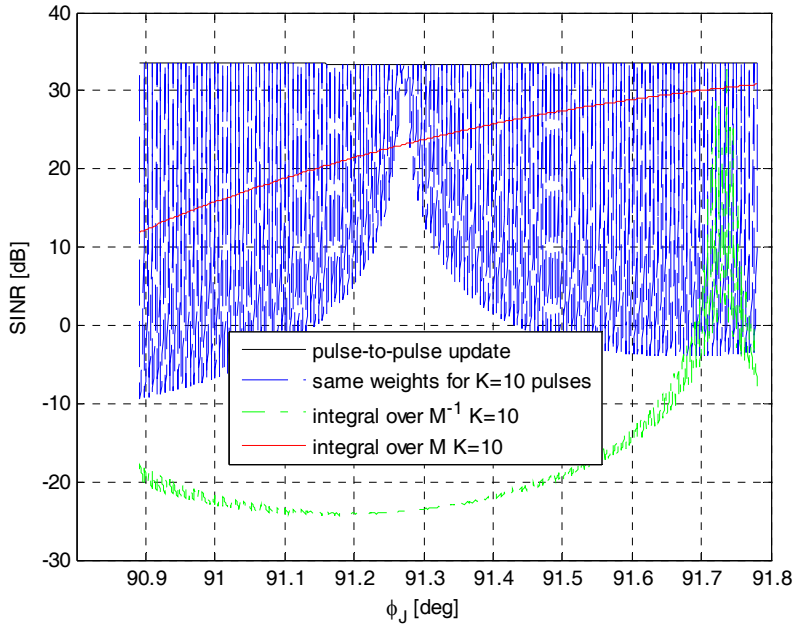

Figure III-57 SINR vs ϕ_J airborne-HT scenario: weights update K=10; $\sigma_{\varphi_J} = (1/2)\Delta\phi_{4dB}$

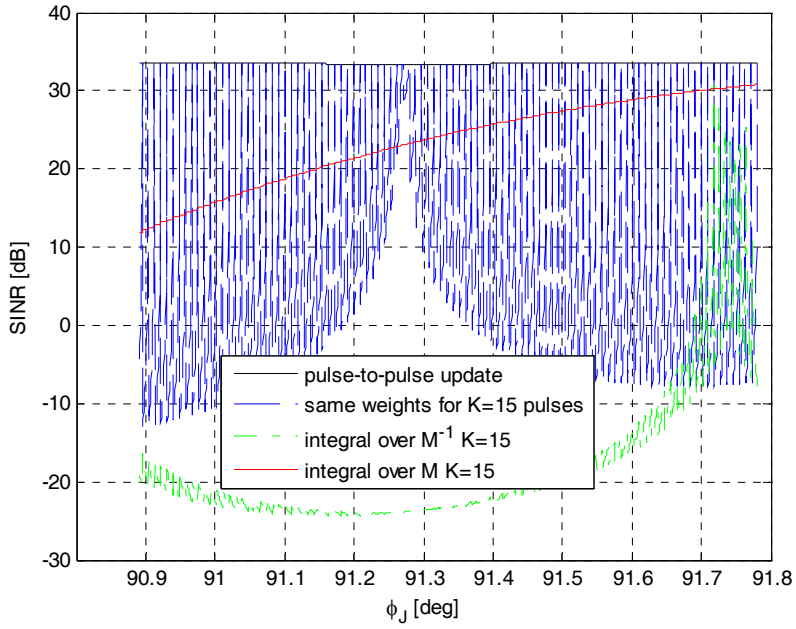

Figure III-58 SINR vs ϕ_J airborne-HT scenario: weights update K=15; $\sigma_{\varphi_J} = (1/2)\Delta\phi_{4dB}$

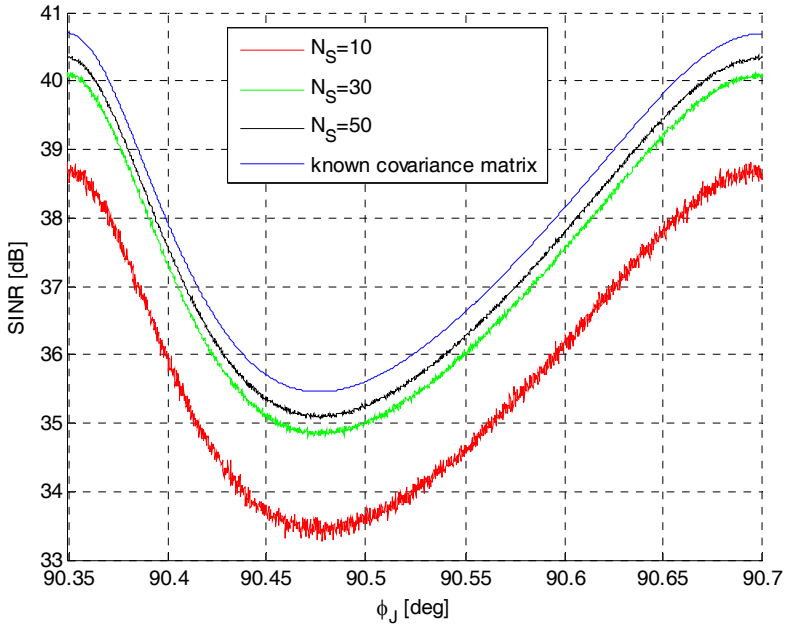

Figure III-59 SINR vs ϕ_J spaceborne-HT: adaptivity losses in covariance matrix estimation

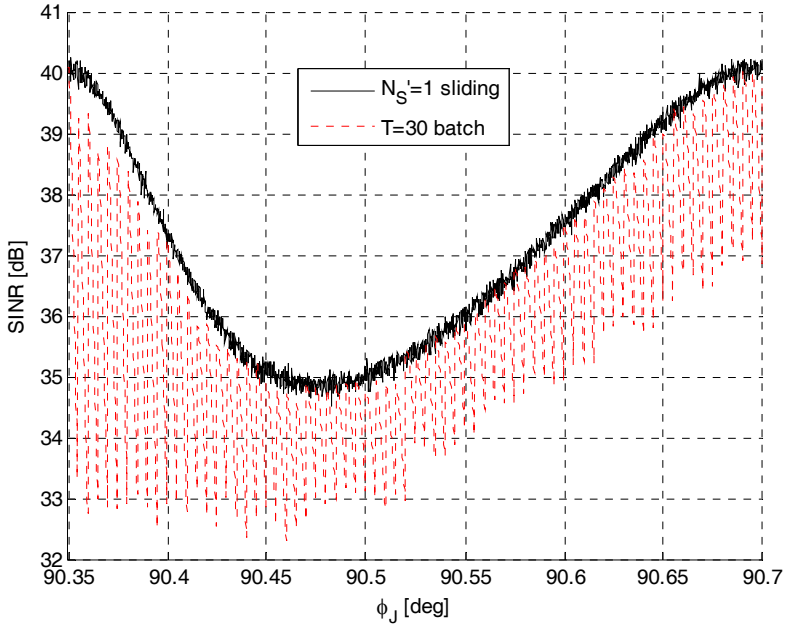

Figure III-60 SINR vs ϕ_J spaceborne-HT scenario: sliding and batch approaches with N_S'=1

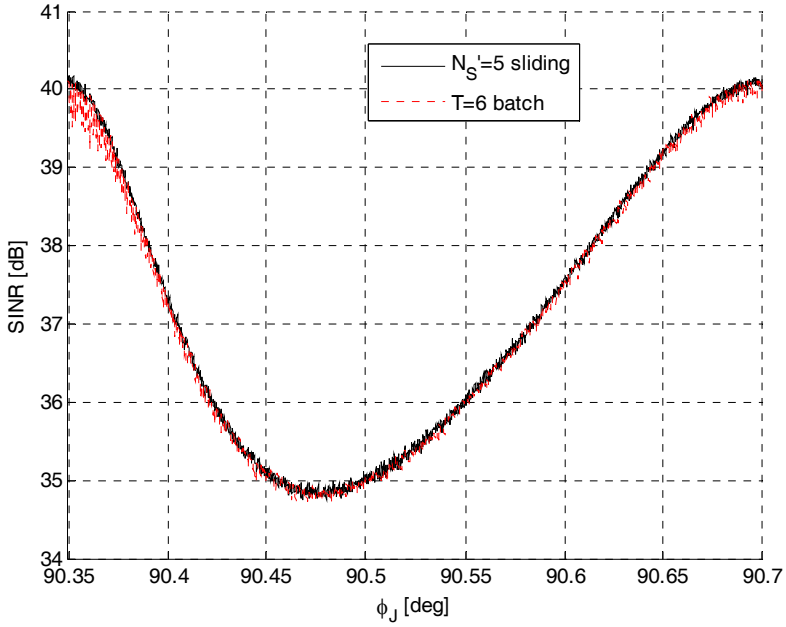

Figure III-61 SINR vs ϕ_J spaceborne-HT scenario: sliding and batch approaches with N_S'=5

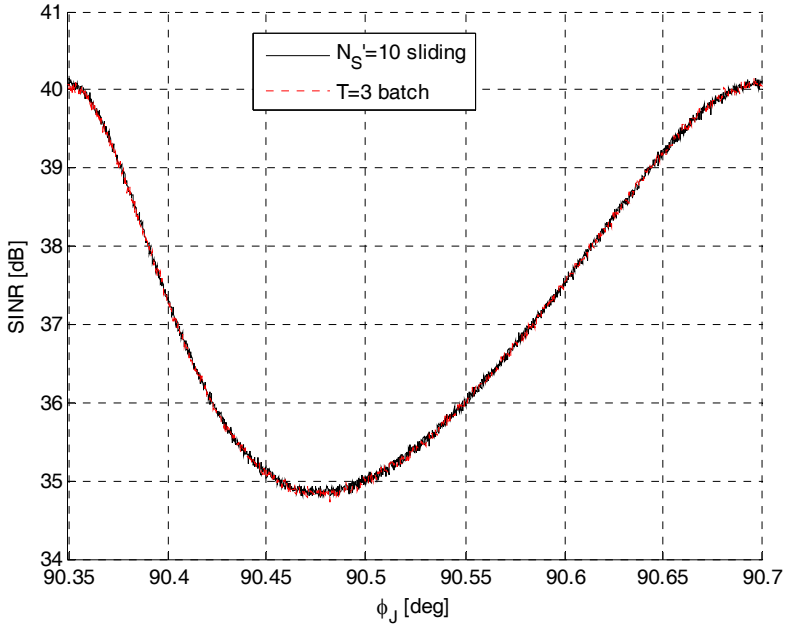

Figure III-62 SINR vs ϕ_J spaceborne-HT: sliding and batch approaches with N_S'=10

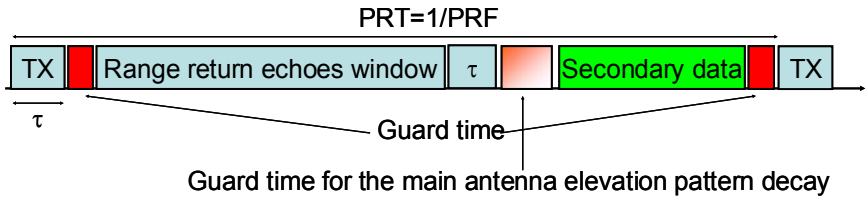

Figure III-63 Timing Diagram

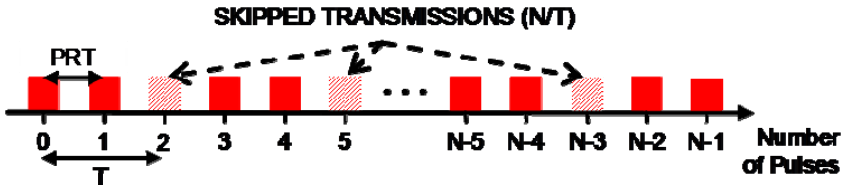

Figure III-64 Periodic skip of transmissions

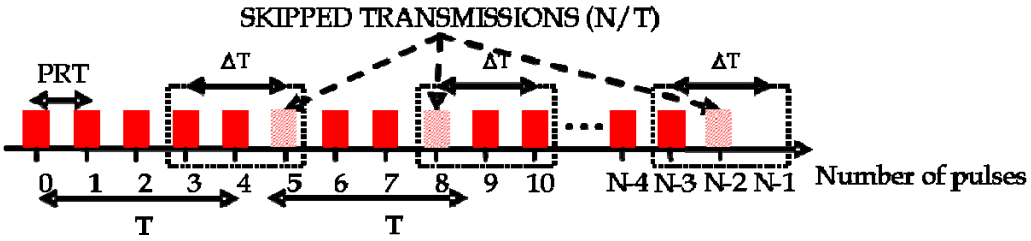

Figure III-65 Periodic skip of transmissions with pseudorandom shift

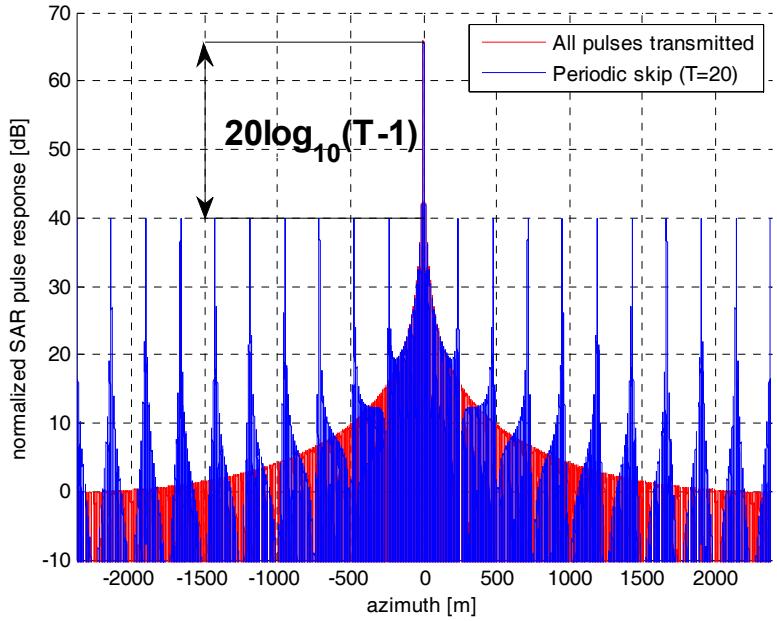

Figure III-66 SAR pulse response: approach (i), T=20

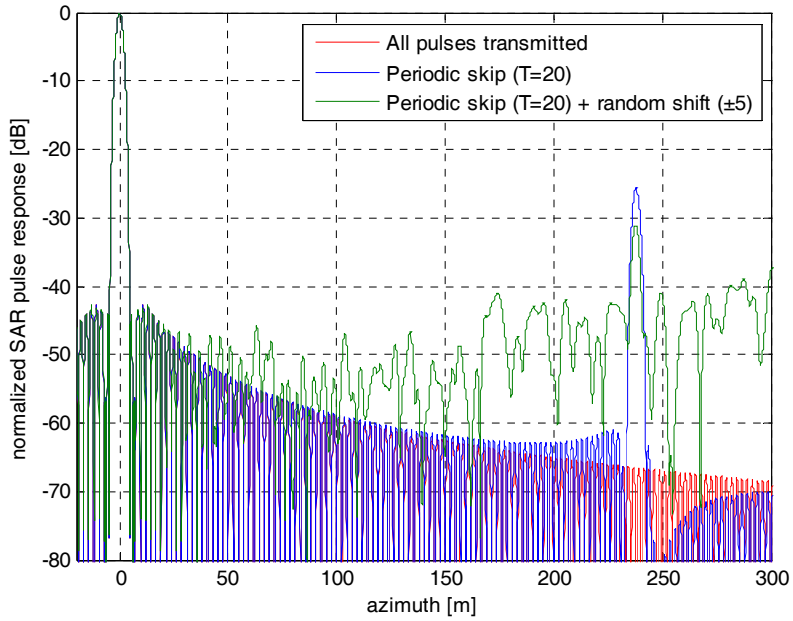

Figure III-67 Normalized tapered SAR impulse response: comparison between approaches (i) and (ii), T=20 and ΔT=±5

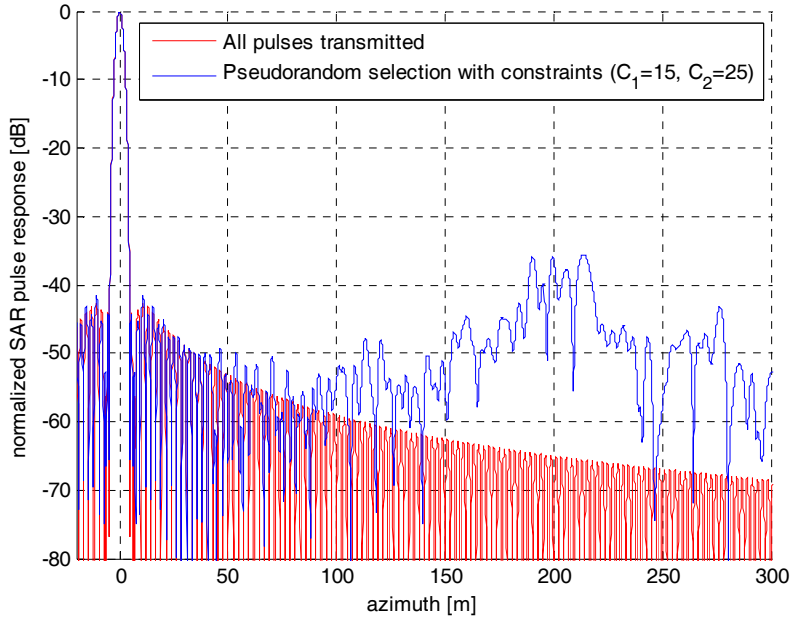

Figure III-68 Normalized tapered SAR response: approach (iii), p_0= 0.05, C_1=15, C_2=25

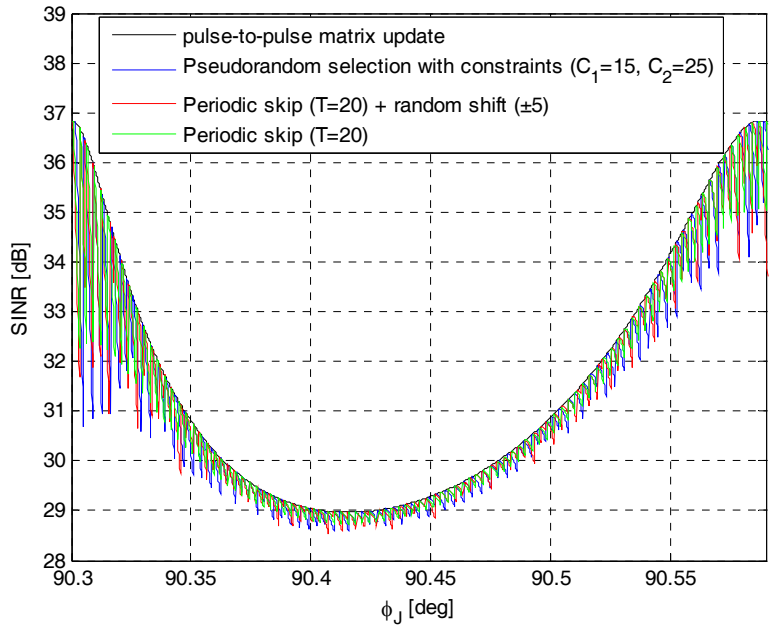

Figure III-69 Update frequency impact on system cancellation capability: near sidelobe region

III.9 *Tables*

Orbit height	700 km
Platform velocity	7500 m/s
Transmitted power	4 kW
System noise figure	2 dB
Carrier frequency	9.6 GHz
PRF	3000 Hz
Incidence angle	30° ÷ 50°
Nominal resolution (azimuth × ground range)	3 m × 3 m
Antenna dimension (azimuth × elevation)	6 m × 2 m
Element spacing (azimuth × elevation)	$0.67 \cdot \lambda \times 0.6 \cdot \lambda$

Tab. III-1 Spaceborne scenario: main system parameters

Orbit height	10 km
Platform velocity	120 m/s
Transmitted power	1 kW
System noise figure	2 dB
Carrier frequency	9.6 GHz
PRF	200 Hz
Grazing angle	5° ÷ 20°
Nominal resolution (azimuth × ground range)	1 m × 1 m
Antenna dimension (azimuth × elevation)	2 m × 0.5 m
Element spacing (azimuth × elevation)	$0.67 \cdot \lambda \times 0.67 \cdot \lambda$

Tab. III-2 Airborne scenario: main system parameters

	Low-Tech	**High-Tech**
EIRP	40 dBW	70 dBW
Jammer incidence angle: spaceborne scenario airborne scenario	40° 80°	

Tab. III-3 Jammer parameters

Pulse length	10 μs
Resolution (azimuth & range)	1 m
Grazing angle at scene center	10°
Platform height	10 km
PRF	200 Hz
Target Radar Cross Section	5 dB

Tab. III-4 Main system parameters used for simulated SAR image: airborne-LT scenario

Scenario / nulling technique	**measured SINR [dB]**
thermal noise only / no ECCM	25.46
noise + jammer / no ECCM	4.61
noise + jammer / ECCM	25.75

Tab. III-5 Measured SINRs from simulated SAR image in the airborne-LT scenario

T	Peak Loss (dB)	PPER (dB)
10	0,92	19,08
15	0,60	22,92
50	0,18	33,80
100	0,09	39,91

Tab. III-6 Peak loss and PPER for approach (i)

Shift	PPER (dB)
T	22.92
T±1	23.11
T±2	24.17
T±3	26.11
T±4	29.23
T±5	32.94

Tab. III-7 PPER achievable using approach (ii)

C_1	C_2	PPER (dB)	Skipped pulses
13	17	30.63	87
12	18	31.79	85
11	19	33.07	87
10	20	34.02	85

Tab. III-8 PPER achievable using approach (iii)

	Approach	ISLR (dB)	Skipped pulses
No Tapering	All pulses transmitted	-9.68	0
Hamming Tapering	All pulses transmitted	-34.36	0
	(i) T = 15	-11.44	100
	(ii) T = 15, shift = ±5	-11.44	100
	(iii) C_1=10, C_2=20	-12.12	85

Tab. III-9 ISLR using approaches (i), (ii) and (iii)

IV MULTI-CHANNEL SAR FOR CLUTTER CANCELLATION

IV.1 *Introduction*

The recent performance improvements of SAR systems in terms of spatial resolution, make particularly interesting the possibility to detect and image even small moving targets within SAR images. The detection of small moving objects inside a SAR image is a very challenging application due to the possible low Radar Cross Section (RCS) of the targets and to the possible low Doppler frequencies of the movers, due to their slow motion. Another aspect to be considered resides in the ill-positioning of moving targets inside SAR images, which is directly related to the intrisic ambiguity between Doppler frequency and azimuthal angle of view in single-channel SAR systems.

To overcome these problems, thus implementing a SAR-GMTI (Ground Moving Target Indication) capability, several approaches are possible, each one having a different impact on the SAR system design.

The simplest approach is to perform the moving target detection working in the Doppler domain only, synthesizing a filter with a zero-Doppler notch, so that returns from the stationary background can be cancelled. This approach has the appealing advantage to be suitable even for a single-channel SAR system. The main drawback is that only exo-clutter moving targets can be detected, that is only targets fast enough to produce echoes with Doppler frequencies out of the clutter Doppler bandwidth.

Another very low-cost approach is to divide the overall synthetic aperture in several sub-apertures, focus each sub-aperture independentely at reduced azimuth resolution, and detect moving targets as "changes" in the sequence of low-resolution SAR images, [47]. Even in this case, while a simple single-channel SAR systems allows some SAR-GMTI capabilities, low RCS and/or slow moving targets are hardly detected against the strong background.

Among a wide variety of other SAR-GMTI approaches, the most promising it is represented by the exploitation of multi-channel SAR systems. In this case, the availability of multiple parallel receiving channels gives additional Degrees Of Freedom (DOFs) to suppress returns from the stationary background (i.e. ground clutter), thus making easier the detection of movers. All multi-channel SAR-GMTI techniques which are based on an adaptive cancellation of the clutter echoes are also referred to as Space Time Adaptive Processing (STAP) techniques for SAR, [46] [48] [49]. In order to guarantee effective additional DOFs for clutter cancellation the parallel receiving channels have to allow different sampling of the echoes in the along-track direction. This pose some limitations to the relative spatial location of the different phase centers. A viable commonly used configuration foresees the parallel receiving channels to be connected to different antenna sub-apertures aligned in the along-track direction. Possible partitions of a phased array antenna similar to the one mounted in the SAR of COSMO-SkyMed are sketched in **Figure II-4**, **Figure II-5**, and in **Figure II-6**.

Space samples collected with multiple parallel receiving channels together with Time samples corresponding to different Pulse Repetition Intervals (PRI) are combined coherently with proper complex weights in a Space-Time filter that cancels the echo backscattered from the ground making visible the signals corresponding to moving targets. Such a two-dimensional filtering leads to much higher performance w.r.t. a one-dimensional filtering (either Space-only or Time-only filtering).

The optimum way to coherently combine Space-Time samples (i.e. the optimum derivation of the FIR filter weights) can be derived analytically, [46]. This optimum weights derivation ensures the

maximization of the Signal to Clutter plus Noise Ratio after filtering. In practical cases, some sub-optimal STAP configurations have been derived to limit the overall number of spatial and temporal DOFs, hence trying to keep limited the overall computational burden. Specifically, for the case of a M-SAR system, the overall number of temporal samples to be considered in the optimum filter synthesis is equal to the overall slow-time samples corresponding to a synthetic aperture, which can be even of the order of some thousands[10]. Among this huge amount of temporal samples, only a very limited number result effectively correlated each other, thus being useful for clutter cancellation. Different sub-optimal schemes have been proposed (see for example [51]), aiming at limiting the number of temporal samples by keeping only those correlated each other.

A very interesting STAP implementation suitable for the M-SAR case has been introduced in [49]. In this case an azimuth Fourier Tansform is performed independently for each parallel receiving channel prior than STAP filtering. This post-Doppler approach to STAP guarantees, for the SAR case, a theoretical decoupling of different Doppler bins and a clutter sub-space dimension equal to 1. As a consequence, a clutter cancellation can be performed separately for each Doppler bin using only the spatial DOFs (which are usually a limited number in a M-SAR system). This results in small dimensions of the covariance matrices to be estimated and inverted, thus maintaining limited the computational burden.

Apart from the clutter cancellation that is mandatory to allow proper moving target detection against strong background, if also high-resolution imaging of the moving target is required, the focusing algorithm has to be complicated to deal with target motion defects in SAR images. In fact, as it is well known, moving targets within SAR images appear shifted and/or smeared due to their motion [43]. In particular, an along-track target velocity component determines a variation in the resulting azimuth

[10] Actually, this number is highly depending on the SAR system considered and might range of two or three orders of magnitude.

chirp rate and a consequent mis-match with the parameters used to focus the stationary scene, thus giving rise to target smearing. These effects deteriorate the imaging capability of movers, as well as a reduction in the achievable Signal to Clutter plus Noise Ratio (SCNR).

In particular, a viable solution to recover the moving target imaging capability is to design a more complex focusing algorithm which takes into account a possible along-track movement of the targets, thus synthesizing several azimuth compression filters each one matched to a different relative along-track velocity between SAR sensor and moving target, as described in [44]. Since a high number of filters directly determines an increase in the computational cost, it is necessary to resort to a computational efficient focusing algorithm, like the Chirp Scaling Algorithm (CSA), [45]. It is worth noticing that such a bank of focusing filters is able to partially recover SCNR degradation due to focusing mis-match, thus increasing moving target detection capabilities even in a single-channel SAR system, [52]. However, this SCNR recovery is not enough is sub-clutter target visibility is required.

Therefore the two techniques for moving target detection and high-resolution imaging have to be jointly exploited in the framework of a M-SAR system, [50]. This chapter is organized as follows. In Section IV.2 the implementation of bank of focusing filters based on the CSA is presented. Performance evaluation is conducted with reference to an emulated single-channel SAR scenario in terms of both improved moving target detection and improved imaging capabilities. Section IV.3 presents an efficient integration of the bank of CSA together with the aforementioned post-Doppler STAP approach. The need of a joint application of STAP and bank of filters is demonstrated against an analogous emulated M-SAR datacube. In Section IV.4 the efficiency of the integrated STAP + bank of CSA technique is evaluated in terms of overall computational burden. A comparison with an Along-Track Interferometry (ATI)-based approach is reported.

IV.2 *Bank of focusing filters based on Chirp Scaling Algorithm*

As it is well known, SAR data focusing is based on the assumption of a stationary scene to be imaged, and it is only related to the relative motion between SAR platform and fixed targets on ground. In its simplest modelization this motion is assumed to be rectilinear aligned in the azimuth direction at constant velocity and height, leading to azimuth focusing parameters suitable for conventional SAR processing. However, the same parameters are no more valid when a moving target has to be imaged, since the relative motion is different in this case, [43]. Therefore, to retrieve correct focusing parameters, a new derivation of the relative motion between SAR platform and moving target has to be derived, taking into account also the target movement.

Referring to the along-track/slant-range plane (x,y), this relative motion can be simply espressed as:

$$\begin{cases} x(t_a) = x_0 + \left(V_a + V_t^{at}\right) \cdot t_a + a_x \dfrac{t_a^2}{2} \\ y(t_a) = R_0 + \left(V_t^{ct}\right) \cdot t_a + a_y \dfrac{t_a^2}{2} \end{cases} \qquad \textbf{Eq. IV-1}$$

where x_0 represent the azimuthal position of the target at mid-acquisition (we will neglect this term in the following without loss of generality), V_a is the SAR platform velocity, V_t^{at} is the target velocity component in along-track direction, a_x is the target acceleration in along-track direction, R_0 is the target slant range distance at closest approach, V_t^{ct} is the target radial component (namely in the cross-track direction), a_y is the target radial acceleration, and t_a is the slow-time.

Starting from Eq. IV-1, the behaviour of the slant-range distances between target and SAR platform (namely $R(t_a)$) can be simply derived, leading to:

$$R(t_a) = \sqrt{\left[R_0 + V_t^{ct} \cdot t_a + \frac{a_y}{2} t_a{}^2\right]^2 + \left[(V_a + V_t^{at}) \cdot t_a + \frac{a_x}{2} t_a{}^2\right]^2} =$$

$$= \sqrt{R_0^2 + 2R_0 \left[V_t^{ct} \cdot t_a + \frac{a_y}{2} t_a{}^2\right] + \left[V_t^{ct} \cdot t_a + \frac{a_R}{2} t_a{}^2\right]^2 + \left[(V_a + V_t^{at}) \cdot t_a + \frac{a_x}{2} t_a{}^2\right]^2} = \qquad \textbf{Eq. IV-2}$$

$$= R_0 \sqrt{1 + \frac{2}{R_0}\left[V_t^{ct} \cdot t_a + \frac{a_y}{2} t_a{}^2\right] + \frac{1}{R_0^2}\left[V_t^{ct} \cdot t_a + \frac{a_y}{2} t_a{}^2\right]^2 + \frac{1}{R_0^2}\left[(V_a + V_t^{at}) \cdot t_a + \frac{a_x}{2} t_a{}^2\right]^2}$$

By expanding the previous Eq. IV-2 according to a Taylor's series expansion an neglecting all the polynomial terms in t_a^3 or higher, the following approximated expression is obtained:

$$R(t) \cong R_0 \left\{1 + \left[\frac{1}{R_0}\left[V_t^{ct} \cdot t_a + \frac{a_y}{2} t_a{}^2\right] + \frac{1}{2R_0^2}\left[(V_a + V_t^{at}) \cdot t_a\right]^2\right]\right\} \qquad \textbf{Eq. IV-3}$$

As it is apparent, the target motion results in some additional terms:

- a linear term in t_a, which is present for non-null radial target velocity components;
- two quadratic terms in t_a^2, one related to radial target acceleration and the other related to along-track target velocity.

The linear term results simply in a Doppler centroid that shift the focused image of a moving target, not affecting the quality of the focusing[11]. On the other hand, a variation in the quadratic term, results in a variation of the azimuth chirp slope, thus leading to smearing effects in the corresponding azimuth focused pulse response, if conventional azimuth processing is performed. In other words, the azimuth processing designed to be a matched filter suitable for the stationary scene, it is no more "matched" when a moving target is considered. The resulting effects are those related to a mis-match filtering: a degradation of the achievable azimuth resolution as well as a degradation of the Signal to Clutter plus

[11] It has to be noticed that also the radial target velocity can deteriorate the azimuth imaging capabilities. In fact, if during the synthetic aperture the target moves across several range resolution cells, the range-walk effect arises. Range walks effects will be only partially considered in the following analysis, being the main scope of this work to take into account SAR defocusing due to along-track target velocity component. Hence, in the following, "target motion" will refer to "along-track target motion".

Noise Ratio (SCNR) otainable after focusing. These two defects limit the capability to image and to detect a target within a SAR image and, therefore, have to be corrected.

A viable solution to overcome these mis-match focusing defects, is to complicate the SAR focusing algorithm in order to take into consideration the possible motion of the target. The idea is to design a bank of different focusing filters, each one adapted to a different possible target motion. If no a priori information on the target motion is available, a reasonable interval of possible target velocities has to be defined and the different focusing filters will be associated to different along-track relative velocities between target and sensor evenly spaced within this interval. Oviously, some defocusing effects will remain present due not perfect matching between true relative target velocity and relative velocity used in the bank. We will call these defocusing effects as "quantization errors". The approach of focusing moving targets by means of a bank of different focusing filters has already been investigated in past literature, [44]. In particular, in [44] the number of filters L needed to maintain peak losses in the azimuth pulse response within 3 dB[12] is derived analytically.

In the following, the bank of focusing algorihms will be assumed based on the Chirp Scaling Algorithm (CSA, [45]). Among different focusing algorithms it has been selected the CSA since it is quite efficient from a computational point of view (namely no interpolations are required like in the case of Range-Doppler or Range Migration Algorithm) and because its first operation is an azimuth FFT. This will be an appealing characteristic to integrate this algorithm together with a post-Doppler STAP approach, as it will be deeply analyzed in the following sections.

Each branch of the bank is matched to a different possible target velocity component in the along-track (a.t.) direction. This means that in each CSA within the bank, the a.t. sensor velocity V_a has to be

[12] The azimuth signal relative to a moving target will result in a residual chirp due not perfect focusing (i.e. quantization errors). The number of filters is set so that the bandwidth of the residual chirp will remain within a Doppler resolution cell.

replaced with the relative a.t. velocity between sensor and target ($V^{(i)}$). Consequently, all the processing steps which depends on V_a have to be parallelized and customized, leading to the processing scheme sketched in **Figure IV-1** (Φ_1, Φ_2, and Φ_3 are the phase multiplication terms of CSA).

The number of parallel branches L has been determined analytically by following the approach in [44]. Each mover will be differently focused in the L images at the output of the L branches, showing a maximum peak level in the image obtained by using the a.t. velocity value that better approximates the relative a.t. velocity between target and sensor. A proper threshold (as for example obtained via a 2D Cell Average, CA, CFAR) can then be applied to each output image to detect the movers. The proposed technique takes into account only an a.t. target velocity component, while no processing is considered to compensate range walk effects due to cross-track (c.t.) target motion. Therefore, we expect that the bank of CSA will yield to performance comparable w.r.t. a matched filtering of the movers, except for a degradation factor due to range walk. To verify this, two different modifications are applied to the bank of CSA. In the first case, a range walk correction step is performed before the bank, while in the second case the range resolution is degraded so that movers are no more affected by range walk effects.

IV.2.1 CSA Based Bank Performance Analysis

To evaluate the effectiveness of the proposed technique, a SAR dataset of an observed scene with several moving targets is required. To this end, an emulated SAR dataset has been derived starting from a SAREX-92 image of the Tapajos rain forest focused in the slant range-azimuth plane with a resolution of 6 meters, see **Figure IV-2**. To use such an input image for our purposes, we have first applied an inverse focus processing to obtain the raw single-channel SAR data of stationary background. To do this, a flat Earth geometry has been supposed with the SAR working in non-squinted stripmap mode. Such a raw dataset of the stationary background has been added to raw returns from synthetic targets moving along roads A and B, see **Figure IV-2**.

Movers inserted in the image are represented by colored dots in their true position, an arrow indicating the corresponding motion. Circles of the same color indicate their smeared and displaced echo in the focused image. Targets velocities and relative components in the radial and a.t. directions are reported in Tab. IV-1. The considered scenario leads to a dwell time of about 1 second for the targets. The maximum target velocity of 22 m/s has been selected considering the particular environment, resulting in $L=11$ branches in the bank of CSA, [44].

Improved moving target detection performance

The first advantage related to the bank of CSA is the moving target detection improvement. To show this, a Monte Carlo simulation with 300 trials has been conducted for increasing SCR and different speckle realizations. Moving targets are detected via a 2D CA-CFAR (P_{fa} set to 10^{-4}) applied to each output image from each branch of the bank. Detection performance is expressed in terms of P_D versus SCR, as reported in **Figure IV-3** and in **Figure IV-4**. In particular, performance obtained by applying the traditional CSA (azimuth focusing matched to the stationary background) is compared with the bank of CSA (only the branch that gives the higher output power is considered), and with the matched CSA (CSA based focusing matched to the a.t. velocity of the target).

As expected, targets characterized by a higher a.t. velocity component are those that experience a higher detection improvement by implementing the bank of CSA w.r.t. the traditional CSA processing. Moreover, it is worth to notice that the detection performance of the bank of CSA is comparable w.r.t. the matched CSA, thus ensuring that a sufficient number of focusing filters has been considered. Referring to **Figure IV-4** (i.e. to road B), slight discrepancies in the achieved results are experienced due to range walk effects.

Improved moving target imaging performance

The mis-match reduction in moving targets focusing causes also an improvement in the achievable azimuth resolution. To show this, two different analysis have been conducted. In the former, the focusing of the movers has been analysed, neglecting the clutter contribution. Obtained results are reported only for target 1A, see **Figure IV-5**. The azimuth main cut of the target response obtained after the traditional CSA focus is compared with the corresponding responses obtained after the bank of CSA and after the matched CSA. Moreover, the pulse response obtained after a Matched Filtering (MF), including a range walk correction step, is reported for a theoretical comparison.

By implementing the bank of CSA the azimuth response main lobe becomes clearly visible, differently from the case of the traditional CSA. Moreover, the matched CSA case does not yield to substantial differences w.r.t the bank of CSA. By comparing the bank of CSA and the MF responses, it is possible to appreciate both a reduction in the response peak, and a degradation in the azimuth resolution. This latter effect is due to the reduced time the target remains in the same resolution cell.

In a second analysis, the azimuth resolution of all the movers has been measured adding the clutter contribution, for a SCR that guarantees a $P_D=0.9$. Obtained results are reported in **Tab. IV-2**. As apparent, the azimuth resolution improvement moving from the traditional CSA to the bank of CSA is higher for targets with higher a.t. velocities. As expected the bank and the matched CSA provide almost the same performance. Even in this case, the bank of CSA suffers a performance degradation w.r.t. the MF for those targets characterized by a high radial velocity component.

Bank of CSA with range walk correction

In order to overcome performance degradation due to range walk effects, analogous Monte Carlo simulations have been conducted after a Range Walk Correction (RWC) step adapted separately to each

target. The following **Tab. IV-3** reports a performance detection comparison for the cases of traditional CSA, bank of CSA without RWC (bank CSA NO RWC), bank of CSA with RWC (bank CSA RWC), and Matched Filter (MF).

The latter case has been considered for comparison. **Tab. IV-3** reports the minimum targets SCR required to achieve a detection probability $P_D=0.9$ ($P_{fa}=10^{-4}$). As is apparent, the RWC step allows to recover the target detection capabilities especially for targets highly affected by range walk effects (i.e. targets 1B, 2B, and 3B).

Bank of CSA with degraded range resolution

An alternative scheme to overcome the problems related to range walk, is to reduce the range resolution. This leads to an appealing scheme from a computational point of view, with all the drawbacks related to the reduced resolution. In particular, in the following analysis the range resolution is reduced by a factor 3, thus ensuring no range migration for any of the targets. The resolution degradation is obtained by filtering the received bandwidth of both the background image and synthesized targets. We expect that such a filtering causes a reduction in the SCR for targets that do not experience significant range walk, since part of the bandwidth is discarded. This will directly affect the detection capabilities.

Expected results are confirmed by **Figure IV-6**, which reports the detection performance of the low resolution bank of CSA compared with the full resolution case, for the targets moving along road A (i.e. with low range walk effects). Slightly different results are obtained for target moving along road B, i.e. with stronger range walk effects, see **Figure IV-7**. In fact, in this case the achievable performance of the low resolution scheme show a similar behavior w.r.t. the full resolution case. This means that the

SCR degradation due to the bandwidth filtering is approximately by compensated by the elimination of the migration of the movers from one range resolution cell to another.

Comments

The proposed technique is constituted by a bank of focusing filters (based on the CSA) each one matched to a different possible a.t. target velocity component. The bank of focusing filters has a positive effect both on target detection and imaging performance. The effectiveness of the proposed technique has been tested on an emulated dataset. Obtained results confirm the expected performance improvement both in terms of detection and imaging capabilities. Discrepancies w.r.t. theoretical performance are mainly due to cross-track target velocity component. To show this, two different analysis have been conducted. In the former, the same bank of CSA has been applied after a RWC step, separately applied to each mover. In the latter analysis, the range resolution has been reduced so that none of the target is affected by range walk effects. Both the analysis show that a proper range walk removal determines an increase of the bank of CSA performance up to a level comparable with a matched filtering.

IV.3 *Integration of the bank of CSA with a post-Doppler STAP approach*

As already mentioned in Section IV.1 , the bank of focusing filters presented above is able to provide high-resolution imaging of the moving targets present in the observed scene. However the SCNR recovery which it is provided by the bank of CSA it is not sufficient to ensure a reliable moving target detection capability especially if sub-clutter moving target detection capabilities are required. Hence, a M-SAR system it has to be considered and the bank of CSA has to be combined with a clutter cancellation step, such as a STAP technique. To this end, among various different STAP approaches, we have considered the post-Doppler STA approach introduced by Ender in [49]. This STAP approach is not only particularly suitable for the M-SAR case, but it is also suitable for an efficient integration with the bank of CSA previously presented.

Post-Doppler implementations of STAP are an appealing solution in the MSAR case, [49]. In fact, the special case of a SAR acquisition is characterized by very long Coherent Pulse Intervals (CPIs). Therefore, by modeling the echoes received from the stationary clutter as a stationary process, a theoretical clutter Doppler frequency components decoupling is obtained ([53]) if the time base tends to infinity and for Nyquist sampling. In practical cases, the synthetic aperture will not be infinite, leading to a non perfect de-correlation of different clutter Doppler frequency components. Hence, few adjacent Doppler frequency components are needed for proper clutter cancellation.

Concerning the implementation of such a clutter cancellation scheme, two aspects have to be considered. First of all, the nice property of frequency components decoupling can be obtained only sampling the clutter signal in the azimuth domain at the Nyquist rate (i.e. PRF equal to the clutter Doppler bandwidth). Moreover the interference covariance matrices should be estimated on received

data samples containing only clutter and thermal noise contributions (secondary data). In the following, such samples will be considered available to the system. It is worth to notice that this assumption is reasonable for the scenarios we are interested in. In fact, if the target received power is high with respect to the clutter plus noise contribution, a STAP approach might not be needed for adequate moving target detection, being sufficient only the SCNR recovery due to the bank of CSA. In constrast, a STAP approach is needed when the target received power is much lower than the clutter plus noise contribution. In this case, the interference covariance matrix can be directly estimated from secondary data samples containing target plus clutter plus noise contributions, being the target contribution negligible.

This makes possible a clutter cancellation in each Doppler component using the spatial DOFs and very few adjacent Doppler bins, thus resulting in a small clutter plus noise covariance matrix to be estimated and inverted. Being the correlation between adjacent Doppler bins very limited, it will be neglected in the following analysis, thus leading to a clutter cancellation performed Doppler bin per Doppler bin using only spatial DOFs. A sketch of the resulting post-Doppler STAP technique is reported in **Figure IV-8** for the sample case of a three parallel receiving channels.

The samples corresponding to the *k-th* row and to the *n-th* column of the matrices in the range-Doppler domain are collected in the $M \times 1$ vector $\mathbf{x}_{k,n}$. The weight vector $\mathbf{w}_{k,n}$ is determined as:

$$\mathbf{w}_{k,n} = \hat{\mathbf{R}}_{k,n}^{-1} * \mathbf{s}_n , \qquad \textbf{Eq. IV-4}$$

where $\hat{\mathbf{R}}_{k,n}^{-1}$ is the inverse interference covariance matrix in the Doppler domain, estimated from P secondary samples adjacent in the fast-time direction to the *k-th* sample, and $\mathbf{s}_n$ is a $M \times 1$ vector accounting for temporal delay sampling on the different channels. The corresponding clutter-free sample $r_{k,n}$ is then obtained as:

$$\mathbf{r}_{k,n} = \mathbf{w}_{k,n}^{H} * \mathbf{x}_{k,n} \,. \qquad \text{Eq. IV-5}$$

As is apparent, a 3-DOFs nulling has to be performed separately for each Doppler frequency component and for each row of the uncompressed data, since the clutter may not be assumed stationary along the range dimension.

A block diagram of the integrated clutter cancellation and bank of focusing filters using the CSA is depicted in **Figure IV-9** for the sample case of a three channels SAR system. As is apparent, the FFT in the azimuth domain required by the STAP technique is applied separated to the raw data acquired by each receiving channel. The azimuth FFT is also the first operation foreseen by the CSA, making feasible an efficient integration between the cancellation and the focusing steps. Once the clutter cancellation is performed, the bank of focusing filters is applied to the resulting clutter free data.

IV.3.1 Case Study

To evaluate the effectiveness of the proposed technique, a M-SAR datacube of an observed scene with several moving targets is required. Unfortunately, the authors do not have access to a dataset with those charecteristics. Therefore, an emulated M-SAR datacube has been derived starting from a SAREX-92 image of the Tapajos rain forest focused in the slant range-azimuth plane with a resolution of 6 meters, see **Figure IV-2**. To use such an input image for our purposes, we first applied an inverse focus processing to obtain the raw single-channel SAR data of stationary background. To do this, a flat Earth geometry has been supposed with the SAR working in non-squinted stripmap mode. Assuming the stationary background (i.e. clutter) to be perfectly correlated, a multi-channel SAR dataset can be derived from the single-channel SAR dataset by resampling the signal in the slow-time domain. In particular, the single-channel raw image has been first interpolated (i.e. over-sampled) and then

properly decimated in the slow-time domain to obtain equivalent M-SAR raw data acquired from three receiving channels displaced in the along-track direction of a quantity *dx* and *2·dx*, respectively (*dx=V_a/(3·PRF)*). Neither an additional temporal decorrelation nor an additional spatial decorrelation has been added to the multi-channel clutter dataset. These three raw images have been added to thermal noise and to synthetic raw returns from several targets moving along roads A and B (see **Figure IV-2**). In particular, a Clutter to Noise Ratio (CNR_{RAW}) of 13 dB and a Signal to Clutter Ratio (SCR_{RAW}) of -28 dB (both measured on the single-channel raw data) have been considered. **Figure IV-2** reports the focused image obtained combining coherently the three images and applying a CSA matched to the stationary background without any preliminary STAP processing step. After focusing, an averaged CNR_{FOC} of about 16 dB is experienced over the image. Moving targets inserted in the image are represented by colored dots in their true position, an arrow indicating the corresponding motion. Circles of the same color indicate their smeared and displaced echo in the focused image.

Targets velocities and relative components in the cross/along-track directions, are reported in Tab. IV-1.

The maximum target velocity of 22 m/s has been selected considering the particular environment. For our study case we get a resulting number of filters *L=11*. Both defocusing and low SCR_{RAW} value make difficult the detection of the movers.

To show the effectiveness of the bank of CSA in correctly focusing moving targets, in **Figure IV-10** we consider, as an example, the azimuth pulse response of target 2A when using the traditional CSA (i.e. with along-track velocity given by the sensor velocity V_a) and the bank of CSA (only the branch giving the maximum output power for the considered target).

For simplicity, in this analysis neither clutter nor noise contributions have been added. As is apparent, a recovery in the peak target response as well as an improvement in the azimuth resolution is experienced.

It is worth to notice that, in general, the target azimuth pulse response given by the bank of CSA might slightly differ from the theoretical one which can be obtained by using the exact value of the relative along-track velocity between the sensor and the mover. A better approximation of the theoretical target pulse response could be possible increasing the number of branches, i.e. at the expense of a higher computational cost.

The same M-SAR raw datacube has been focused by means of traditional CSA with a preliminary STAP processing step. The 3x3 interference covariance matrices have been estimated on the basis of $P=6$ secondary data samples. The effectiveness of the clutter cancellation has been verified by measuring the reduction of the clutter plus noise power in the focused image with respect to the "no STAP case", see **Figure IV-2**. In particular, a reduction of the clutter plus noise power close to 13 dB has been observed. This value is approximately equal to the maximum theoretical reduction, achievable when the clutter level is lowered down to the noise level (clutter plus noise power reduction = CNR_{FOC} – 3 dB). In the first two columns of **Tab. IV-4**, the improvement in $SCNR_{FOC}$ moving from the "no STAP case" to the "STAP case" can be appreciated, for a Monte Carlo simulation with 100 trials. As is apparent, the $SCNR_{FOC}$ improvement is lower than the clutter plus noise power reduction. This is mainly due to a reduction of the power signal level due to low target velocities. The resulting values of $SCNR_{FOC}$ guarantee a proper target detection capability. Nevertheless, these returns appear still defocused, making the bank of CSA needed for high-resolution imaging. To show the effectiveness of the integrated processing, we still refer to target 2A. In particular, in **Figure IV-11** a comparison among azimuth pulse responses is conducted for the following three cases: no STAP + traditional CSA, STAP + traditional CSA, and STAP + bank of CSA processing.

As is apparent, in the STAP + bank of CSA case, the target pulse response main-lobe becomes clearly visible against the interference background. An analysis of the $SCNR_{FOC}$ achievable applying the integrated technique are reported in the third column of **Tab. IV-4** for the considered targets, refering to

the Monte Carlo simulation mentioned above. As expected, a further $SCNR_{FOC}$ improvement is experienced when applying the bank of CSA filters.

In **Tab. IV-5** is reported a comparison of azimuth resolutions (r_{AZ}) for the two cases of STAP + traditional CSA and STAP + bank of CSA. As is apparent, an improvement in the achievable azimuth resolution is experienced for all the considered targets, making evident the need of the bank of CSA for high-resolution imaging of the movers. Refering to the r_{AZ} values obtained applying the bank of CSA, two different aspects have to be considered. First of all, the bank of filters create a discretization of the possible moving targets azimuth chirp slopes. Secondly, the target radial velocity component might cause range walk, thus decreasing the dwell time and, consequently, the achievable resolution.

IV.3.2 Comments

An integrated technique for M-SAR clutter cancellation and high-resolution imaging of moving target has been presented. The clutter cancellation step is conducted in the Doppler frequency domain (i.e. after applying a separate azimuth FFT to raw data from each channel) and the high-resolution focusing of movers is achieved by means of a bank of CSA filters. The proposed approach gives two main advantages. First of all, sampling at Nyquist rate in azimuth, clutter cancellation can be performed separately for each Doppler frequency using only spatial DOFs, resulting in small interference covariance matrices to be estimated and inverted. Moreover, the azimuth FFT required by this clutter cancellation technique is also the first operation required by the focus algorithm (i.e. the CSA). Hence this FFT is common to both the techniques, making feasible an efficient integration. The effectiveness of the proposed integrated technique has been tested on an available dataset with added synthetic moving targets.

IV.4 *Performance comparison with an ATI-based approach*

Even if the previous Sections demonstrated the effectiveness of the proposed integrated technique for moving target detection and imaging, it is important to evaluate the cost that has to be paid for it.

Spacifically, the following analysis has been focused on the evaluation of the computational burden of the clutter cancellation step, being, usually, the STAP not a low-cost cutter cancellation technique. In fact, to make the clutter cancellation adaptive, an estimation (and corresponding invertion) of the interference covariance matrix has to be conducted on a Doppler bin by Doppler bin basis. To this end, a comparison has been conducted between the post-Doppler STAP approach and a well-known low-cost clutter removal approach, like the ATI. Generally speaking, we expect the ATI approach to be more efficient, since no interference covariance matrix has to estimated and inverted.

To allow a fair comparison between ATI and STAP in conjuction with the CSA, we have first neglected the bank of CSA, thus considering a so-called "*single CSA case*". The resulting integrated schemes are reported in **Figure IV-12** and in **Figure IV-13** for the *ATI + single CSA* and *STAP + single CSA* cases, respectively. Secondly, the analysis has been extended to the *ATI + bank of CSA* and *STAP + bank of CSA* cases have been addressed.

IV.4.1 ATI + single CSA

The ATI approach is considered as a "low-cost" GMTI technique for M-SAR systems, since it exploits only the interferometric phase (i.e. the phase difference between the channels) to perform clutter cancellation and target detection. After coregistering the channels and under ideal conditions, the two channel signals are identical for clutter returns. Thus they can be cancelled out by computing the

phase difference, leaving only the moving targets in the differential data. In practice, the cancellation capability is limited by the unavoidable phase noise.

A skecth of the ATI approach based on the CSA is reported in **Figure IV-12**. As it is apparent, the evaluation of the interferogram requires the application of the CSA on both channels separately. However, it results in a quite simple processing scheme which typically allows reliable detection performance against different clutter scenarios, [54]. Hence it can be considered as a valid benchmark to compare the detection performance and the computational burden of the post Doppler STAP approach considered in the following.

IV.4.2 Case study for performance comparison

To evaluate the moving target detection capabilities of the two integrated techniques, a M-SAR datacube of an observed scene with several moving targets is required. An emulated M-SAR datacube has been derived starting from the same SAREX-92 image of the Tapajos rain forest focused in the slant range-azimuth plane with a resolution of 6 meters, see **Figure IV-2**. Moving targets inserted in the image are represented by colored dots in their true position, an arrow indicating the corresponding motion. Targets velocities and relative SCR measured on the single-channel raw data are reported in **Tab. IV-6**. Please notice that lower moving targets velocities have been considered with respect to previous analysis since, in this context, we are not interested in the imaging of the targets and a *single CSA* approach is taken into account. Specifically, targets moving along road A show the same velocity and different SCR values, while targets along road B share the same SCR but different velocities. All the injected targets are well below the clutter level so that they cannot be directly detected on the focused image.

Figure IV-14 and **Figure IV-15** show the detection results of the ATI and STAP techniques respectively, against the considered case study scenario. To allow a fair comparison, the detection

thresholds have been set to obtain a quite comparable number of false alarms in both cases. In the ATI case, a multi-look approach has been used with 14 looks for the interferogram evaluation. Solid circles indicate correctly detected targets, while dashed circles represent missed detections. A sketch of the detection results is also reported in **Tab. IV-6**. As it is apparent, both techniques are able to detect targets with relatively high velocities and SCR values (i.e. targets 3A, 1B, and 2B), while both STAP and ATI fail in detecting target 2A, due to the extremely low SCR value. In contrast, STAP outperforms ATI in the detection of very slowly moving targets (e.g. target 3B) or for target echoes of limited power (e.g. target 1A). In fact, in these cases, the ATI approach is not able to separate the target motion induced phase difference with respect to the unavoidable phase noise. Obviously, better results could be obtained with ATI if an higher number of receiving channels is exploited, [55]. However this should be paid in terms of computational load and system complexity. Moreover a similar performance improvement should be expected for the STAP approach when increasing the number of spatial DOFs.

IV.4.3 Computational load comparison: single CSA

The proposed efficient integration of the post Doppler STAP and the CSA makes this approach comparable, from a computational point of view, with the ATI approach sketched in **Figure IV-12**. In fact, by comparing **Figure IV-12** and in **Figure IV-13**, it is apparent that the higher computational load of the clutter cancellation stage required by the STAP technique is compensated by the computational saving deriving from the application of the (single) CSA over the single-channel clutter-free data at the output of the STAP.

Tab. IV-7 reports a list of the main operations required by the two considered SAR-GMTI techniques, as a function of the number M of receiving channels. For each operation, also the unitary computational cost is reported, expressed in terms of complex multiplications. For simplicity, the dimension of the single-channel raw data (N) is assumed to be the same in range and azimuth. The

computational cost comparison of the two techniques is also reported in **Figure IV-16**, for *M=2* and *M=3* for increasing values of *N*. It is worth noticing that for small dimensions of the matrices $\mathbf{R}_{\mathbf{k,n}}$ (*M=2*) the computational burden of the STAP processing drastically reduces (i.e. low cost for estimation and inversion of $\mathbf{R}_{\mathbf{k,n}}$), so that the FFTs of the CSA play a key-role in the evaluation of overall cost. As a consequence, the STAP approach results even slightly more efficient w.r.t. the ATI technique for *M=2*, since the CSA has to be applied just once regardless of the number of receiving channels. Even for the case of *M=3*, the computational load of the two techniques is still comparable.

Finally it can be observed that both approaches are suitable to an integration with a bank of CSA based focusing filters, each one matched to a different along-track target velocity component, to produce a high-resolution image of the detected targets, [50]. Even in this case the presented STAP approach results more efficient w.r.t. ATI. In fact, if a bank of focusing filters is implemented together with the ATI approach, a pair of CSA has to be calculated for each branch of the bank (for *M=2*), resulting in an overall number of FFTs always greater than that required by the STAP approach.

IV.4.4 Computational load comparison: bank of CSA

The analysis conducted in Section IV.4.3 has shown a comparable overall computational burden of clutter cancellation plus focusing steps for the two approaches taken into consideration. In addition, it is worth to notice that the main contribution to the computational burden resides in the high cost of the FFTs (either in range or in azimuth direction). This point makes the ATI-based approach in a worse position with respect to the STAP-based approach, since a complete focusing has to be performed for each receiving channel separately to evaluate an interferogram. As a consequence, if not just a single CSA, but a bank of CSA is implemented jointly with the clutter removal stage, the increase of computational burden is higher for the ATI case w.r.t. the STAP based case. In fact, in the ATI case, a complete focusing has to be performed for each receiving channel and for each brach of the bank.

Figure IV-17 and **Figure IV-18** show the block diagrams of the corresponding integrated approaches. A summary of all the operation foreseen in the two cases together the corresponding computational cost (expressed in terms of complex multiplications) is reported in **Tab. IV-8**, where *L* indicates the number of branches in the bank. The overall computational cost is also reported in **Figure IV-19** for the ATI and the STAP cases against the data dimension for 2 and 3 parallel receiving channels. As it is apparent, when a bank of CSA is considered, the ATI approach becomes less efficient w.r.t. the STAP case. This is due to the higher number of FFTs required, which plays a key role in determining the computational cost.

IV.5 *Figures*

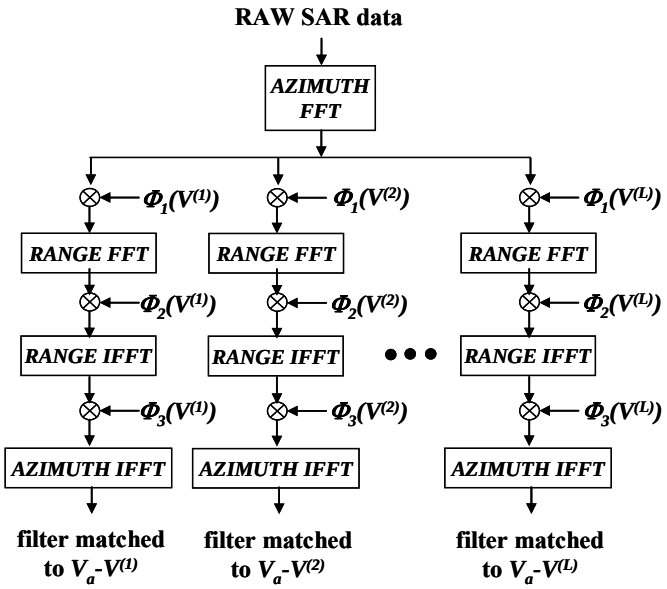

Figure IV-1 Bank of focusing filters based on CSA

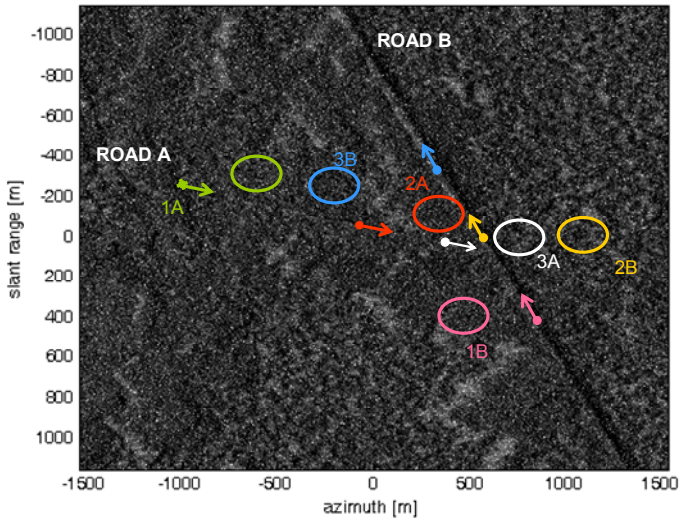

Figure IV-2 SAREX image with synthetic movers

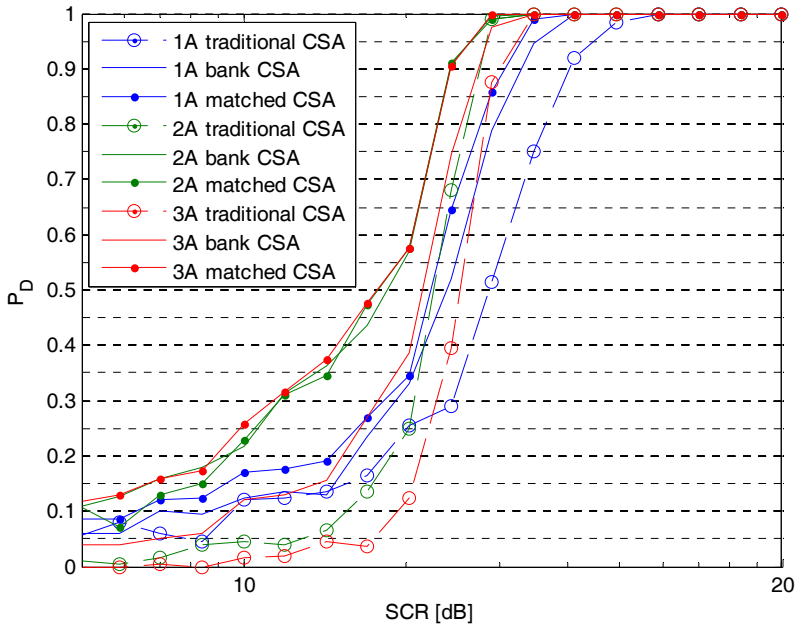

Figure IV-3 P_D vs. SCR: bank of CSA – road A

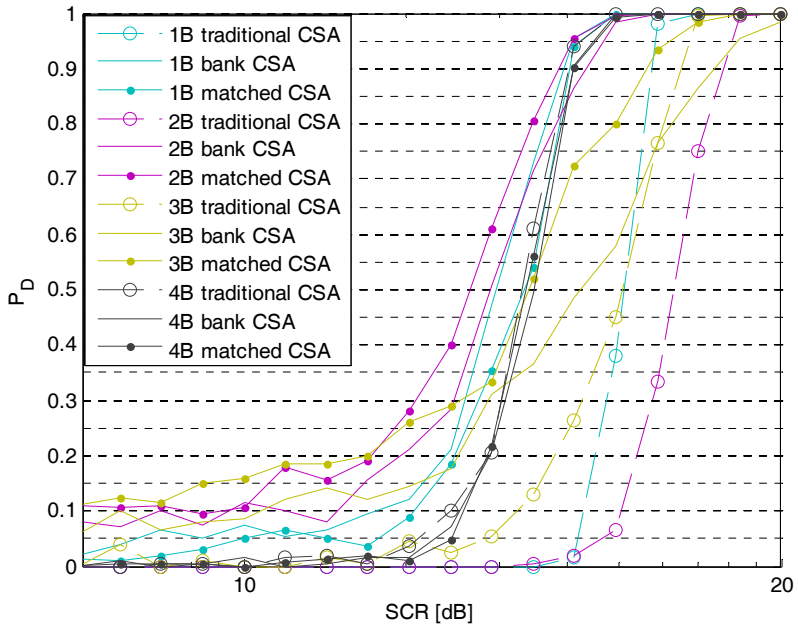

Figure IV-4 P_D vs. SCR: bank of CSA – road B

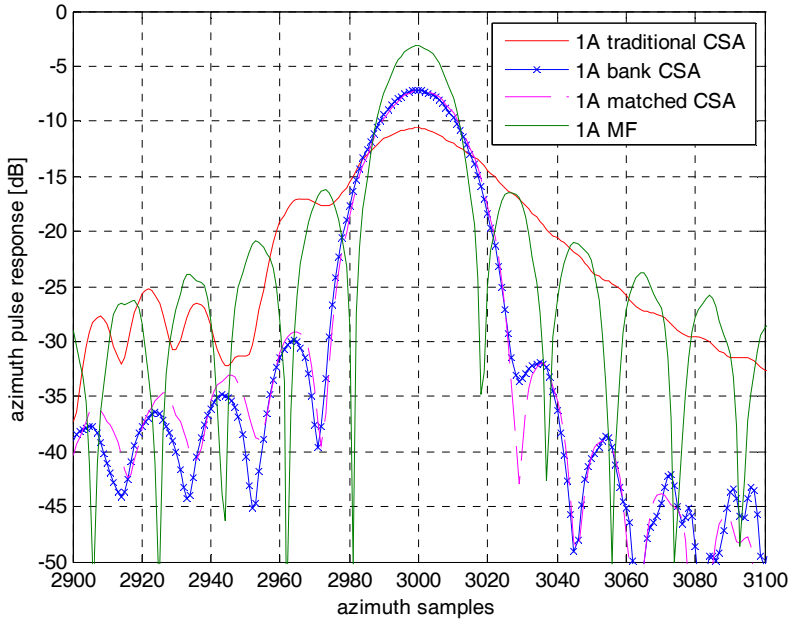

Figure IV-5 Comparison of azimuth pulse responses – target 1A

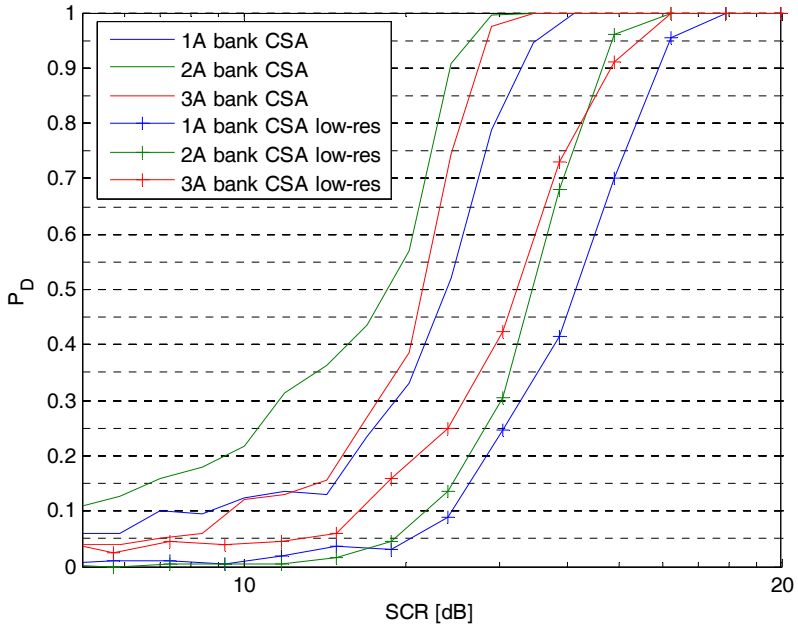

Figure IV-6 P_D vs. SCR: bank of CSA with low resolution – road A

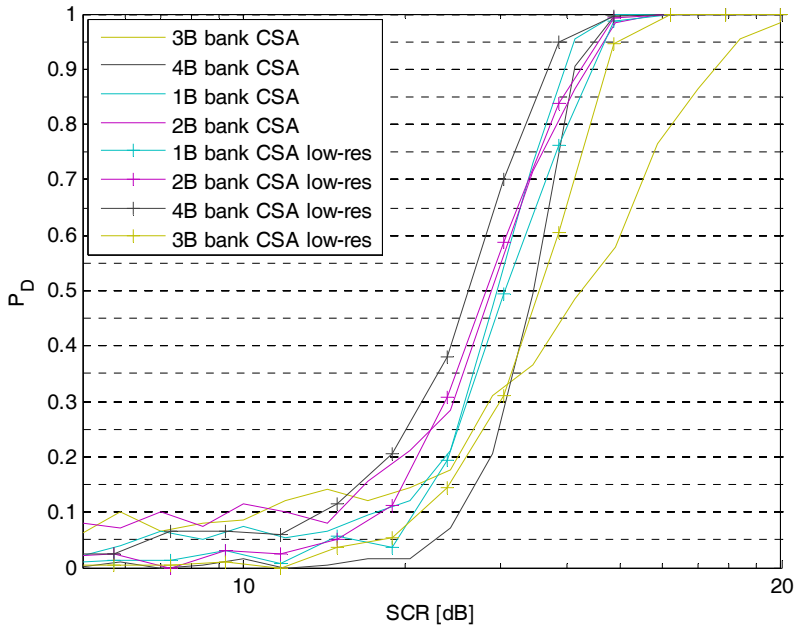

Figure IV-7 P_D vs. SCR: bank of CSA with low resolution – road B

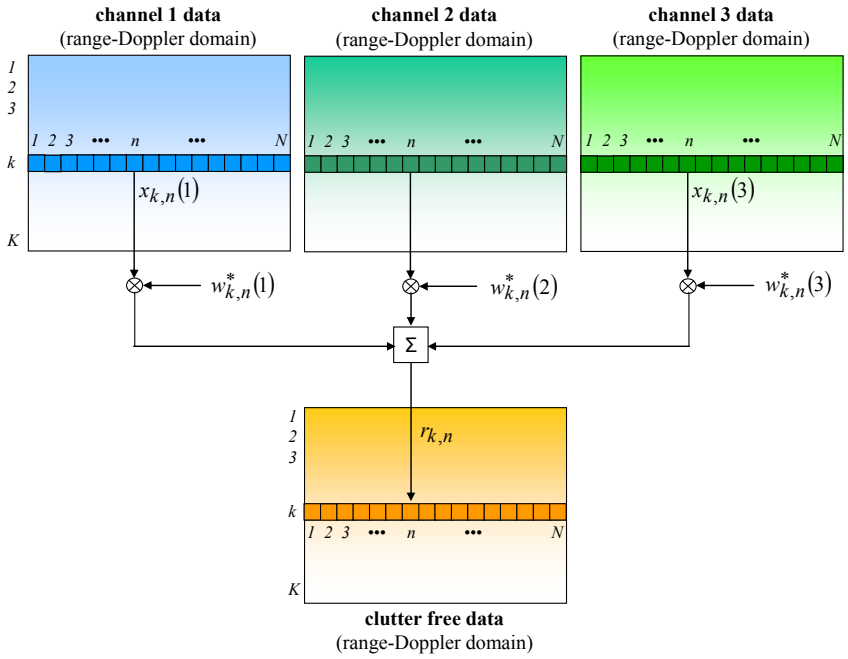

Figure IV-8 Clutter cancellation in the Doppler frequency domain

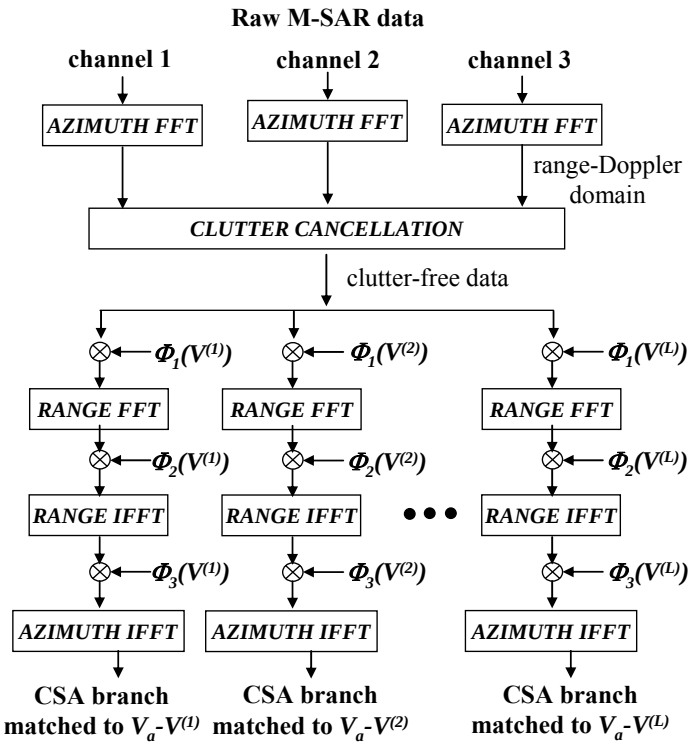

Figure IV-9 Integrated clutter cancellation and focusing scheme

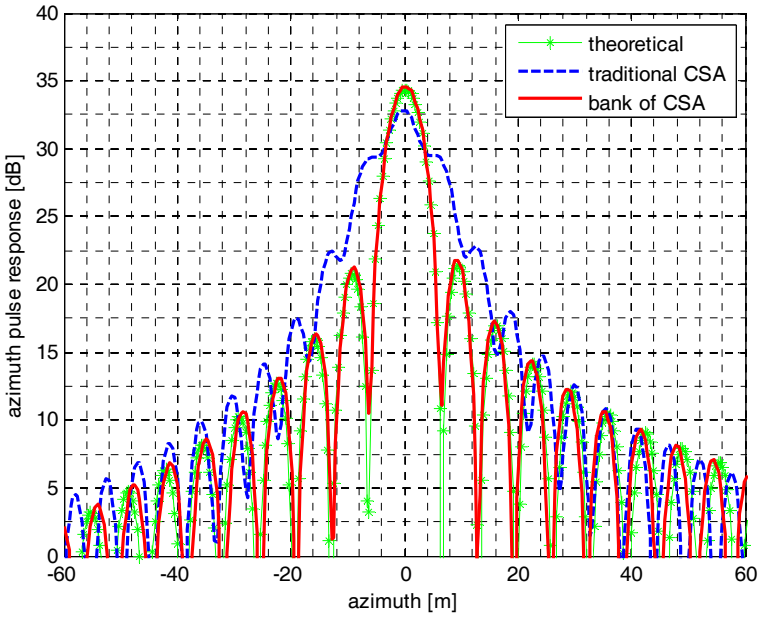

Figure IV-10 Comparison of azimuth pulse responses for target 2A

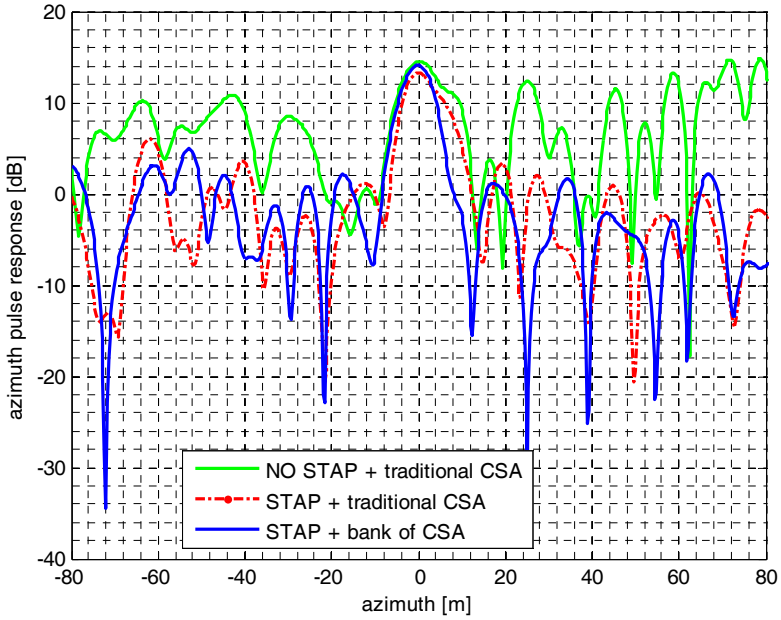

Figure IV-11 Comparison of azimuth pulse responses for target 2A

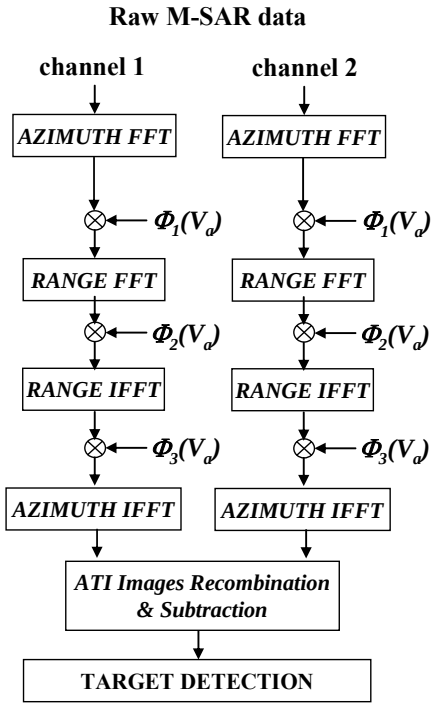

Figure IV-12 ATI and CSA

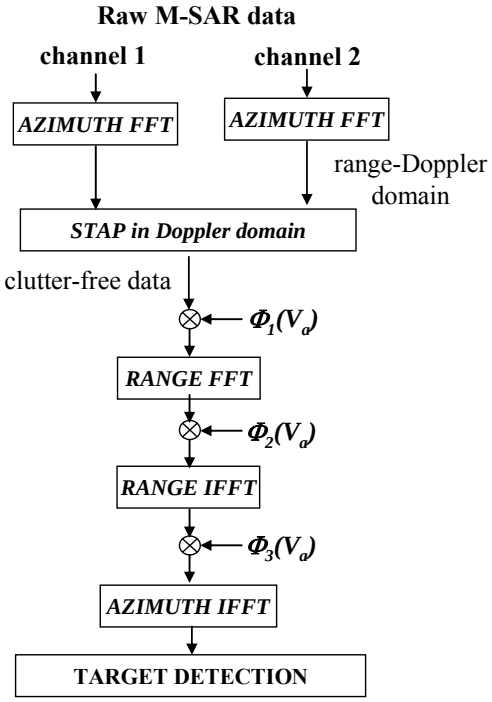

Figure IV-13 post-Doppler STAP and CSA

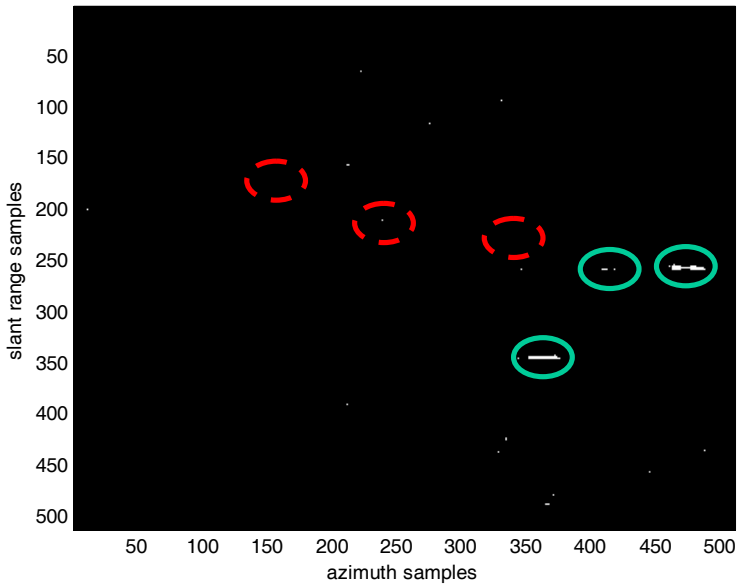

Figure IV-14 ATI approach: map of detections

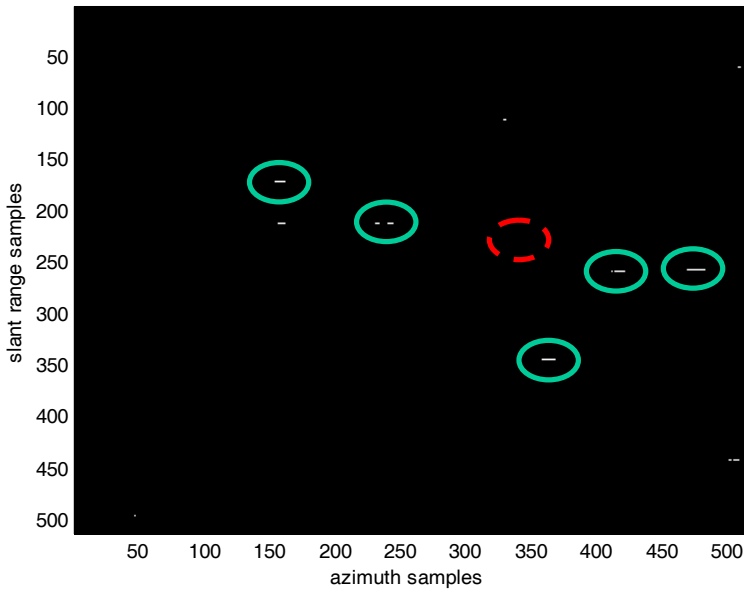

Figure IV-15 STAP approach: map of detections

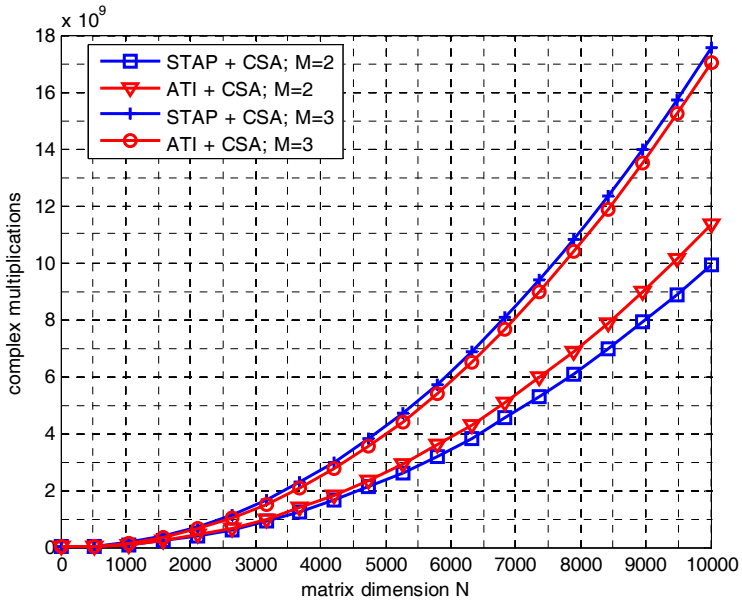

Figure IV-16 Computational cost comparison

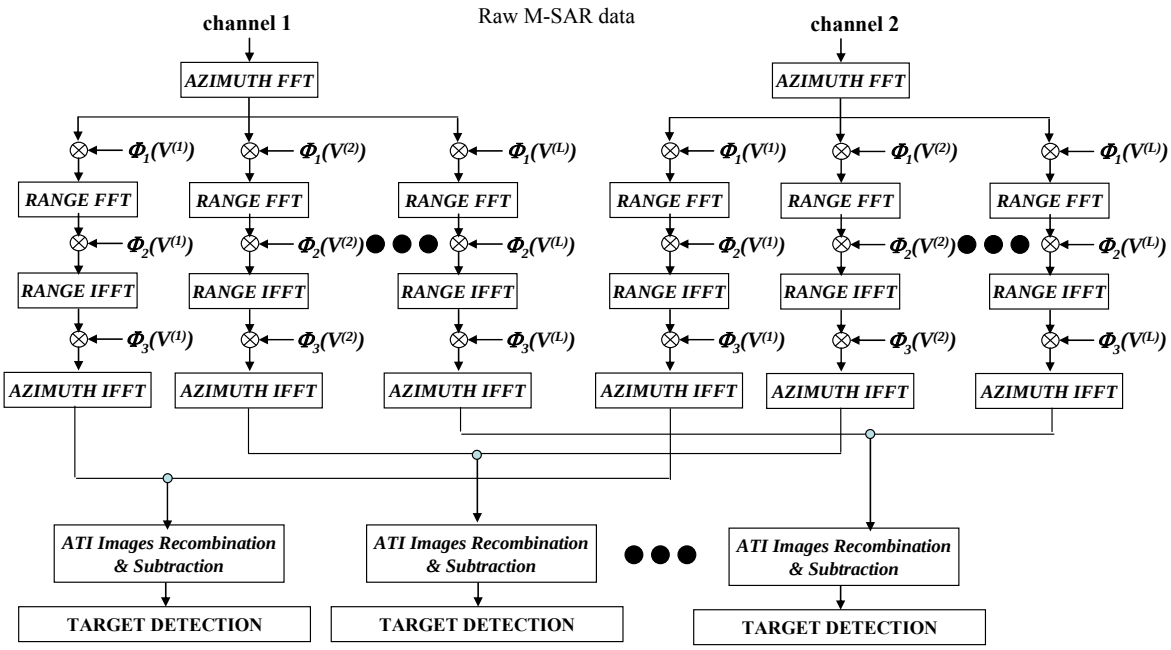

Figure IV-17 ATI + bank of CSA

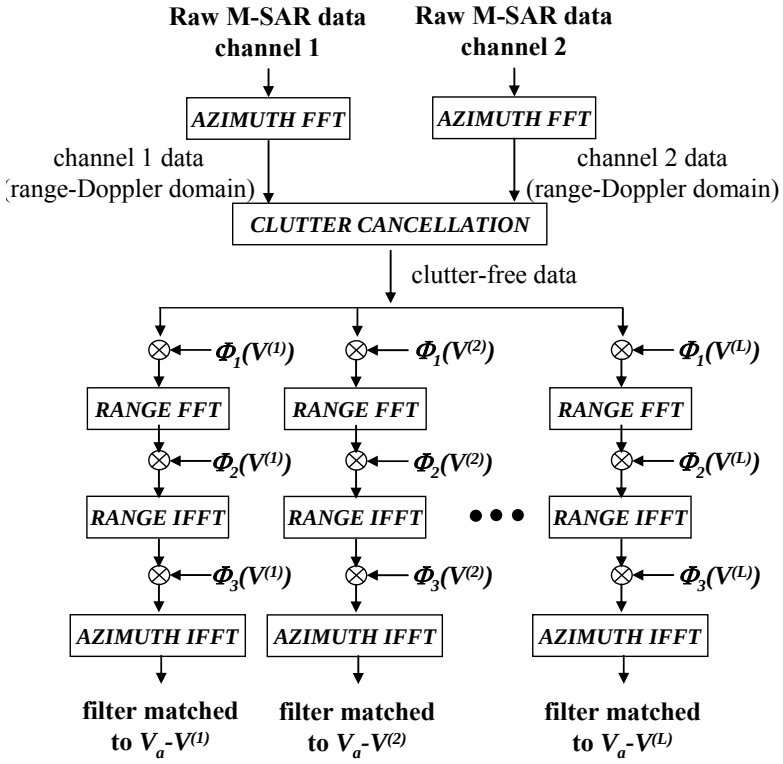

Figure IV-18 STAP + bank of CSA

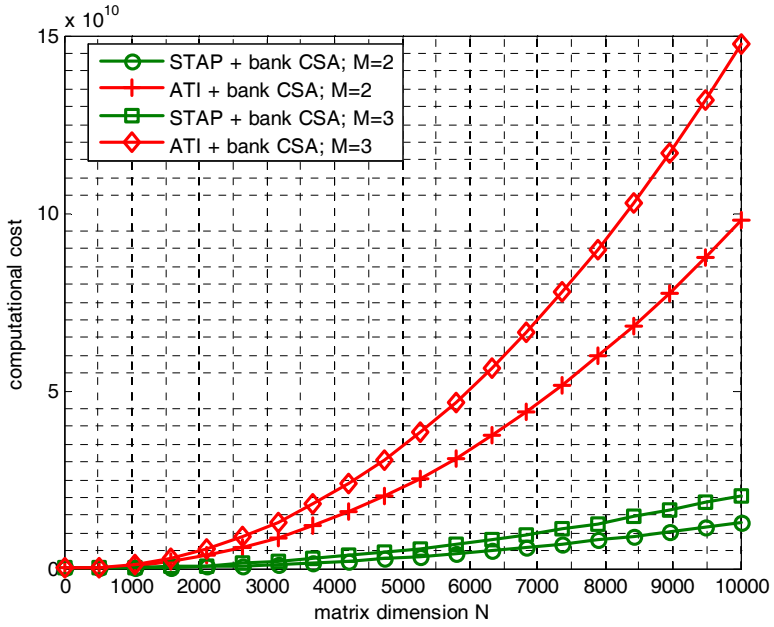

Figure IV-19 Computational load comparison (bank of CSA, L=11 filters)

IV.6 *Tables*

Target	Velocity [m/s]	Radial component [m/s]	A.t. component [m/s]
1A (dark blue)	22	5.37	21.28
2A (green)	10	2.44	9.67
3A (red)	5	1.22	4.83
1B (purple)	-10	-8.78	-4.13
2B (yellow)	-22	-19.33	-9.10
3B (brown)	18	15.83	7.44
4B (light blue)	7	6.16	2.89

Tab. IV-1 Moving targets velocities

	1A	2A	3A	1B	2B	3B	4B
traditional CSA [m]	12.8	12.6	6.1	8.1	11.3	12.6	7.7
bank CSA [m]	9.9	6.5	6.1	7.4	13.8	17.8	7.6
matched CSA [m]	10.0	6.6	6.3	7.4	13.8	17.8	7.6
MF [m]	7.3	6.6	6.3	5.9	5.6	6.4	6.3

Tab. IV-2 Azimuth resolutions comparison

	traditional CSA [dB]	bank CSA NO RWC [dB]	bank CSA RWC [dB]	MF [dB]
1A	$SCR_0 = 16.1$	$SCR_0 - 1.0$	$SCR_0 - 1.7$	$SCR_0 - 2.8$
2A	$SCR_0 = 14.4$	$SCR_0 - 0.6$	$SCR_0 - 0.6$	$SCR_0 - 0.4$
3A	$SCR_0 = 14.8$	$SCR_0 - 0.4$	$SCR_0 - 0.9$	$SCR_0 - 1.0$
1B	$SCR_0 = 17.6$	$SCR_0 - 1.6$	$SCR_0 - 2.7$	$SCR_0 - 3.2$
2B	$SCR_0 = 18.9$	$SCR_0 - 3.1$	$SCR_0 - 4.0$	$SCR_0 - 5.8$
3B	$SCR_0 = 18.1$	$SCR_0 + 0.6$	$SCR_0 - 2.5$	$SCR_0 - 3.6$
4B	$SCR_0 = 16.0$	$SCR_0 - 0.0$	$SCR_0 - 0.1$	$SCR_0 - 1.0$

Tab. IV-3 Performance detection: RWC case

Target	NO STAP + traditional CSA	STAP + traditional CSA	STAP + bank of CSA
1A	4.6	14.6	16.5
2A	6.5	14.2	16.4
3A	6.7	15.7	16.1
1B	4.0	13.5	15.4
2B	3.5	12.1	15.2
3B	3.5	14.0	16.2
4B	5.5	14.7	15.5

Tab. IV-4 $SCNR_{FOC}$ values on focused images

Target	STAP + traditional CSA	STAP + bank of CSA
	r_{AZ} [m]	r_{AZ} [m]
1A	13.9	9.2
2A	12.6	8.6
3A	10.4	9.4
1B	10.5	8.9
2B	11.9	8.5
3B	12.6	8.6
4B	9.9	9.2

Tab. IV-5 Azimuth resolutions

Target	Velocity [m/s]	SCR_{raw} [dB]	Detected?	
			ATI	STAP
1A	4.0	-25	no	yes
2A	4.0	-28	no	no
3A	4.0	-20	yes	yes
1B	6.0	-18	yes	yes
2B	4.0	-18	yes	yes
3B	2.0	-18	no	yes

Tab. IV-6 Target scenario

	STAP + CSA		ATI + CSA	
	overall number	unitary cost	overall number	unitary cost
FFTs	$(3+M)\times N$	$N\times\log_2 N$	$4\times M\times N$	$N\times\log_2 N$
CSA Phase multiplications	3	$N\times N$	$3\times M$	$N\times N$
Estimation of $\mathbf{R}_{k,n}$	$N\times N$	$2\times M^3$	-	-
Inversion of $\mathbf{R}_{k,n}$	$N\times N$	M^3	-	-
Evaluation of $\mathbf{w}_{k,n}$	$N\times N$	M^2	-	-
Evaluation of $\mathbf{r}_{k,n}$	$N\times N$	M	-	-
Interferogram evaluation	-	-	$M-1$	$N\times N$
Total	$(3+M)\times N^2\times\log_2 N + (3M^3+M^2+M+3)\times N^2$		$(4\times M)\times N^2\times\log_2 N + (4M-1)\times N^2$	

Tab. IV-7 Computational cost comparison single CSA

	STAP + bank CSA		ATI + bank CSA	
	overall number	unitary cost	overall number	unitary cost
FFTs	$(3+M)\times N$	$N\times\log_2 N$	$(M+3\times L\times M)\times N$	$N\times\log_2 N$
CSA Phase multiplications	$3\times L$	$N\times N$	$3\times L\times M$	$N\times N$
Estimation of $\mathbf{R}_{k,n}$	$N\times N$	$2\times M^3$	-	-
Inversion of $\mathbf{R}_{k,n}$	$N\times N$	M^3	-	-
Evaluation of $\mathbf{w}_{k,n}$	$N\times N$	M^2	-	-
Evaluation of $\mathbf{r}_{k,n}$	$N\times N$	M	-	-
Interferogram evaluation	-	-	$L\times(M-1)$	$N\times N$
Total	$(3+M)\times N^2\times\log_2 N + (3M^3+M^2+M+3L)\times N^2$		$(3L+1)\times M\times N^2\times\log_2 N + (4LM-L)\times N^2$	

Tab. IV-8 Computational cost comparison bank of CSA

V REFERENCES

[1] Currie A., Brown M.A., “Wide-swath SAR”, Radar and Signal Processing, *IEE Proc. F*, Vol: 139, N. 2, Apr. 1992, pp. 122–135.

[2] Lombardo P., Colone F., “Potenzialità delle antenne multicanale con elaborazione adattiva per radar da piattaforma spaziale del tipo di COSMO-SkyMed”, *Quaderni della Società Italiana di Elettromagnetismo*, Vol. 1, N. 3 Settembre 2005.

[3] Krieger G., Gebert N., Moreira A., “Unambiguous SAR signal reconstruction from nonuniform displaced phase center sampling”, *IEEE GRS Letters*, Vol. 1 , N. 4 , Oct. 2004, pp. 260-264.

[4] Gebert N., Krieger G., Moreira A., "SAR signal reconstruction from non-uniform displaced phase centre sampling in the presence of perturbations", *Proc. IGARSS 2005*, vol.2, pp. 1034- 1037, 25-29 July 2005.

[5] Prati C., Rocca R., “Improving Slant-Range Resolution With Multiple SAR Surveys”, *IEEE Trans. AES*, 1993, 29, (1), pp. 135-144.

[6] Fornaro G., Pascazio V., Schirinzi G., “Resolution Improvement Via Multipass SAR Imaging”, *IGARSS Proc.*, Sydney (Australia), July 2001.

[7] Guillaso S., Reigber A., Ferro-Famil L., Pottier E., “Range Resolution Improvement of Airborne SAR Images”, *IEEE GRS Letters*, 2006, 3, (1), pp. 135-139.

[8] Tebaldini S., “Single and Multipolarimetric SAR Tomography of Forested Areas: A Parametric Approach”, *IEEE Trans. GRS*, 2010, in print.

[9] Nannini M., Scheiber R., Moreira A., "Estimation of the Minimum Number of Tracks for SAR Tomography", *IEEE Trans. GRS*, 2009, 47, (2), pp. 531-543.

[10]Bradaric I., Capraro G.T., Weiner D. D., Wicks M. C., "A Framework for the Analysis of Multistatic Radar Systems with Multiple Transmitters," *Int. Conf. on Electromagnetics in Advanced Applications*, 2007. ICEAA 2007.

[11]Magde K.M., Wicks M.C., "Waveforms in virtual tomographic arrays," *Int. Waveform Diversity and Design Conference*, 2007.

[12]Eigel R.L., Collins P.J., Terzuoli A.J., Nesti G., Fortuny J., "Bistatic scattering characterization of complex objects", *IEEE Trans. GRS*, 2000, Vol. 38, Issue 5, Part 1, pp. 2078 – 2092.

[13]Skolnik M., "Radar Handbook", Third Edition, *McGraw Hill*, 2008, pp. 23.19-23.20.

[14]Krieger G., Cassola M. R., Younis M., Metzig R., "Impact of oscillator noise in bistatic and multistatic SAR", *IEEE GRS Letters*, 2006, 3, (3), pp. 424-428.

[15]Younis M., Metzig R., Krieger G., "Performance prediction of a phase synchronization link for bistatic SAR", *IEEE GRS Letters*, 2006, 3, (3), pp. 429-433.

[16]Wang W., "Approach of adaptive synchronization for bistatic SAR real time imaging", *IEEE Trans. GRS*, 2007, 45, (9), pp. 2695-2700.

[17]Correll, B., "Efficient spotlight SAR MIMO linear collection geometries," *Proc. European Radar Conference (EuRAD) 2008, Amsterdam (NL),* pp.21-24, 30-31 Oct. 2008.

[18]Pastina D., Bucciarelli M., Lombardo P., "Multi-platform distributed ISAR for surveillance and recognition", *Proc. IEEE RADAR 2009*, Bordeaux (France), Oct. 2009.

[19]Pastina D., Bucciarelli M., Lombardo P., "Multi-platform ISAR for flying formation", *Proc. IEEE RadarCon*, Pasadena (USA), May 2009.

[20]Krieger G., Gebert N., Moreira A., "Multidimensional Waveform Encoding: A New Digital Beamforming Technique for Synthetic Aperture Radar Remote Sensing," *IEEE Trans. GRS*, 2008, 46, (1), pp. 31-46.

[21]Dall J., Kusk A., "Azimuth Phase Coding for Range Ambiguity Suppression in SAR", *Proc. IGARSS 2004*, Vol. 3, pp. 1734-1737, Anchorage, Sept. 2004.

[22]Cristallini D., Sedehi M., Lombardo P., "SAR Imaging Solutions Based on Azimuth Phase Coding", *Proc. EUSAR 2008*, vol. 3, pp. 57-60, Friedrichshafen, Germany, June 2008.

[23]Pillai S.U., Himed B., Li K.Y., "Effect of Earth's rotation and range foldover on Space-based radar performance", *IEEE Trans. AES*, 2006, (42), (3), pp. 917-932.

[24]Cristallini D., Pastina D., Lombardo P., "Efficient Configurations of SAR Sensors for Improved Range Resolution", *Proc .IGARSS 2009*, Cape Town (South Africa), July 2009.

[25]Raney R. K., Runge H., Bamler R., Cumming I. G., Wong F. K., "Precision SAR processing using chirp scaling", *IEEE Trans. GRS*, 1994, 32, (4), pp. 786-799.

[26]Moreira A., Mittermayer J., Scheiber R., "Extended chirp scaling algorithm for air- and spaceborne SAR data processing in stripmap and scan SAR imaging modes," *IEEE Trans. GRS*, 1996, 34, pp. 1123–1136.

[27]Mittermayer J., Moreira A., Loffeld O., "Spotlight SAR Data Processing Using the Frequency Scaling Algorithm", *IEEE Trans. GRS*, 1999, 37, (5), pp. 2198-2214.

[28]Cafforio C., Prati C., Rocca F., "SAR Data Focusing Using Seismic Migration Techniques*", IEEE Trans. AES*, 1991, 27, (2), pp 194-206.

[29]Goj W.W., "Synthetic Aperture Radar and Electronic Warfare," *Artech House*, 1989.

[30]Dumper K., Cooper P.S., Wons A.F., Condley C.J., Tully P., "Spaceborne Synthetic Aperture Radar and Noise Jamming", *Systems Eng. & Assessment Ltd*, UK, 1997.

[31]Sedehi M., Cristallini D., Marini J., Lombardo P., "Impact of an Electromagnetic Interference on Imaging Capability of a Synthetic Aperture Radar", *Proc. IEEE Aerospace Conf. 2007*, March 2007, Big Sky, USA.

[32]Lombardo P., Sedehi M., Colone F., Bucciarelli M., Cristallini D., "Dual channel adaptive antenna nulling with auxiliary selection for spaceborne radar", *Proc. IEEE Aerospace Conf. 2008*, Big Sky, Montana, March 1 - 8, 2008.

[33]Sedehi M., Colone F., Cristallini D., Lombardo P., "A reduced order jammer cancellation scheme based on double adaptivity", *Proc. IEEE Radar Conf. 2008*, Rome, Italy, May 26-30, 2008.

[34]Sedehi M., Colone F., Cristallini D., Lombardo P., "A reduced order jammer cancellation scheme based on double adaptivity", to appear on *IEEE Trans. Aerospace and Electronic Systems*.

[35]Reed I.S., Mallett J.D., Brennan L.E., "Rapid convergence rate in adaptive arrays," *IEEE Trans AES*, Vol. 10, No. 6, November 1974, pp. 853-863.

[36]A. Farina, "Antenna-Based Signal Processing Techniques for Radar Systems," *Artech House*, 1992.

[37]Golub G. H., Van Loan C. F., "Matrix Computations", *Johns Hopkins University Press*, Baltimore, second edition, 1989.

[38]Sedehi M., Cristallini D., Bucciarelli M., Lombardo P., "Constrained adaptive beamforming for electromagnetic interference cancellation for a synthetic aperture radar", *IET Int. Radar Conf.*, October 2007, Edinburgh, UK.

[39]Sedehi M., Bucciarelli M., Cristallini D., Scolamiero S., Lombardo P., "Interference covariance matrix estimation for a Multi-Channel Synthetic Aperture Radar", *Proc. EUSAR 2008*, June 2008, Friedrichshafen, Germany.

[40]Van Trees H.L., "Optimum Array Processing," *John Wiley & Sons*, 2002.

[41]L. Rosenberg, D. A. Gray, "Anti-jamming Techniques for Multi-Channel SAR Imaging", *IET Proc. on RSN*, 153, (3), pp. 234-242.

[42]Bucciarelli M., Cristallini D., Pastina D., Sedehi M., Lombardo P., "Integrated wideband antenna nulling and focusing technique for multi-channel synthetic aperture radar", *Proc. Int. Radar Symposium (IRS) 2008*, Wroclaw, May 21-23, 2008.

[43]Raney R. K., "Synthetic aperture imaging radar and moving target", *IEEE Trans. AES*, 1971, 7, pp. 499-505.

[44]Barbarossa S., "Detection and imaging of moving objects with synthetic aperture radar, Part 1", IEE Proc.-F, 1992, 139, (1), pp. 79-88.

[45]Raney R. K., et alii, "Precision SAR processing using chirp scaling", *IEEE Trans. GRS*, 1994, 32, (4), pp. 786-799.

[46]Klemm R., "Principle of Space-Time Adaptive Processing", *IEE Publisher*, 2002.

[47]Pastina D., Battistello G., Aprile A., "Change detection based GMTI on single channel SAR images", *Proc. EUSAR 2008*, vol. 3, pp. 85-88, 2-5 June 2008, Friedrichshafen, Germany.

[48]Farina A., Lombardo P., "Space-time techniques for SAR", chapter in the book edited by Richard Klemm, "Applications of Space-Time Adaptive Processing", *IEE Publisher*, 2004.

[49]Ender J. H. G., "Space-time processing for multichannel synthetic aperture radar", *Electr. & Comm. Eng. Journal*, 1999, 11, (1), pp.29-38.

[50]Cristallini D., Colone F., Pastina D., Lombardo P., "Integrated Clutter Cancellation and High-Resolution Imaging of Moving Targets in Multi-channel SAR", *Proc. European Radar Conference (EuRAD) 2009*.

[51]Bürger W., “Space-Time Adaptive Processing: Algorithms”, *Advanced Radar Signal and Data Processing* (pp. 7-1 – 7-12). Educational Notes RTO-EN-SET-086, Paper 7. Neuilly-sur-Seine, France: RTO.

[52]Cristallini D., Lombardo P., Pastina D., Mennella A., “Chirp Scaling Based Detection of Moving Targets in SAR Images”, *Proc. IGARSS 2009*, Cape Town (South Africa), July 2009.

[53]Wei-Biao Wu, “Fourier Transforms of Stationary Processes”, *Proc. American Mathematical Society*, vol. 133, no. 1, pp. 285-293.

[54]Gierull C. H., “Statistical analysis of multi-look SAR interferograms for CFAR detection of ground moving targets”, *IEEE Trans. GRS*, 2004, 42, (4), pp. 691-701.

[55]Budillon A., Pascazio V., Schirinzi G., “Multichannel Along-Track Interferometric SAR Systems: Moving Targets Detection and Velocity Estimation”, *Int. Journal of Navigation and Observation*, vol. 2008, pp. 1-16.